Groningen Seismological Models for Activity Rate Forecasting

Nora DeDontney

Upstream Research Centre, ExxonMobil

Datum June 2017

Editors Jan van Elk & Dirk Doornhof

General Introduction

The seismological model incorporated in the Hazard and Risk Assessment makes use of fundamental physics-based models, with pore pressure depletion as the driver for the seismic activity (Ref. 1 to 3).

Alternative approaches to the forecasting of seismic activity have been explored. This report describes the development of a seismological model for the activity rate in the Groningen field, using the geomechanical model developed for the Groningen field (4 to 6). Both compaction and fault slip based seismological models are examined.

References

1. Bourne S.J., Oates S.J., 2017. Extreme threshold failures within a heterogeneous elastic thin-sheet account for the spatial-temporal development of induced seismicity within the Groningen gas field, Journal of Geophysical Research: Solid Earth 122(12), 10299-10320.
2. Bourne S.J., Oates S.J., van Elk J., 2018. The exponential rise of induced seismicity in the Groningen gas field and its implications for controlling seismic risk. Geophysical Journal International 213(3), 1693-1700.
3. Gaussian Process Optimisation of the Elastic Thin-Sheet Seismological Model for Depletion Induced Seismicity in the Groningen Gas Field, Shell Research and IBM Services, G. Joosten, J. Limbeck, G. Kaleta, S. Bourne, K. Nevenzeel, February 2019
4. Sanz, P. F., Lele, S. P., Searles, K. H., Hsu, S.-Y., Garzon, J. L., Burdette, J. A., Kline, W. E., Dale, B. A., and Hector, P. D. "Geomechanical analysis to evaluate production-induced fault reactivation at Groningen Gas Field." SPE Annual Technical Conference and Exhibition. Houston, TX: Society of Petroleum Engineers, 2015.
5. Lele, S. P., Hsu, S.-Y., Garzon, J. L., DeDontney, N., Searles, K. H., Gist, G. A., and Dale, B. A. "Geomechanical modeling to evaluate production-induced seismicity at Groningen Gas Field." Abu Dhabi International Petroleum Exhibition and Conference. Abu Dhabi, UAE: Society of Petroleum Engineers, 2016.
6. ExxonMobil Upstream Research Company, Suvrat Lele, JorgeGarzon, Sheng-Yuan Hsu, Nora DeDontney, Kevin Searles and Pable Sanz-Reherman, Groningen 2015 Geomechanical Analysis, Mar 2016

NAM

Title	**Groningen Seismological Models for Activity Rate Forecasting**	**Date**	June 2017
		Initiator	NAM
Autor(s)	Nora DeDontney	**Editors**	Jan van Elk Dirk Doornhof
Organisation	Upstream Research Centre, ExxonMobil	**Organisation**	NAM
Place in the Study and Data Acquisition Plan	Study Theme: Seismological Model Comment: The seismological model incorporated in the Hazard and Risk Assessment makes use of fundamental geomechanical models, with compaction as the driver for the seismic activity (Ref. 1 to 3). Alternative approaches to the forecasting of seismic activity have been explored. This report describes the development of a seismological model for the activity rate in the Groningen field, using the geomechanical model developed in URC (4 to 6). Both compaction and fault slip based seismological models are examined.		
Directly linked research	• Hazard Assessment • Geomechanical Studies		
Used data			
Associated organisation			
Assurance			

Groningen Seismological Models for Activity Rate Forecasting

June 2, 2017

Nora DeDontney

Table of Contents

Executive Summary 3

1.0 Introduction 5

1.1 Overview of Groningen seismicity 5

1.2 Probabilistic Seismic Hazard Analysis Activity Model 7

1.3 Geomechanical model input to the seismological model 7

1.4 Activity vs. strain partitioning models 10

2.0 Methods 13

2.1 Compaction data 13

2.2 Fault moment data 17

2.3 Maximum likelihood estimation of seismological model parameters 19

2.3.1 Specified Forms for the Poisson Process Model 20

2.3.2 Generic Poisson Process Methodology 22

2.4 Comparison of Activity Models 24

3.0 Results 25

3.1 Compaction Based Activity Models 25

3.1.1 Fit to field domain 25

3.1.2 Fit to the submodel domain 39

3.2 Fault Slip Based Activity Models 46

4.0 Discussion 57

4.2 Field Wide Compaction Based Models 57

4.1 Comparison of Compaction and Fault Based Models 58

4.1.1 Best Fault and Compaction based Models for Comparison 58

4.1.2 Comparison of Activity in the Near Term 60

4.1.3 Comparison of PGA Hazard Maps 63

5.0 Summary and Conclusions 64

References 67

Executive Summary

Seismic activity forecasts play a significant role in the production plan for the Groningen field. These forecasts are based on models that are calibrated to historical seismic activity, and many of these models can represent the historical seismicity observations equally well. However, when projected into the future, these models can yield very different activity forecasts, so it is important to consider a wide range of models when making a forecast and not be locked into one form at the expense of potentially more predictive models.

Activity forecasts are also a critical input to the Probabilistic Seismic Hazard Analysis (PSHA). Since the M_L 3.6 Huizinge event occurred in 2012 the regulator has required that hazard maps be generated and submitted for the production scenarios under consideration. To make hazard maps, a map of seismic activity is required that quantifies how many events are expected to occur over a given timeframe and their spatial distribution. An activity map does not include information about the expected size of events, as that information is a separate input into the PSHA. Whether events are dispersed over a large area or localized into high activity zones will affect the spatial distribution of Peak Ground Acceleration (PGA) in the hazard maps as well as the maximum PGA. For the purposes of this document we examined only PGA-based hazard maps (10% probability of exceedance in 50 years) without consideration of spectral accelerations at various structural periods or other values for probability of exceedance.

In tectonic settings, where overall seismicity rates are expected to be constant over the time frame of interest, the historical catalog is used to generate an activity map. In the case of induced seismicity, a constant seismicity rate cannot be assumed. Seismic events are related to gas production so the rate and spatial distribution of gas production should affect the activity in any given year. Therefore, a model is needed to relate production to seismicity. Production leads to subsurface deformations and changes in stress and these stress changes may result in tremors. A geomechanical model is calibrated to historical observations to capture the relationship between production and subsurface deformations and then a seismological model is created to relate the deformations to the observed seismicity. To make an activity forecast the geomechanical model projects subsurface deformations for a given production scenario (pore pressure evolution) and this is then fed into the seismological model.

The geomechanical model is based on the physics of deformation while the seismological model is a statistical correlation between the historical geomechanical quantity and the observed seismic activity. There are many forms that the seismological model could take and this report documents an exploration of those forms, an analysis of which are the best representations of the observed seismicity to date and a discussion of which are likely to be the most predictive. One of the options explored is the type of geomechanical quantity that is used as an input to the seismological model. Depending on the type of geomechanical model in use, the subsurface deformation can be represented by either reservoir compaction or the amount of slip that occurs on discrete faults.

NAM's Hazard and Risk Assessments for Groningen have historically been based only on activity forecasts using compaction as an input to the seismological model. The ExxonMobil Upstream Research (EMURC)

geomechanical model captures compaction across the entire field and fault slip over the 70% of the field area that is the most seismically active. Both compaction and fault slip based seismological models are examined. In the area where the fault slip geomechanical model exists, a fault slip based metric is found to yield a significantly better representation of the observed seismicity than a compaction based model. The best fault slip based seismological model forecasts lower activity rates over the next 30 years than a compaction based model similar to that used by NAM. Compaction and fault based models result in very different spatial distributions of seismic activity, but this has a relatively small effect on the resulting hazard map due to the fact that the Ground Motion Prediction Equations (GMPEs) act to disperse the hazard over a larger domain.

The faulted geomechanical model does not exist in the entire domain of the field, so currently only compaction can be used to develop a field wide activity model. A variety of forms were considered and the model currently used by NAM was found to be one of the better models. However, two other seismological models represent the historical data better, or nearly as well, but make substantially different forecasts about the seismicity rate in the near term. Given the importance of the activity rate forecast, and the near equality of the different model fits, at this time it is difficult to strongly favor one compaction based model over another.

Given that there is no physical basis to prefer one type of compaction based (or fault slip based) seismological model over another, multiple models should be carried forward, and weighted appropriately in a logic tree, so that an assumption of one form for the seismological model does not dominate the result.

1.0 Introduction

1.1 Overview of Groningen seismicity

The Groningen gas field is located in a tectonically quiet area of little to no historic seismicity. By the 1980s, some 20 years after first gas production in the area, tremors started to be felt in the vicinity of other nearby gas fields. The first seismic event to be detected in association with the Groningen gas field was in 1991. By that time, seismicity around the Northern Netherlands gas fields had increased and was understood to be a consequence of fault reactivation due to pressure depletion from gas production. From that time forward the Groningen seismic activity catalog shows a generally increasing number of events per year and an overall trend of increasing peak magnitude of events (Figure 1) up until recently when the number of events per year has started to decrease. The yearly production is also shown in Figure 1. There has been a clear correlation between the produced volumes and number of events since the year 2000. A large amount of the production prior to 2000 occurred without any seismicity, making any correlation with yearly production less clear.

As of January 1, 2017, 285 events of magnitude $M_L \geq 1.5$ have been observed within and near the Groningen field. 12 of those events occurred before April of 1995, when the installation of new surface seismic stations established catalog completeness down to M_L 1.5, with local areas of completeness down to ~M_L 1.2 (van Thienen-Visser et al., 2016). In addition to a surface array of seismometers operated by the Royal Meteorological Institute of the Netherlands (KNMI), there are also downhole arrays of geophones deployed in the reservoir interval that are operated by NAM (the operator of the field). The downhole arrays are able to detect smaller magnitude events than the surface array, but only in the immediate vicinity of the boreholes. While small magnitude data exists, it is not spatially and temporally complete so this study will focus only on $M_L \geq 1.5$ events recorded by the surface array since that catalog covers the full aerial extent of the field.

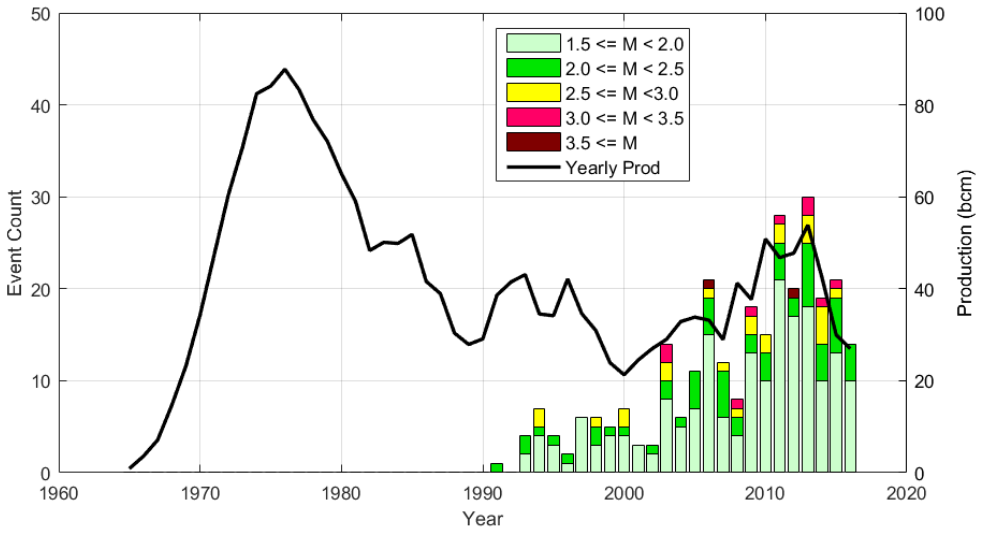

Figure 1: Number of events observed per year, categorized by magnitude (reported as local magnitude M_L) and yearly production (black line) to year end, 2016. A general correlation between production and number of events is apparent since the year 2000.

To understand the spatial distribution of seismic activity a map view of the events through the end of 2015 is provided in Figure 2. The field outline is shown as a maroon line plotted on a depth map of the top of the reservoir and the light blue squares are the surface seismic stations. Most of the seismic activity has been located in a large cluster towards the central-north end of the field. The two largest magnitude events observed to date, the August 2012, M_L 3.6 (M_W 3.4) Huizinge event and the M_L 3.5 Westeremden event, are located in the northwest of this cluster (red circles). This area with historically larger peak magnitudes and more frequent events is called the Loppersum region (named for the nearby town of Loppersum). Concerns about the potential hazard and risk in the area led to a large investment by NAM into a scientific program to better understand the seismicity and how the gas production plan affects the characteristics of the seismicity.

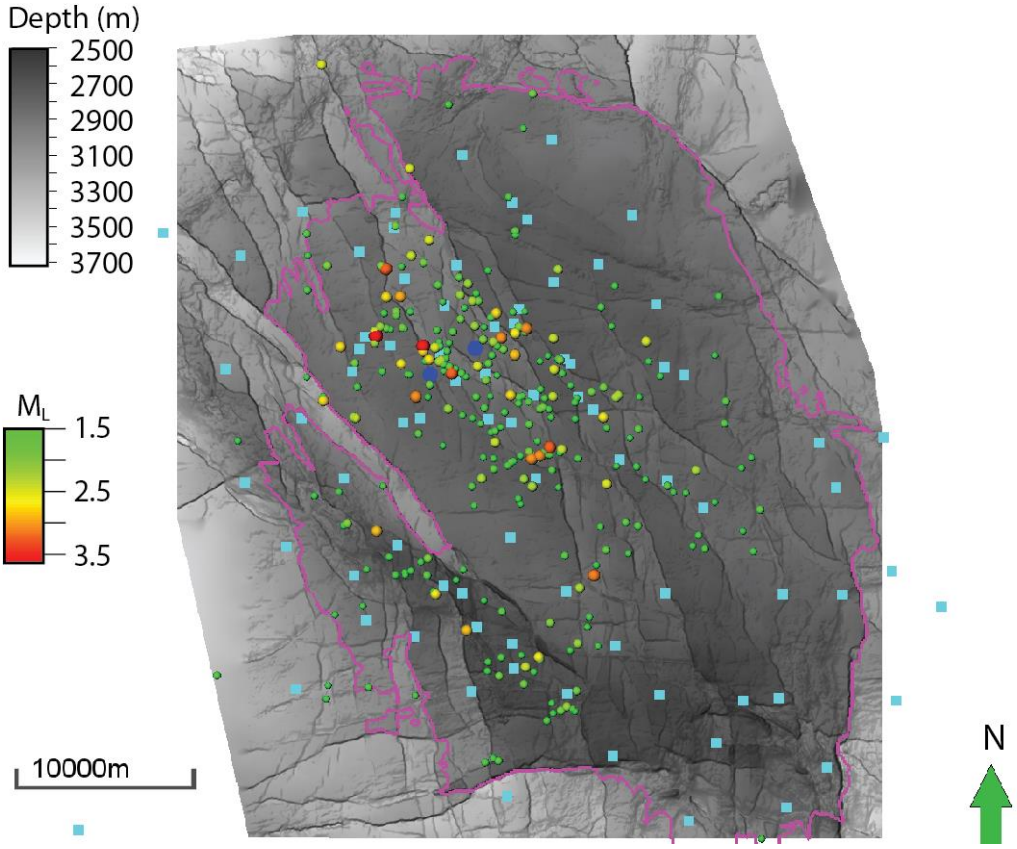

Figure 2: Seismic activity at the Groningen field, through end of 2015. The field is outlined in pink and the depth map is the top of the Rotliegend reservoir. Epicenters are circles and scaled/colored according to magnitude. Current surface seismic stations are light blue squares and the downhole array locations are dark blue circles. Event locations were obtained from the Royal Netherlands Meteorological Institute's website[1]. Lateral error in the location is estimated by KNMI to be ~1 km, while depth is assigned to be 3 km – within the reservoir.

[1] http://www.knmi.nl/kennis-en-datacentrum/dataset/aardbevingscatalogus

1.2 Probabilistic Seismic Hazard Analysis Activity Model

Since the 2012 Huizinge earthquake, the regulator requires that Probabilistic Seismic Hazard Analysis (PSHA) maps be submitted as part of the production plan. One of the three input components of PSHA is the forecasted number and spatial distribution of earthquakes (the activity model). The other two components are (1) the ground motion prediction equations (how much shaking may occur at a given distance from a given magnitude event) and (2) the magnitude frequency distribution specified by the Gutenberg-Richter b-value and a maximum magnitude. All of these components are important in the PSHA and are the subject of ongoing investigations (E.g., Coppersmith et al., 2016; Bommer et al., 2016). The focus of this study is the activity model, which is decoupled from the earthquake magnitude. Activity only captures the number of events at or above a threshold magnitude (here M_L 1.5) and their spatial distribution.

PSHA is based on a grid of source locations of spatial coordinates, $\boldsymbol{x}$, each with their own activity rate, λ

$$\lambda(\boldsymbol{x}) = \frac{\#\ events}{Area * \ year}$$

Activity is strictly a number of events expected per unit area per year. A map of λ values (an activity map) contains information about the total expected number of earthquakes per year, as well as the spatial distribution of the sources. An integration over the area of the map results in the total number of expected events in a given year.

In conventional PSHA analysis this rate is not expected to change in time, but due to the non-stationary (changing with time) nature of induced seismicity, the rate can also be a function of time, $\lambda = \lambda(\boldsymbol{x}, t)$. The PSHA is performed for a snapshot of activity at a specific point in time, but the time dependence is crucial for fitting a seismological model to the observations and projecting an activity rate into the future.

In order to make an activity map there needs to be an understanding of what is causing the earthquakes. The Groningen induced earthquakes are the result of deformation and stress changes in the subsurface and these changes are being driven by the gas production. Therefore, different production plans (total volume and spatial distribution of withdrawal) should result in different subsurface stress changes and seismicity. NAM supplies hazard maps for the different production plans under consideration and this requires a methodology to translate production into seismic activity. A geomechanical model is calibrated to historical observations and captures the relationship between production and subsurface deformations and then a seismological model is created to relate the deformations to the observed seismicity. The seismological model is a statistical model (no basis in physical equations) and it translates a geomechanical quantity (reservoir compaction or fault slip) into seismic activity.

1.3 Geomechanical model input to the seismological model

A geomechanical quantity is a better basis for a seismological model because stress and deformation are closer to the true cause of seismicity than production alone. Production causes changes in stress and once the stress exceeds the strength of the fault an earthquake occurs. While production is the fundamental driver that leads to geomechanical changes, if the production itself is used as the basis of the seismological

model then geologic heterogeneities are difficult to account for. Geomechanical models are able to account for differences in the material properties throughout the field and the geometry of faults so geomechanical quantities are a better basis for a seismological model than production or pore pressure.

Since 2013 ExxonMobil Upstream Research Company (EMURC) has invested resources into developing a geomechanical model of the Groningen field. EMURC has used the commercial finite element program, ABAQUS, to develop a quasi-static 3D geomechanical model covering large portions of the field and including ~90% of the faults mapped in those areas (Lele et al., 2016). The 3D model imposes pore pressure changes in a global model that does not explicitly include faults (reservoir layers are draped across faults to approximate the pre-existing geometry) and extends far beyond the boundaries of the field. The prescribed pore pressures are taken from the NAM provided reservoir simulation model that is history matched to the production and forecasts future pore pressure changes for each production scenario. The global model provides a measure of the compaction across the domain of the entire field.

The deformations calculated in the global model are then applied as boundary conditions to three overlapping submodels that explicitly include the faults and cover domains smaller than the field. The faults are modeled as contact surfaces that are able to slide past one another. The complex fault geometry (e.g. surface roughness) cannot be fully captured in these submodels, but the spatially variable average strike and dip of the fault are well represented. Both the global model and the submodels have porosity (and thus location) dependent elastic moduli. The porosity variation throughout the field is prescribed by the geologic model and the elastic moduli dependence on the porosity is constrained by lab data. Figure 3 shows an example of the slip magnitude that accumulates on the modeled faults in one of the submodels.

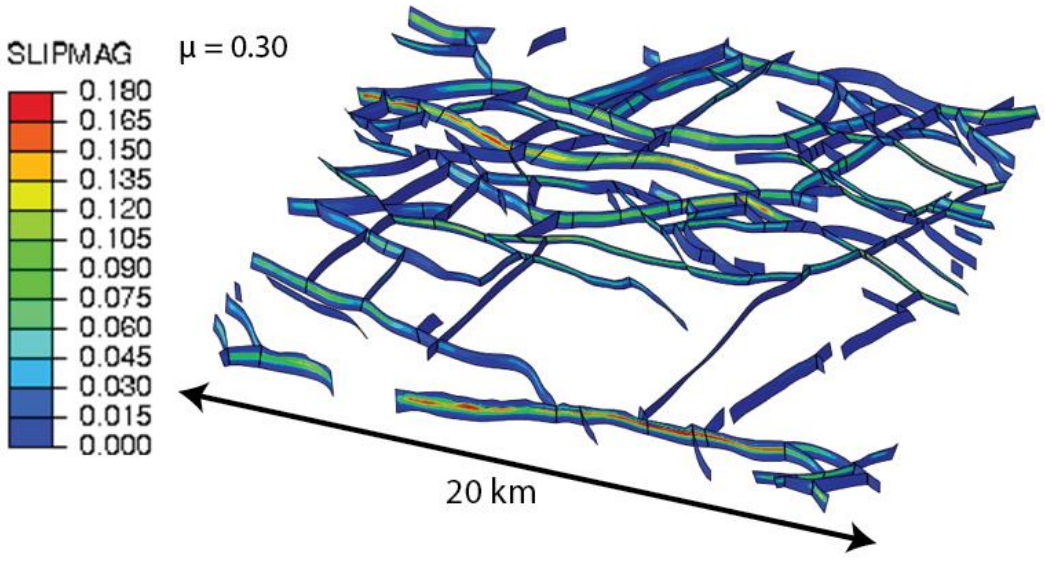

Figure 3 Oblique view of one of three geomechanical submodels. Contoured value is the magnitude of slip for a friction value of $\mu = 0.30$ on the fault.

The geomechanical models first developed in 2013 (Sanz et al., 2015) have undergone substantial upgrades and modifications during 2015. Both the 2013 and 2015 models have the same global model but

the 2015 submodels are substantially different from the 2013 submodels. In the present day subsurface, pre-existing slip on the faults has resulted in offsets of the layers across the faults. These offsets are captured in the 2015 submodels but not in the 2013 models (see Lele et al., 2016 for a complete description of the geomechanical model). Additionally, in the 2013 version there were 2 submodels and the 2015 model has 3 submodels so more of the field is represented (submodel 3 is outlined in green in Figure 4a). The 2015 submodel changes have resulted in a different model behavior than what was observed in the 2013 submodels. These changes have partially motivated the recent focus on developing a geomechanical based activity model, as opposed to a strain partitioning model approach, which will be discussed in more detail in the next section.

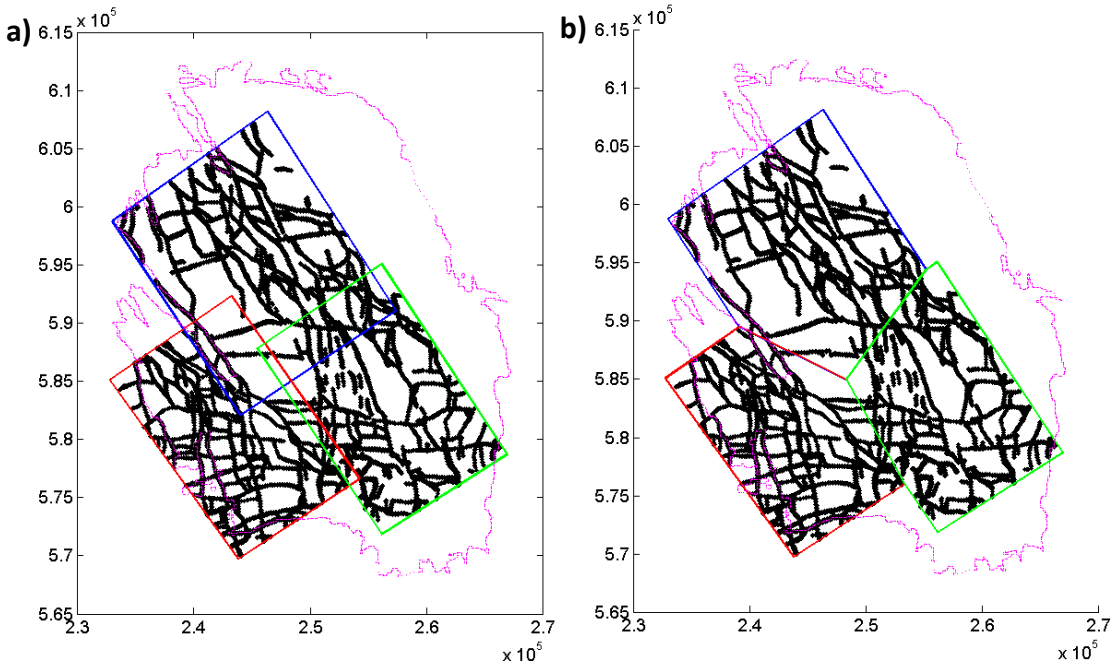

Figure 4: (a) Location of submodel domains in relation to the field outline. Blue – submodel 1; Red – submodel 2; Green – submodel 3 (only in 2015 study). Black lines are the faults included in the submodels. (b) Due to the overlap of the submodels, only some data is taken from each submodel to prevent data duplication in the merged dataset. The boundaries used to merge the data are shown here.

While the geomechanical models are quite complex, there are a limited number of outputs that can be used as a basis for a seismological model. Reservoir volume change and fault slip are the candidate output fields. A measure of reservoir volume change due to depletion is obtained from the global model that does not contain faults. Under uniaxial strain boundary conditions (no lateral deformation) volume change is expressed strictly as a change in reservoir thickness (a map of compaction). If the geomechanical model contains faults then slip can evolve on these faults over time in response to the specific reservoir conditions and fault orientation at that point in space. The submodels overlap each other in space so when combining the submodel results only some data is taken from each submodel to prevent data duplication. The boundaries used to merge the data are shown in Figure 4b. Once a fault slips, either the seismic moment (slip*area*shear modulus) or the dissipated fault energy (slip*shear stress) can be used as a geomechanical input. Qualitatively there is little difference between the moment and energy metrics

because they are both based on the fault slip and are very well correlated over time. Therefore, only fault moment is considered in this study with the knowledge that results based on dissipated energy are nearly identical.

Both compaction and fault moment based seismological models are examined here. Each has advantages and disadvantages but the resulting seismic hazard maps (in terms of Peak Ground Acceleration, PGA, with a 10% probability of exceedance in 50 years) are not drastically different. Currently, NAM implements a compaction based approach (Bourne and Oates, 2015a,b) so while EMURC does not have the same compaction model as NAM, a compaction based fit allows for more direct comparison with the Bourne and Oates (2015a,b) results. Geomechanically modeled fault slip is more similar to earthquake motion than compaction, so there are theoretical benefits to using a fault moment based seismological model. It should be noted that submodels do not cover the entire extent of the field so the fault slip metric is difficult to implement for a complete field wide forecast.

1.4 Activity vs. strain partitioning models

Once a geomechanical model input quantity has been determined the seismological model needs to correlate that quantity with observed seismicity. The quantity can either be correlated with the number of events or the size of the events. A correlation with the number of events provides the activity map that is needed for the PSHA and is the focus here. An alternative relationship would derive a coefficient of proportionality between the modeled quantity and the observed energy/moment release. This type of model is called a strain partitioning model. To derive an activity map from a strain partitioning model would require assuming an average moment release per event (via the Gutenberg-Richter relationship) to translate moment release per year into events per year.

In 2013 a strain partitioning methodology was used to relate the EMURC geomechanical output to the observed seismicity (Sanz et al, 2015). The modeled dissipated fault energy was compared to the observed seismic energy release in the two submodel domains. The motivation behind this approach is the idea that where the model predicts abundant slip, abundant slip should be observed. In 2013 this approach worked well as the same partitioning coefficient could be used for both submodel 1 and 2 to relate the observed seismic energy release to the model energy dissipated by fault slip. However, this uniform partitioning coefficient no longer holds for the 2015 submodels. A comparison of columns 4 and 5 in Table 1 shows that 89% of the **observed** seismic moment release was in the submodel 1 domain but only 44% of the **modeled** moment was in submodel 1. (The percentages do not differ by more than 1% if Table 1 is presented as energy rather than moment).

Table 1: Comparison of earthquake observations and model results in each of the three geomechanical model submodel domains as of Jan 1, 2016. The 2015 model shows a poor correlation between observed and modeled moment. The model results are presented as the moment that has accumulated after some reference point in time, specified by the year. SM refers to submodel number.

		Observations		Model Results	
		# of Events	Moment of Events	Moment of Model (1990)	Moment of Model (1967)
Absolute Values	SM1	171	1.357e15	1.016e16	1.942e16
	SM2	47	9.486e13	6.623e15	1.241e16
	SM3	27	8.165e13	6.240e15	1.200e16
Percentages	SM1	70%	89%	44%	44%
	SM2	19%	6%	29%	28%
	SM3	11%	5%	27%	28%

The spatial distribution of modeled and observed moment is shown in Figure 5. Model and observations are presented as heat maps with a spatial smoothing applied to the model and observations (the method used to spatially smooth the data is discussed in section 2.2). Both model and observation have the most moment release in the submodel 1 domain (blue box outline) but if submodel 1 is simply divided into 4 quadrants, the equality of ranking of the quadrants breaks down.

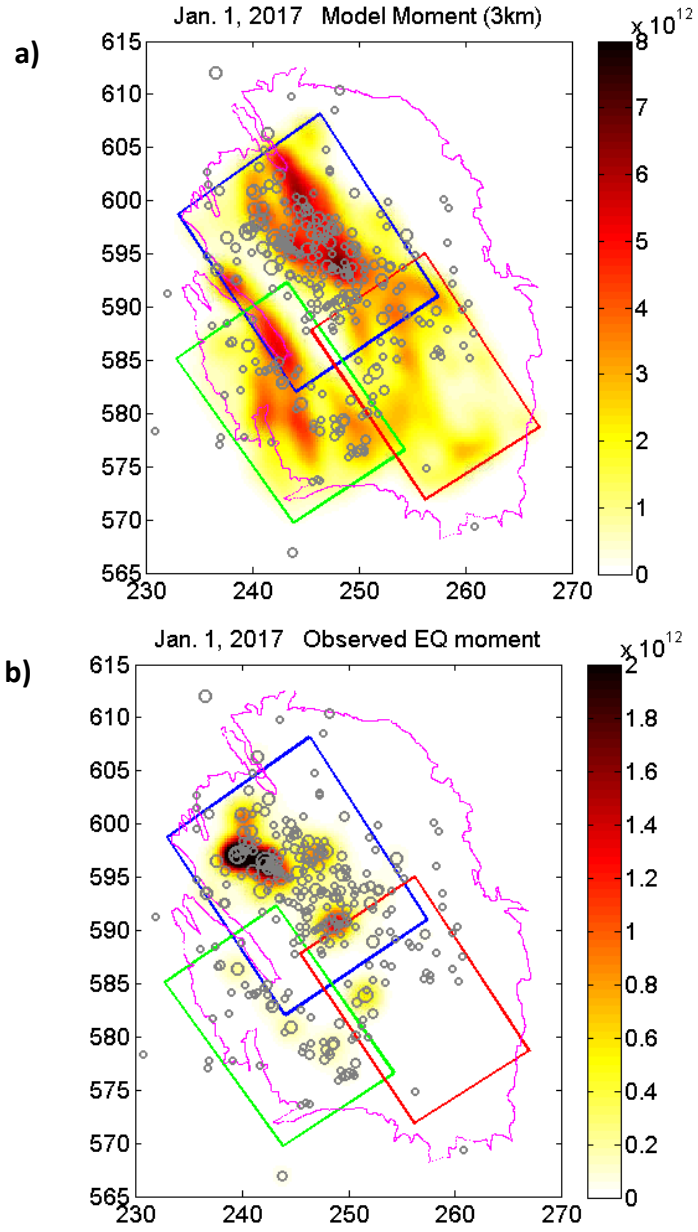

Figure 5: Comparison of (a) modeled moment release and (b) observed seismic moment release. A 3 km kernel is used to distribute the modeled and observed moment over a spatial domain. Observed moment release is of all observed earthquakes and model moment release is all fault slip moment since Jan 1 of 1990. Blue, green and red boxes are the submodel 1, 2 and 3 domains respectively. Maroon line is the field outline. Gray circles are all observed events of $M_L \geq 1.5$ as of January 1, 2017, and their size is proportional to magnitude. Color shading is moment release per 250 m x 250 m gridpoint.

The poor spatial correlation between modeled and observed moment release illustrates that the quasi-static geomechanical model cannot capture the true heterogeneity or the processes that take place during an earthquake. Since several components of the physics of earthquakes cannot be included in the quasi-static model it is not reasonable to expect the model to fully capture the time release of energy in the subsurface (i.e. predict location and magnitude of earthquakes). However, the model well represents

where faults are being stressed. The amount of slip that evolves on the fault indicates if a fault is being stressed a lot or a little and if it is over a long duration or a short duration. An earthquake is more likely to nucleate in an area that is highly stressed so the geomechanical model could be a good proxy for the availability of earthquake nucleation sites. Where the model predicts fault slip we should expect to see more events. The physics of the rupture process determines how big the earthquake is, and the quasi-static geomechanical model cannot capture these effects. For these reasons the quasi-static modeled fault slip/energy is compared to the observed **number** of events rather than the observed **moment**.

2.0 Methods

2.1 Compaction data

Depletion of the Groningen reservoir results in a decrease in pore pressure, and this causes the reservoir rock to compact over time. The amount of compaction depends on the magnitude of pore pressure reduction and the porosity dependent elastic moduli at a given position in the reservoir. The reservoir does not have infinite lateral extent so there will be lateral movement in response to the depletion, but the horizontal displacements are small compared to the vertical displacements that are solely considered here. The top and bottom of the reservoir are defined layers in the global geomechanical model so the displacement of every point can be evaluated at any year. The top of the reservoir will move down due to depletion and the bottom of the reservoir may also move in response to the depletion. The compaction, $c(\boldsymbol{x}, t)$, at spatial positions $\boldsymbol{x}$, and time t, are evaluated by $c(\boldsymbol{x}, t) = \Delta u_z^{bottom}(\boldsymbol{x}, t) - \Delta u_z^{top}(\boldsymbol{x}, t)$, where u_z are the vertical displacements and the resulting compaction is a positive quantity.

The displacements are only calculated by the geomechanical model for January 1 of each calendar year. Therefore, the 2015 compaction is simply the compaction from January 1, 2015, and the 2015 compaction derivative is the difference between the January 1, 2016 and the January 1, 2015 compaction values. The activity for the year, 2015, is calculated from those 2015 values. The choice could also be made that the compaction derivative for the year 2015 is the difference between the January 1, 2015 and the January 1, 2014 compaction values. In that case only past production (and not current or future production), influences the seismicity.

In addition to bulk values that represent the entire year, the compaction and compaction derivative values at specific dates throughout the year are needed to estimate the parameters of the seismological model. To determine the compaction at a point in space during the year, a linear interpolation between January 1 values, at the specific point in space, is performed. This linear interpolation neglects the seasonal swing in production that has occurred historically due to the high production of gas during the cold winter months, but this effect will be small and is not expected to significantly change the results. The derivative of compaction for July 1 is estimated by centered difference between the compaction values of the next January 1 and the previous January 1. The compaction derivative at any other date is then computed by linear interpolation of these July 1 estimates. The choice of a centered difference was made to maximize accuracy.

Figure 6a shows how the total reservoir volume has changed in the global geomechanical model and is expected to change over time for a given production scenario (here the 27 bcm case is shown). In 2017, ~2/3 of the total expected compaction has occurred. Seismic activity started in the mid 80's and picked up in the mid 90's, after ~1/3 of the compaction had occurred. The derivative of this curve, the rate of volume change, is shown as the red line in Figure 6b. The onset of seismicity did not correspond to the time of highest compaction rate (blue circles - note that the few events in the 80's and early 90's were not well recorded and are not included in the catalog shown). Figure 6c shows the cumulative number of events in each year vs. the total volume change. Each year is shown as one point and the last point is for 2017, so there is no increase in earthquakes because the 2017 catalog is not included. A clear relationship exists that could be fit with a variety of functional forms.

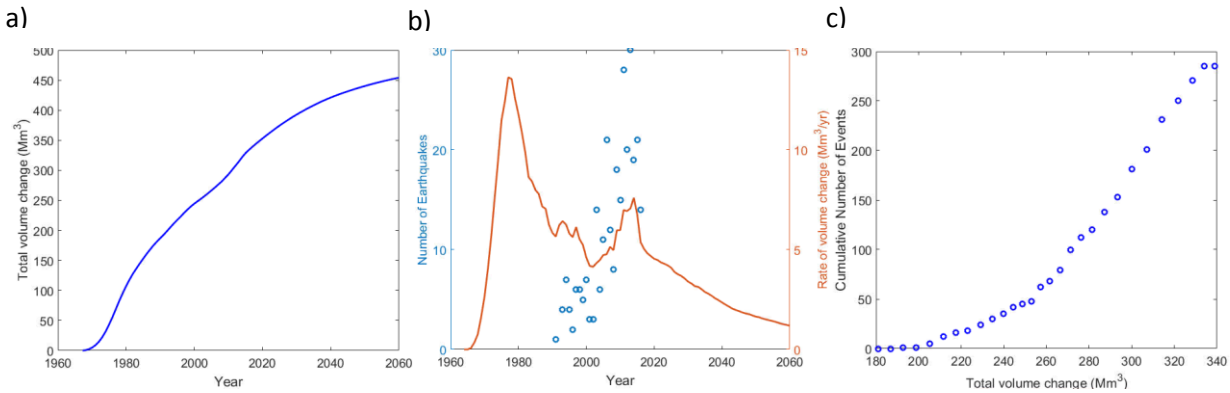

Figure 6: Features of the field wide change in reservoir volume. (a) Total reservoir volume change increases monotonically with time. (b) Derivative of volume change (red line) is not monotonic. Blue circles are the number of $M_L \geq 1.5$ events observed per year. (c) Cumulative number of $M_L \geq 1.5$ events vs. total volume change suggests a non-linear relationship between compaction and activity.

It is clear from Figure 6b that a large amount of volume change occurred before the onset of seismicity. This suggests that a threshold was reached and compaction past this threshold may result in seismicity, but compaction less than this threshold may not. The threshold can either be specified as a time or a compaction value. Figure 7 shows the compaction at the point in space and time of each observed earthquake. The size and shading of each circle is proportional to the magnitude of the observed event and the gray line is the maximum compaction value at any point in the model domain. Most events occur in areas where $c \geq 0.18$ m and after 1990 so either could be used as a threshold.

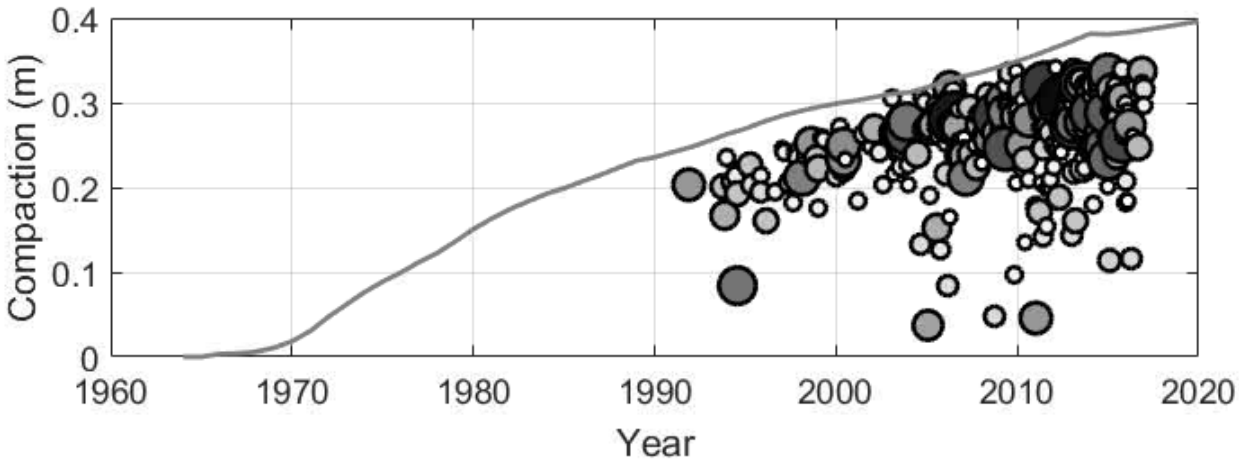

Figure 7: Compaction at each point in space and time that an earthquake was observed within the field outline. Shading and size of circle is proportional to the magnitude of the observed event. Gray line is the maximum compaction value at any point in the model within the filed outline. Model is referenced to the beginning of production, 1965.

Once a threshold is specified, all compaction values are in reference to that threshold value. If the threshold is specified as a year (e.g. 1990) then the January 1, 1990 compaction value at each point in space is subtracted from all subsequent years (the model is referenced to 1990 values). When a forward derivate is used, the derivative value in 1989 and all previous years is set to zero while the derivative for 1990 and later is unchanged. If a threshold value is specified (e.g. 0.18 m) then that value is subtracted from the compaction at every point in space and time. Negative referenced compaction values are set to zero and then the derivative is calculated. Note that this process can result in earthquakes occurring at locations with compaction values of zero, which results in difficulties when performing the fits (discussed in more detail later).

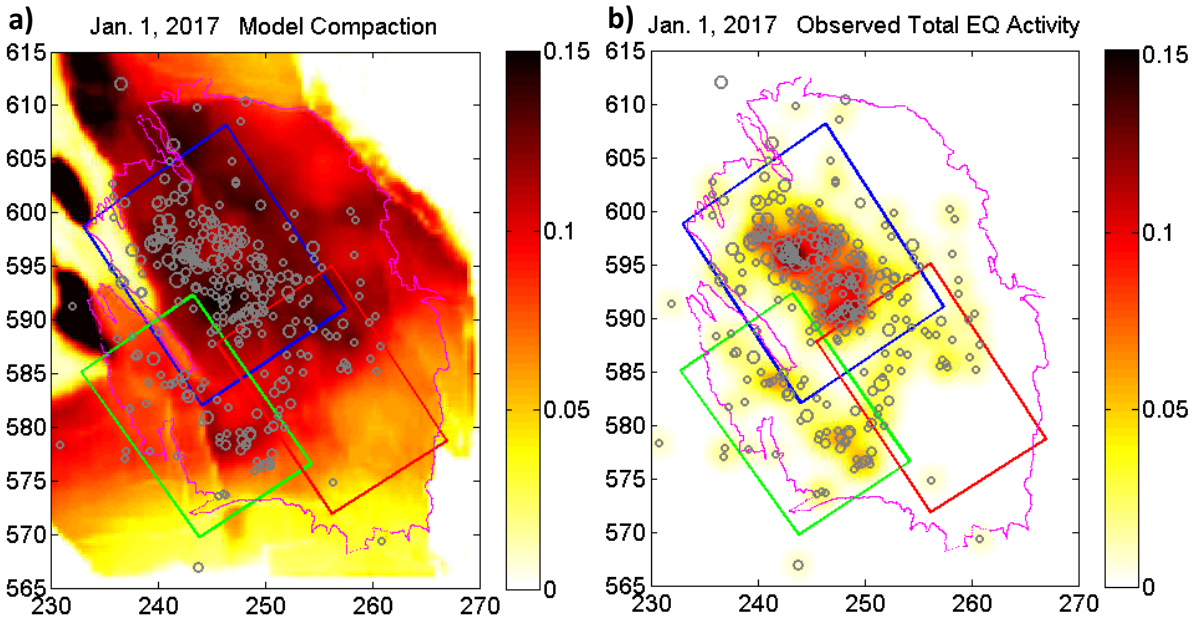

Figure 8: Comparison of (a) modeled reservoir compaction since January 1 of 1990 and (b) observed seismic activity. A 3 km kernel is used to distribute the observed activity over a spatial domain. Blue, green and red boxes are the submodel 1, 2 and 3 domains respectively. Maroon line is the field outline. Gray circles are all observed events as of January 1, 2017, and their size is proportional to magnitude. Color shading is compaction (m) in (a) and events per 250 m x 250 m grid in (b).

Figure 8a shows the January 1, 2017 compaction value referenced to 1990 and Figure 8b shows the spatial distribution of seismic activity. The compaction is distributed over a large spatial area but seismic activity is highly localized in the Northwest, an area of generally high compaction. The activity heat map was generated using a 3 km Gaussian kernel to distribute the activity over a spatial area (described in more detail in section 2.2).

On the northern edge of the western boundary of the map in Figure 8a there are three areas of very high compaction. These large amounts of compaction are due to large pore pressure reductions in the reservoir model in those areas. These are present in the 2015 reservoir model but they were not present in some of the previous versions of the reservoir model and are thought to be spurious. Hence these areas are ignored in the calculations going forward by fitting the seismological model only within the outline of the field or within the domain of the three submodels. This choice trims away the anomalously high compaction areas so they do not affect the calculation.

The map of compaction shown here is different from the compaction model used by Bourne and Oates (2015a,b). While this paper presents a forward modeling approach, Bourne and Oates (2015a,b) perform an inversion of surface subsidence measurements to determine the spatial distribution of compaction. Because the surface subsidence approximates to a 3 km low-pass filtered response to subsidence at the reservoir, Bourne and Oates (2015a,b) investigates the effect of smoothing the compaction model. The

geomechanical model presented here provides a higher resolution and smoother dataset so additional smoothing of the compaction model is not examined.

2.2 Fault moment data

Figure 5 and Figure 9 illustrate the differences in the spatial distribution of modeled seismic moment and the observed seismic moment and activity. The modeled seismic moment is distributed spatially using a Gaussian of specified spread where the kernel size (3 km in Figure 5 and Figure 9) refers to the radius of the 3 sigma distance in the distribution. The distribution linearly tapers to zero from the 3 sigma distance to the 4 sigma distance to prevent moment from spreading outside of the near field area, making it pseudo-Gaussian. The moment release at every node on a fault surface is moved to the nearest point on a 250m x 250 m grid and then the sum of the moment release at that point is distributed over the nearby region with the pseudo-Gaussian. All values are scaled appropriately to ensure that the volume under the pseudo-Gaussian equals the total moment release. This same process of spatial distribution is used for observations of moment released via earthquakes or for activity. In the case of observed moment, each earthquake has its own Gaussian and the volume under the Gaussian is the seismic moment. In the case of the activity map, all earthquakes are weighted equally and the volume under each Gaussian is one.

The use of the Gaussian for the earthquake observations allows for easier visualization of the data. For the geomechanical model data, the spatial distribution serves a functional role as well. Distribution of the moment in this manner makes visualization of the model results easier but more importantly compensates for a number of uncertainties and makes it possible to fit a statistical model. The reasons for applying a spatial distribution are as follows:

1. Not all faults are captured in the geomechanical model because not all faults can be imaged in the seismic data. Additionally, there is a limit to the amount of detail that can be included in the geomechanical model. Slip could be occurring on a parallel fault strand not included in the model so distributing the moment release over an area is one way to capture this uncertainty.
2. In the process of fitting the seismological model each earthquake epicenter is used to determine the moment release at the point in space and time of the event. However, there is a large amount of error in the earthquake locations ($\pm$ 500m-1km) so earthquake epicenters rarely locate onto mapped faults. This results in an estimated moment release of zero at almost every observed earthquake epicenter, which would make it impossible to fit a statistical model. Distributing the modeled slip over a spatial area greatly reduces the number of locations that will have no modeled moment release.
3. Due to the large number of faults in the field there are often multiple faults within the error ellipse of a given observed event location. In reality the observed event could have occurred on any number of faults so the best proxy for how much modeled moment release occurred at a location is an average of the nearby modeled moment release on multiple faults where the average is weighted by distance from the observed earthquake epicenter. The method implemented here, distributing the modeled moment release and querying the result at a point, achieves the same end result as querying a number of points around an observation location.

As discussed in section 1.3, there is a poor correlation between the spatial distribution of modeled seismic moment release and the moment of observed earthquake events (Figure 5). In contrast, Figure 9 illustrates a good spatial correlation between modeled moment and observed activity. For example, the geomechanical model captures the diffuse nature of the seismicity observed in submodel 1 (blue box outline) and it also captures the secondary lineament of seismicity observed in submodel 2 (green box outline). However, there are a few places where the geomechanical model predicts some amount of seismicity but none has been observed (southern end of submodel 3, red outline). This mis-match does not mean that the fault moment data should not be used as a predictor of seismicity because the other potential input data, compaction, also would forecast activity in the seismically quiet area to the south.

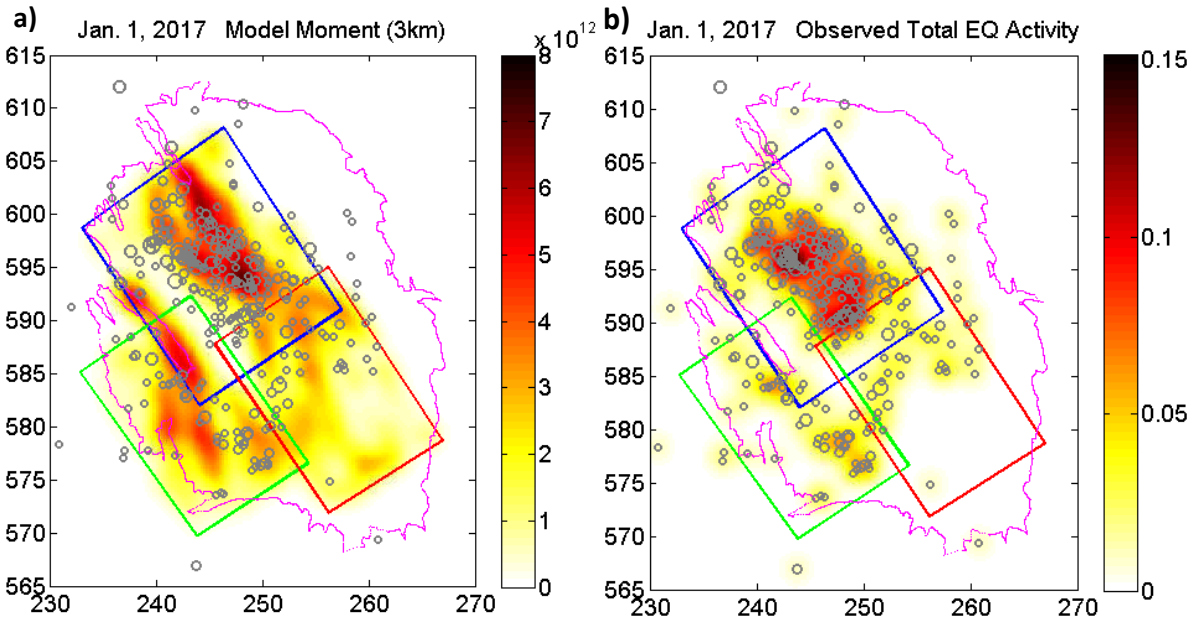

Figure 9: Comparison of (a) geomechanical model moment release and (b) observed seismic activity. A 3 km kernel is used to distribute the modeled moment and observed activity over a spatial domain. Observed activity is of all observed earthquakes and model moment release is all moment since Jan 1 of 1990. Blue, green and red boxes are the submodel 1, 2 and 3 domains respectively. Maroon line is the field outline. Gray circles are all observed events as of January 1, 2017, and their size is proportional to magnitude. Color shading is moment release per 250 m x 250 m grid point or events per 250 m x 250 m grid point.

Similar to the compaction data, a reference time or reference value is used to analyze the modeled moment release data. Slip initiates soon after the start of production in the geomechanical model, but earthquakes are not observed until many years later. To help determine a relevant threshold Figure 10 shows the moment release at each point in space and time that an earthquake was observed (similar to Figure 7 except for moment rather than compaction).

Modeled fault moment is evaluated at January 1 of each year. Similar to compaction, moment and moment derivatives are linearly interpolated to evaluate quantities throughout the year. The activity for a given year is based on the January 1 moment release value and the derivative of moment release over the year (difference between the January 1 value and the January 1 value of the following year).

Similar to compaction, if the threshold is specified as a year (e.g. 1990) then the January 1, 1990 slip value at each node in the geomechanical model is subtracted from all subsequent years and the spatial distribution of moment is recalculated. Additionally all derivatives for prior years are set to zero. If a threshold amount of slip is specified, then that amount of slip is subtracted from the time history of every fault node. All slip values less than zero are then ignored (set to zero) and the spatial distribution of moment release is calculated as well as the derivatives of moment release.

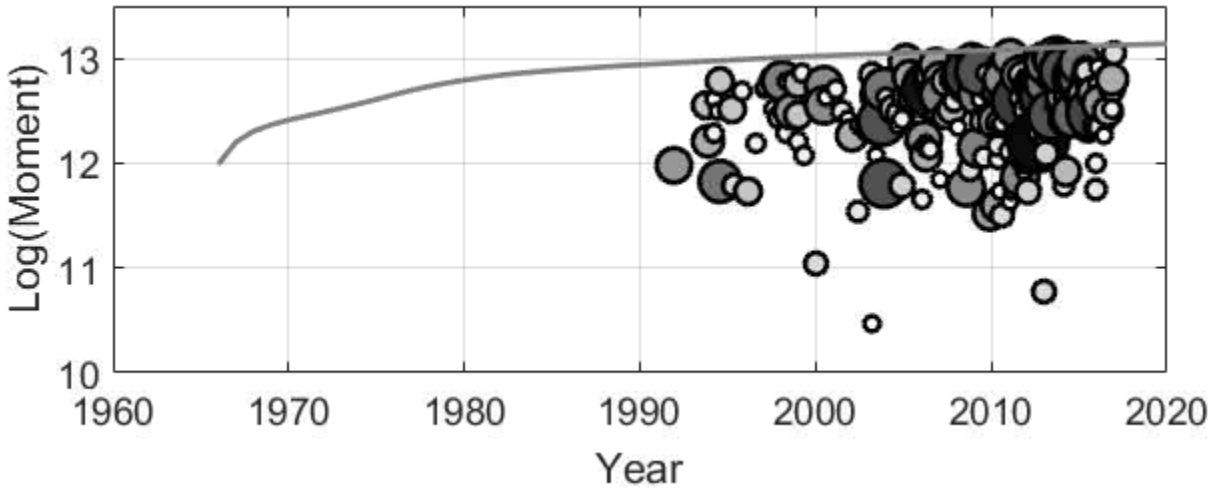

Figure 10: Modeled moment release at each point in space and time of observed earthquakes within the filed outline. Shading and size of circle is proportional to the magnitude of the observed event. Gray line is the maximum moment release value at any point in the model within the field outline. Model is referenced to the beginning of production, 1965.

2.3 Maximum likelihood estimation of seismological model parameters

Compaction and moment release maps are sourced from very different data but they are treated identically when fitting a seismological model. For both types of input data an equation (the seismological model) is used to relate the activity rate (variable in space and time) to the input geomechanical data (also variable in space and time). The geomechanical input used in the derivations below is the reservoir compaction, $\boldsymbol{c}$, but a similar derivation can be followed for fault moment, $\boldsymbol{m}$.

Earthquake occurrence is assumed to be a Poisson process and a maximum likelihood estimation (MLE) is used to determine the coefficients of the seismological model. This methodology incorporates the spatial and temporal aspects of each individual observed earthquake. The analysis is based on the region of interest, *A*, the 2D activity map, $\lambda(\boldsymbol{x}, t)$ (where t is time and $\boldsymbol{x}$ is the position in the field), and the activity at each point in space and time when an observed earthquake occurred, $\lambda(\boldsymbol{x_i}, t_i)$, for each of N earthquakes that occurred over a timespan $t_s \leq t \leq t_f$.

When performing a MLE a functional form for $\lambda(\boldsymbol{x}, t)$ is specified and the parameters that maximize the likelihood function are determined. The form chosen for λ and the optimized parameter values are the seismological model.

Following the derivation in Bourne and Oates, 2015a, the likelihood function, *L*, is

$$L = exp\left(-\int_A \int_{t_s}^{t_f} \lambda(\boldsymbol{x}, t) dt dA\right) \prod_{i=1}^{N} \lambda(\boldsymbol{x_i}, t_i)$$

Maximizing the product sum in the above equation can be computationally cumbersome so it is common practice to take the log of the likelihood function. The maximum of a function and the maximum of the log of the function occur at the same value so this simplification is accurate. The result is that the log-likelihood function, l, is maximized to determine the best fit parameters

$$l = -\int_A \int_{t_s}^{t_f} \lambda(\boldsymbol{x}, t) dt dA + \sum_{i=1}^{n} \log \lambda(\boldsymbol{x_i}, t_i)$$

$$l = -\Lambda_0 + \sum_{i=1}^{n} \log \lambda(\boldsymbol{x_i}, t_i) \qquad (eqn. 1)$$

Where Λ_0 is the expected total number of earthquakes in an area, over a time window, $t_s \leq t \leq t_f$, defined as

$$\Lambda_0 = \int_{t_s}^{t_f} \int_A \lambda(\boldsymbol{x}, t)\, dA\, dt$$

Two time windows are used for the MLE analysis. One time window captures the observed earthquakes and one window captures a time of seismic quiescence. The catalog of $M \geq 1.5$ events is complete starting in April of 1995, so one time interval is $1995.25 \leq t < 2017.0$. All events in 2016 are included in the analysis but no 2017 events. The second time interval used is $1965 \leq t \leq 1988$, a time when there were no observed earthquakes. Using both of these time windows constrains the model to have low activity in the early years and high activity later. Without this constraint (and more discussed later) the best fit model can predict a large amount of activity at a point in time when it is known that there was no activity. The first recorded events started in the early 90's but it is possible that there were small events, larger than M_L 1.5 but small enough to not be noticed, before the events of the early 90's so this time frame is not included in the analysis and nothing is assumed about the number of events between January 1 of 1988 and March 31 of 1995.

2.3.1 Specified Forms for the Poisson Process Model

To perform the MLE it is necessary to specify a form for λ, because without this, it is not possible to solve for the terms in the log-likelihood equation. One approach is to start from the observation that there is a nonlinear relationship between the cumulative event count and the reservoir volume change, ΔV (Figure 6c). The volume change can also be expressed as the integral of compaction over an area, A.

$$\Delta V(A) = \int_A \boldsymbol{c}\, dA$$

In the case of uniform compaction, this relationship simplifies to $c = \frac{\Delta V}{A}$. The nonlinear relationship between the total number of events between time t_s and t, $\Lambda(t_s, t)$, and the volume change may be captured with the use of an arbitrary function, f, in the following equation:

$$\Lambda(t_s, t) = \Delta V \, f\left(\frac{\Delta V}{A}\right)$$

Dividing this by the area provides the local total event count, $\Lambda_{local} = \Lambda/A$, in units of events per m^2

$$\Lambda_{local}(t_s, t) = \frac{\Delta V}{A} \, f\left(\frac{\Delta V}{A}\right) = c \, f(c)$$

The total activity over the field is then

$$\Lambda(t_s, t) = \int_A \Lambda_{local}(t_s, t) dA = \int_A cf(c) dA$$

The expected total event count is also related to the local activity rate by the following equation

$$\Lambda_0(A, t_0, t_s) = \int_{t_s}^{t_0} \int_A \lambda(\boldsymbol{x}, t) \, dA \, dt$$

If we assume that the nonlinear relationship holds over any area, then equating the expected number of events and the observed number of events suggests that the local activity rate should be

$$\lambda = \frac{d\Lambda_{\text{local}}(t_s, t)}{dt} = \frac{d\,(cf(c))}{dt} = \dot{c}[f(c) + cf'(c)]$$

With the above equations, the functional forms for the event count and local activity rate can be determined and those forms examined are presented in Table 2. Shell has used the exponential form for their seismological model and the above derivation shows where the Shell form for λ comes from.

Table 2: Relationship between the total event count, Λ_0, and the local activity rate, λ, for various functional forms of the nonlinear relationship

	f	Λ_0	λ
Linear	α	$\int [c\alpha]_{t_s}^{t_f} \, dA$	$\alpha\dot{c}$
Quadratic	$\beta c + \alpha$	$\int [\beta c^2 + \alpha c]_{t_s}^{t_f} \, dA$	$2\beta c\dot{c} + \alpha\dot{c}$
Cubic	$\gamma c^2 + \beta c + \alpha$	$\int [\gamma c^3 + \beta c^2 + \alpha c]_{t_s}^{t_f} \, dA$	$3\gamma c^2\dot{c} + 2\beta c\dot{c} + \alpha\dot{c}$
Exponential	$\alpha e^{\beta c}$	$\int [c\alpha e^{\beta c}]_{t_s}^{t_f} \, dA$	$\alpha e^{\beta c}\dot{c}\,(1 + c\beta)$

The forms of these equations pose some numerical challenges depending on the method implemented. If a reference year is chosen (e.g. 1990), then the 1990 compaction values are subtracted from the total

and there is a non-zero amount of compaction and compaction derivative at every point in space at the time of an earthquake (since all earthquakes considered occurred after 1990). Therefore there is a non-zero λ at every event location. However, this is not the case if a reference value is chosen, (e.g. 0.15 m). From Figure 7 it is apparent that there are events that occurred at compaction values less than 0.15 m. If the model is referenced to 0.15 m then there are earthquakes that occur at a point in space with the relative compaction and compaction derivative terms equal to zero. If this occurs then $\lambda = 0$ at those points and this results in an inability to calculate the log-likelihood because the log of zero is infinite. The same problem arises if moment is used instead of compaction.

To address the ill-posedness, a constant, δ, is added to each equation for λ in Table 2. This ensures that there is always a small background activity rate at every location and allows the calculation to be performed. However, constraints need to be placed on the maximum value of this constant to avoid best-fit solutions that predict sizable amounts of activity at times when it is known that there was low activity. Here it is assumed that the background total activity rate over a 30 km x 40 km area is no more than 0.25 earthquakes per year. If the activity rate, λ, has units of events per m^2 per year, then this implies that $\delta \leq 2.083 * 10^{-10}$. The total activity and activity rate equations of Table 2 become altered to those presented in Table 3, and these are used to perform the MLE.

Table 3: Modified forms for the local event rate, λ, used for the specified model forms

	λ
Linear	$\alpha\dot{c} + \delta$
Quadratic	$2\beta c\dot{c} + \alpha\dot{c} + \delta$
Cubic	$3\gamma c^2\dot{c} + 2\beta c\dot{c} + \alpha\dot{c} + \delta$
Exponential	$\alpha e^{\beta c}\dot{c}\,(1 + c\beta) + \delta$

From the equations in Table 3 it is possible to numerically evaluate the log-likelihood function for any set of parameters $\alpha, \beta, \gamma,$ and δ. There are many routines that find the minimum of functions so the coefficients that maximize the log-likelihood are solved for by finding the minimum of the negative of the log-likelihood.

While the above equations are shown using compaction, c, the exact same formulation can also be performed using the geomechanical fault moment or fault energy. Compaction is a change in volume per unit area and the maps of geomechanical model moment release are a change in moment per unit area so ***m*** can be directly substituted into the above equations for ***c*** without altering the process.

2.3.2 Generic Poisson Process Methodology

As an alternative to specifying a limited set of forms for the activity rate (as described in the previous section), a generic model form for the activity rate can be evaluated. The generalized linear model for a Poisson process is the following equation

$$\lambda = \exp(\alpha_0 + \alpha_1 f_1(\boldsymbol{c}) + \alpha_2 f_2(\boldsymbol{c}) + \alpha_3 f_3(\boldsymbol{c}) + \cdots + \alpha_k f_k(\boldsymbol{c}))$$

where the α parameters are fitting coefficients and the functions, f, can take on a range of forms (The addition of a term always improves the model fit (increases l), but the AIC penalizes the additional model complexity to avoid over-fitting. The model with the smallest AIC is the one that should have the best predictive accuracy.

Table 4 summarizes the forms that are examined here). In the generic model terms are iteratively added to the model to improve the fit until the addition of new terms is no longer warranted. The metric used to determine if the addition of a new term is warranted is the Akaike Information Criterion (AIC). The AIC value is calculated based on the log-likelihood value, l, and the number of parameters, k, that were solved for in the estimation.

$$AIC = 2k - 2l$$

The addition of a term always improves the model fit (increases l), but the AIC penalizes the additional model complexity to avoid over-fitting. The model with the smallest AIC is the one that should have the best predictive accuracy.

Table 4: Terms that can be incorporated into the generic Poisson process model

Term	Form
f_1	c
f_2	c^2
f_3	c^3
f_4	$\dot{c}$
f_5	$\dot{c}^2$
f_6	$\dot{c}^3$
f_7	$c\dot{c}$
f_8	$c^2\dot{c}$
f_9	$c\dot{c}^2$
f_{10}	$c^2\dot{c}^2$

The null hypothesis is that the data can be explained with a single term in the exponential, α_0. Similar to the methodology presented in section 2.3.1, an assumption is made regarding the maximum value for the coefficient α_0. It is assumed that the background total activity rate over a 30 km x 40 km area is no more than 0.25 earthquakes per year. If activity rate, λ, has units of events per m^2 per year, then $\alpha_0 \leq -22.292$.

Terms are added using forward stepwise refinement. To add a second parameter the MLE is performed for each potential two parameter set (α_0 and each model each term, $\alpha_1 f_1$ through $\alpha_k f_k$). The AIC is then evaluated for the two parameter fit and compared to the AIC for the one parameter fit. If the AIC decreases, then the improvement in the goodness of fit is statistically large enough to warrant the addition of a second fitting parameter. The term that decreases the AIC the most is added to the model and a new search over the remaining model terms is performed. This process is then repeated to find additional terms that should be added until the AIC value does not decrease. In general adding the term that provides the maximum reduction in AIC is a good approach, however, on occasion (especially with the fits to the

fault moment) this was found to result in the selection of a local maximum in the log-likelihood (and hence AIC) value. To address this rare situation, after some trial and error, the initial term or two to be added to the model were specified a priori.

2.4 Comparison of Activity Models

The two methodologies described in section 2.3 result in different forms for the activity rate. One way to determine which model is the best is to compare the AIC values for all of the models. However, it is necessary that the MLE be performed on the same model input domain when comparing AIC or log-likelihood values. The domain is an important consideration when comparing models based on the compaction data to models based on the fault slip data because the fault slip model data only exists within the boundaries of the three submodels while the compaction model data exists across the entire field. The MLE should be performed only using earthquakes that occurred within the submodel domain and the integral of the activity rate should only be performed over the area of the submodels as well. If the domain is the same amongst models the log-likelihood or AIC values can be compared for an assessment of which model is the best.

The choice of domain will affect the results of the MLE. Different compaction based activity models will be determined if the domain of the entire field is used versus the domain of the submodels. Results for both domains will be presented in section 3.1.

Though the AIC is designed to estimate predictive accuracy, it is also possible to directly assess predictive accuracy. This can be achieved by performing the MLE over a specified time span (e.g. April 1, 1995 – Jan 1, 2006), obtaining the best fit parameters, and using these parameters to evaluate the log-likelihood for all future years of seismicity (2006, 2007, …, 2016). The most predictive model will have the highest log-likelihood value in each of the following years. For simplicity, the log-likelihood can be summed over all of the future years so that a single parameter can be compared between models. After this, the MLE is performed over a longer time span (e.g. April 1, 1995 – Jan 1, 2007) and the parameters are used to evaluate and sum the log-likelihood values for all future years. The most predictive model should consistently have one of the highest log-likelihood summation values regardless of the timespan used to fit the model.

The summation of the log-likelihood over all future years is a good comparison between models, but the model performance in forecasting the 2015 and 2016 seismicity is of particular interest. Since the recent reductions in the annual production cap there has been a decrease in the seismicity in the field. A good activity model should be able to forecast both increases and decreases in seismicity so a high log-likelihood value in 2015 and 2016 is indicative of a good activity model. The decreased activity can provide a good constraint on some of the models and greatly improve their predictive power over the last year but some models may be less capable of representing the decrease in seismicity.

3.0 Results

3.1 Compaction Based Activity Models

To determine the best compaction based activity model both methodologies discussed in section 2.3 were examined (generic as well as the specified Poisson process). Additionally, different references (years 1988-1995 and compaction values 0-0.24 m) were examined for each methodology. Models fit based on data in two model domains were also considered. The models fit to the field domain will be discussed in detail to illustrate the results of the analysis and since they can be used to generate complete hazard maps. The models fit to the submodel domain will be discussed in less detail.

3.1.1 Fit to field domain

Table 5 summarizes the log-likelihood and AIC values for each of the fits and forms of activity model fit to the domain of the field. Larger log-likelihood values (less negative) indicate better fits and smaller AIC values indicate better estimated predictive accuracy for the number of parameters used to fit the model. The best fits for each of the methodologies (specific vs. generic), for each type of reference (year vs. value), and for both AIC and log-likelihood criterions are indicated with red text. If the AIC and log-likelihood values are in agreement, this means that there will be four “best-fit” models that are compared to one another. Sometimes the AIC values and the log-likelihood values suggest that different references are the best fit or that a different specified form is the best fit. If there is disagreement, the better AIC value is generally chosen as the better model but sometimes the model with the better log-likelihood value is still discussed for comparison.

Table 5: Log-likelihood and AIC values for models fit to the compaction data over the whole field domain. Larger log-likelihood values (less negative) and smaller AIC values indicate better fits for the number of parameters used to fit the model. The best fits for each of the methodologies, for each type of reference, and for both AIC and log-likelihood criterions are indicated with red text. The first four fits (linear – exponential) are described in section 2.3.1. The final column is the best fit generic model described in section 2.3.2. Model fits and parameter values for the reference years and values in red are presented in Table 6 and Figure 11-Figure 17.

	Log-likelihood					AIC				
Ref.	Linear	Quadratic	Cubic	Exp.	Generic	Linear	Quadratic	Cubic	Exp.	Generic
1988	-5004.10	-4949.80	-4942.93	-4943.93	-4939.80	10012.19	9905.60	9893.86	9893.85	9889.61
1989	-5004.10	-4948.83	-4942.80	-4943.70	-4939.89	10012.19	9903.66	9893.60	9893.39	9889.79
1990	-5004.10	-4947.41	-4941.73	-4942.37	**-4938.36**	10012.19	9900.83	9891.47	9890.75	**9888.72**
1991	-5004.10	-4946.25	**-4941.62**	-4942.06	-4938.64	10012.19	9898.51	9891.24	**9890.11**	9889.28
1992	-5004.10	-4947.33	-4943.91	-4944.32	-4942.76	10012.19	9900.66	9895.82	9894.65	9895.52
1993	-5004.10	-4948.62	-4945.49	-4945.83	-4945.07	10012.19	9903.25	9898.97	9897.66	9900.14
1994	-5004.10	-4948.93	-4946.77	-4947.11	-4946.93	10012.19	9903.86	9901.55	9900.21	9903.86
1995	-5004.44	-4949.32	-4947.34	-4947.46	-4947.76	10012.88	9904.63	9902.68	9900.92	9905.52
0.0 m	-5266.56	-5011.10		-4969.61	-4948.68	10537.12	10028.20		9945.22	**9907.36**
0.01 m	-5254.51	-5019.17	-4964.67	-4969.31	**-4947.87**	10513.02	10044.34	9937.35	9944.62	9907.73
0.02 m	-5241.70	-5026.00	-4963.79	-4968.98	-4948.15	10487.39	10058.01	9935.57	9943.95	9908.31
0.04 m	-5214.93	-5030.54	-4962.90	-4968.25	-4949.39	10433.85	10067.08	9933.79	9942.50	9908.79
0.06 m	-5189.09	-4986.19	-4962.99	-4967.45	-4949.86	10382.18	9978.39	9933.99	9940.91	9909.72
0.08 m	-5156.20	-4997.91	-4962.33	-4965.97	-4950.29	10316.41	10001.82	9932.67	9937.93	9912.58
0.09 m	-5141.31	-4990.31	-4961.88	-4965.51	-4953.94	10286.62	9986.62	9931.76	9937.01	9915.89
0.10 m	-5125.18	-4978.62	-4961.58	-4965.04	-4953.16	10254.35	9963.24	9931.16	9936.08	9916.32
0.11 m	-5107.30	-4980.89	-4961.09	-4964.01	-4954.94	10218.61	9967.78	9930.19	9934.01	9919.89
0.12 m	-5089.00	-4976.44	**-4960.89**	-4963.42	-4954.13	10181.99	9958.89	**9929.78**	9932.84	9920.26
0.13 m	-5072.71	-4974.27	-4961.25	-4963.46	-4956.37	10149.43	9954.54	9930.51	9932.91	9922.73
0.14 m	-5056.18	-4972.94	-4962.90	-4964.60	-4958.11	10116.36	9951.88	9933.81	9935.21	9928.21
0.15 m	-5044.72	-4971.54	-4965.62	-4967.05	-4963.38	10093.43	9949.08	9939.24	9940.09	9936.75
0.16 m	-5032.11	-4971.63	-4967.14	-4968.08	-4966.15	10068.23	9949.27	9942.28	9942.16	9942.30
0.18 m	-5021.24	-4980.11	-4977.14	-4977.70	-4979.55	10046.49	9966.22	9962.28	9961.41	9971.10
0.20 m	-5020.62	-4993.22	-4990.67	-4991.38	-4994.60	10045.25	9992.43	9989.33	9988.75	10003.20
0.22 m	-5069.35	-5047.11	-5046.94	-5047.44	-5051.33	10142.70	10100.22	10101.89	10100.89	10114.67
0.24 m	-5122.10	-5114.21	-5113.77	-5114.01	-5125.01	10248.19	10234.416	10235.547	10234.023	10264.02

According to Table 5, a compaction reference of 0.0m provides the best AIC for generic models, whereas a compaction reference of 0.12m and a cubic form is best among the specified models. In the case of a reference year, 1990 is the best fit for the generic model and 1991 is the best fit for the specified model. Since the preference for one year vs. another is so small, here we choose to only examine 1990, because as will be discussed later, 1990 is also a good year for fits made to just the submodel domain. Additionally, the exponential fit referenced to the year 1990 is the fit that is often used by Shell/NAM to produce hazard maps. The log-likelihood value indicates that the cubic is the best model fit while the AIC value indicates that the exponential is the best model fit. Both scenarios are presented and discussed here so that the effect of the subtle differences in the activity maps can be illustrated. The reference year and reference values that are some of the best fits are also highlighted in red in column 1 of Table 5. The parameters for these best fit models (as well as the other specific model fits that are made for the best fit reference

values) are presented in Table 6 and the terms of the generic model are presented in order of their addition to the AIC resulting solution.

Table 6: Best fit parameters used to generate the models presented in Table 5. All fits were performed using the compaction data and the earthquake catalog within the outline of the field. Terms of the generic model are presented in order of their addition to the solution.

Reference	Linear	Quadratic	Cubic	Exponential	Generic
1990	$\alpha = 3.482\ e\text{-}6$ $\delta = 4.155\ e\text{-}11$	$\beta = 6.644\ e\text{-}5$ $\alpha = -6.202\ e\text{-}7$ $\delta = 7.118\ e\text{-}11$	$\gamma = 7.124\ e\text{-}4$ $\beta = -8.105\ e\text{-}6$ $\alpha = 7.010\ e\text{-}7$ $\delta = 5.140\ e\text{-}11$	$\alpha = 5.128\ e\text{-}7$ $\beta = 16.294$ $\delta = 4.967\ e\text{-}11$	$\alpha_0 = -22.72$ $\alpha_1 = 7.026\ e1$ $\alpha_2 = -4.193\ e2$ $\alpha_4 = 4.227\ e2$ $\alpha_6 = -2.682\ e6$ $\alpha_3 = 9.998\ e2$
0.00 m					$\alpha_0 = -23.06$ $\alpha_1 = 2.367\ e1$ $\alpha_3 = -9.018\ e1$ $\alpha_8 = 4.767\ e3$ $\alpha_5 = -2.655\ e4$
0.12 m	$\alpha = 2.599\ e\text{-}6$ $\delta = 2.083\ e\text{-}10$	$\beta = 3.298\ e\text{-}5$ $\alpha = -1.845\ e\text{-}7$ $\delta = 2.083\ e\text{-}10$	$\gamma = 2.596\ e\text{-}4$ $\beta = -3.167\ e\text{-}6$ $\alpha = 1.660\ e\text{-}7$ $\delta = 2.083\ e\text{-}10$	$\alpha = 2.552\ e\text{-}7$ $\beta = 12.82$ $\delta = 2.083\ e\text{-}10$	

A comparison of the four best AIC values (red text in Table 5) indicates which model is estimated to have the best predictive accuracy. The generic model referenced to a year is the best, followed closely by the exponential specific model referenced to a year (or the cubic specific model referenced to a year if log-likelihood is considered), then the generic model referenced to a value and then the cubic specific model referenced to a value. Based on the AIC and log-likelihood values, the models referenced to a year are substantially better fits to the observed earthquake data than the models that are referenced to values.

Behind each of the log-likelihood/AIC values presented in Table 5 there is a model specified by a set of parameters that characterizes the historical activity and can be used to forecast the future seismicity. Every fit is different and the best fit scenarios are presented in Figure 11-Figure 17 for a 27 bcm production scenario. Figure 11 and Figure 12 illustrate the sum of the total activity over the entire field domain. The black circles are the number of earthquakes per year within the field boundary and the colored lines are different model fits. All models that are referenced to a year are shown in Figure 11 while all models that are referenced to a compaction value are shown in Figure 12. Figure 13-Figure 17 show the spatial distribution of activity for the five models considered.

All of the specified Poisson process models referenced to a year appear in Figure 11a while all of the generic Poisson process models referenced to a year appear in Figure 11c. To illustrate how the fit changes as parameters are added to the generic model, multiple fits from the iterative process are included. “fit 1” is the fit using just the α_0 parameter while “fit 2” is the fit using α_0 and the next best term (listed in order in Table 6) and so on. The final fit is the best generic model fit using all of the parameters included in Table 6. The specified and generic models from the best fit reference year, 1990, are shown in Figure 11b and d respectively. Of the specified Poisson process models, the cubic fit has the best log-likelihood value but the exponential model has the best AIC value. The best generic model is “fit 6” in Figure 11d. These are three of the 5 models considered going forward.

All models that are referenced to a compaction value are shown in Figure 12. All the Specified Poisson process models appear in Figure 12a while all the generic Poisson process models appear in Figure 12c. The models from the best fit reference values, 0.12m for the specified models or 0.0m for the generic models are shown in Figure 11b and d.

A visual examination of the best fit models in Figure 11 does not reveal large differences in the fit to the observed earthquakes. This is a qualitative assessment that is backed up by the quantitative assessment that is captured by the log-likelihoods. The log-likelihood values for the best fit models to reference years are very close ($\Delta < 1$). A visual examination of the best fit models in Figure 12 shows an over prediction of the number of earthquakes predicted in the early 80's, a time when few to no earthquakes are likely to have occurred. The lower quality of fit is reflected in the log-likelihood values ($\Delta = 10 - 20$). This large difference and the visual examination of the activity level lead to a conclusion that models that are referenced to a year are much more consistent with observed seismicity to date than models that are referenced to a compaction value.

While the three best models referenced to a year all have a similarly good representation of the historical activity level, there are some significant differences in their activity level projections for future years. The exponential model forecasts a higher activity level than the cubic or the generic model. Additionally, the generic model projects a nearly constant future activity rate while the cubic and exponential forecast activity rates rise and fall over time.

Another way to examine the historical and future fits is via maps of activity for different years. Figure 13-Figure 17 show the activity maps for 1996-2020 for the five best model fits. A careful comparison of these figures shows that the models result in different degrees of spatial localization of the activity. The generic model, referenced to 1990 results in the most diffuse activity forecast while the generic model referenced to a value of 0 m is the most localized. As discussed in section 4, the spatial distribution of forecast activity will affect resulting hazard maps.

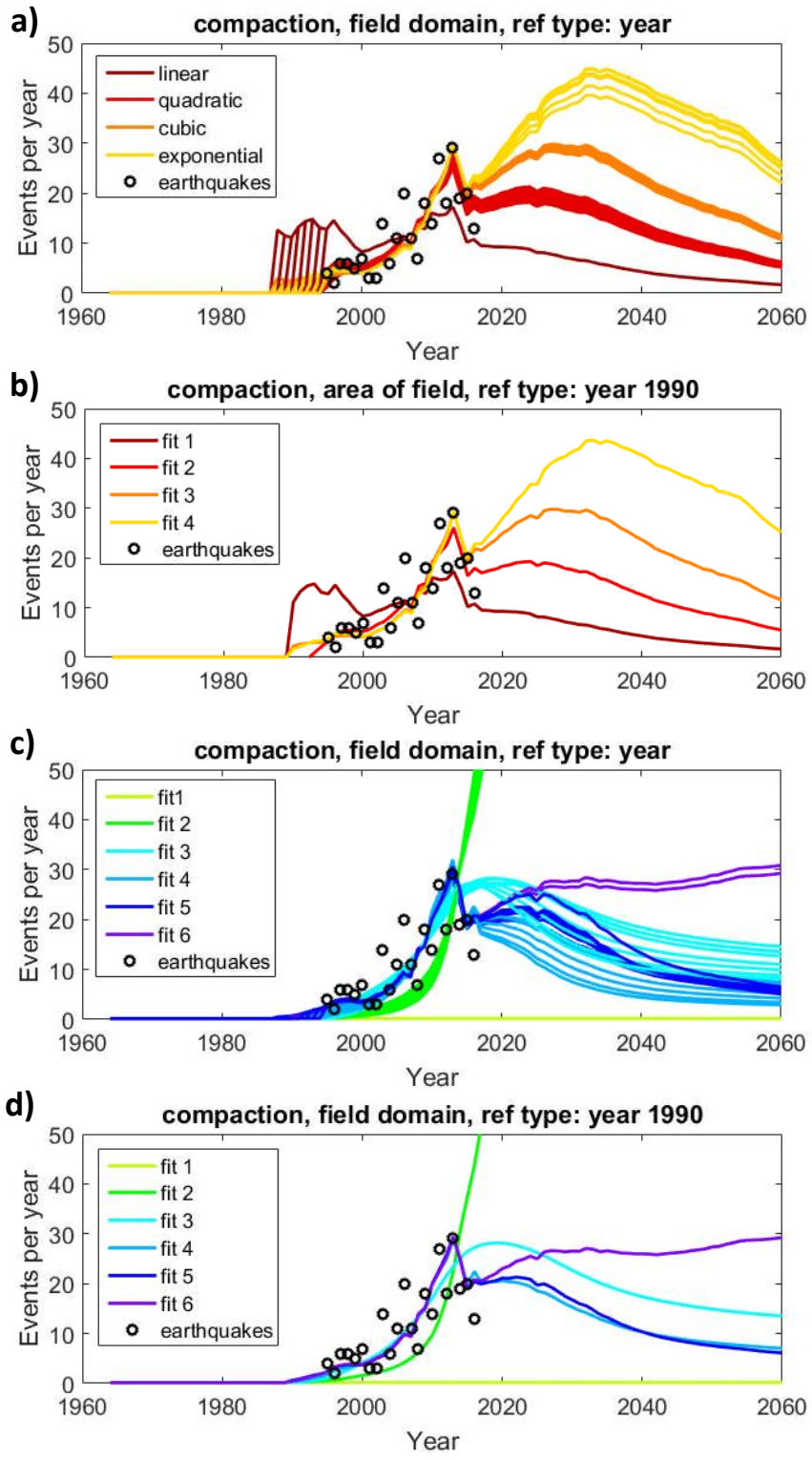

Figure 11: Compaction based fits made on the field domain and referenced to a year. (a) All specified Poisson process model fits to all reference years examined. (b) Specified Poisson process model fits to the best year, 1990. Cubic is the log-likelihood (map shown in Figure 14) and exponential is the best AIC (map shown in Figure 13). (c) All generic Poisson process model fits to all reference years examined - progression of fit with the addition of parameters is shown. (d) Generic Poisson process model fit to the best year, 1990. Fit 6 is the best fit and is used for the maps shown in Figure 15.

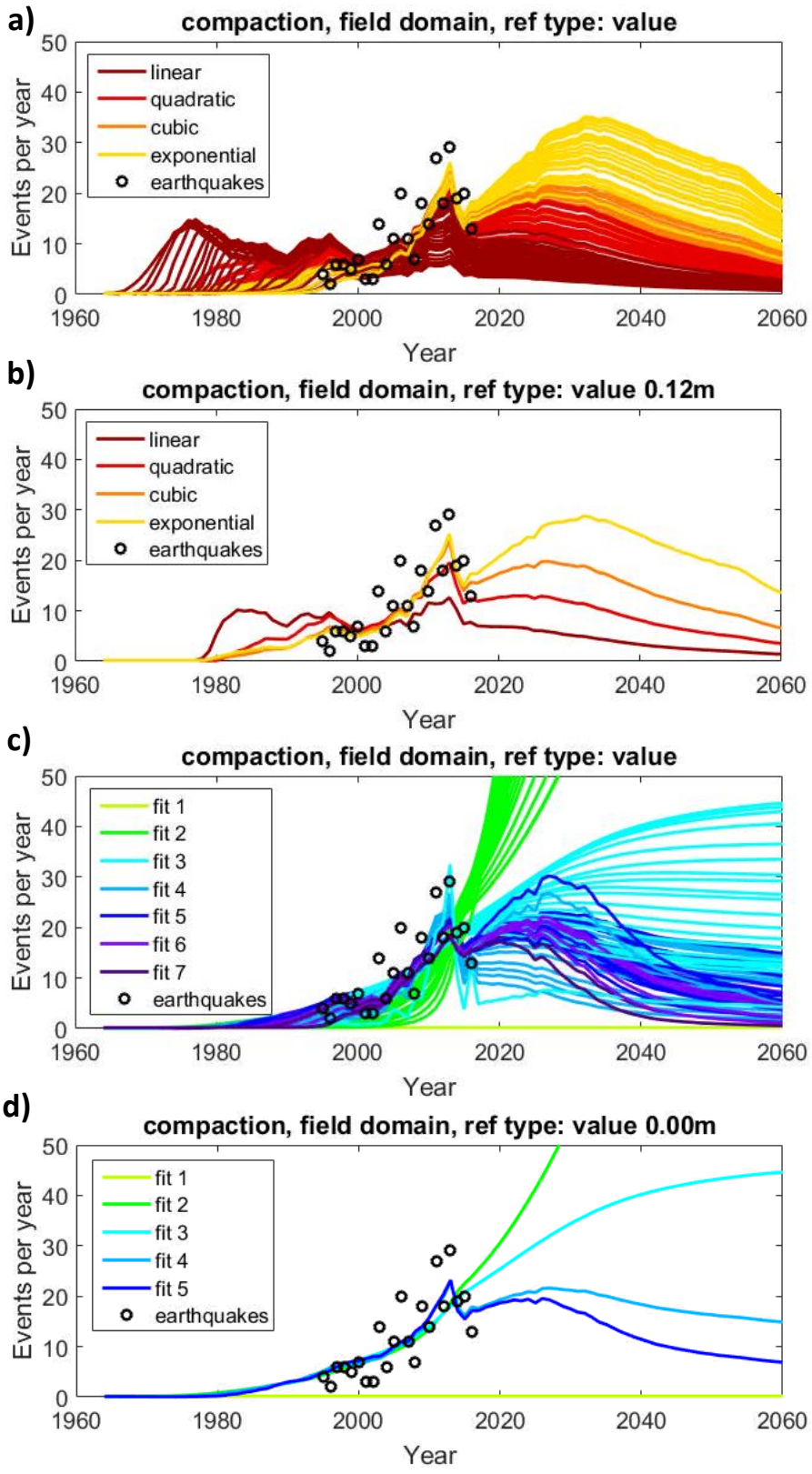

Figure 12: Similar to Figure 11. Fits to compaction data, in the field domain, referenced to specific values. Best fits are highlighted in (b) and (d) with corresponding maps of activity shown in Figure 16 (cubic) and Figure 17 (fit 5) respectively.

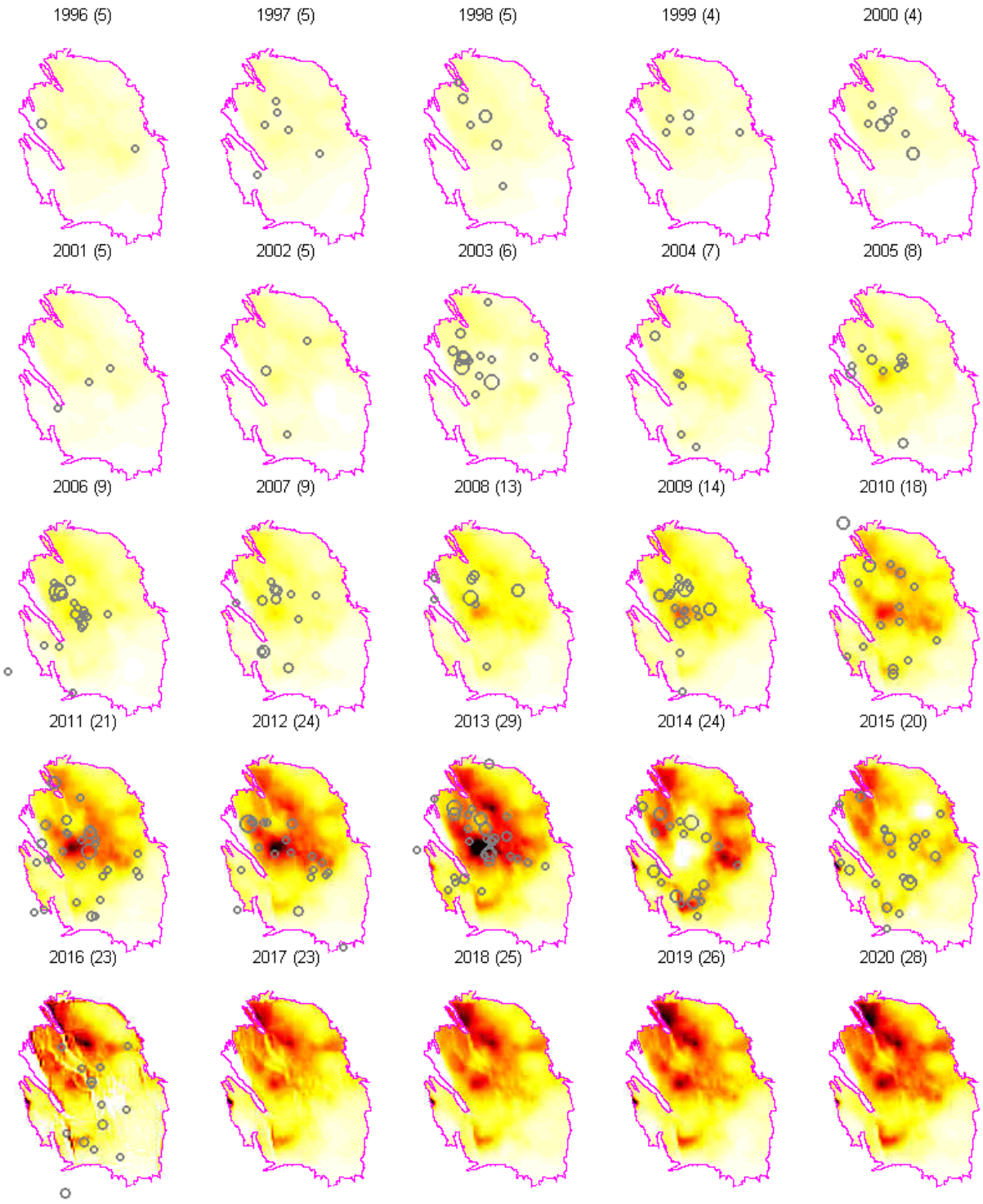

Figure 13: Maps of activity based on compaction data, fit to the field domain data, for the exponential model, referenced to the year 1990, using a 27 bcm scenario for future projections. This is the model often used by Shell/NAM for the production of hazard maps. Actual activity is presented for a range of years. The number in parenthesis in the sub-figure title is the forecasted number of events in that year. Activity color bar ranges from 0-1e^{-7} events per m^2 per year

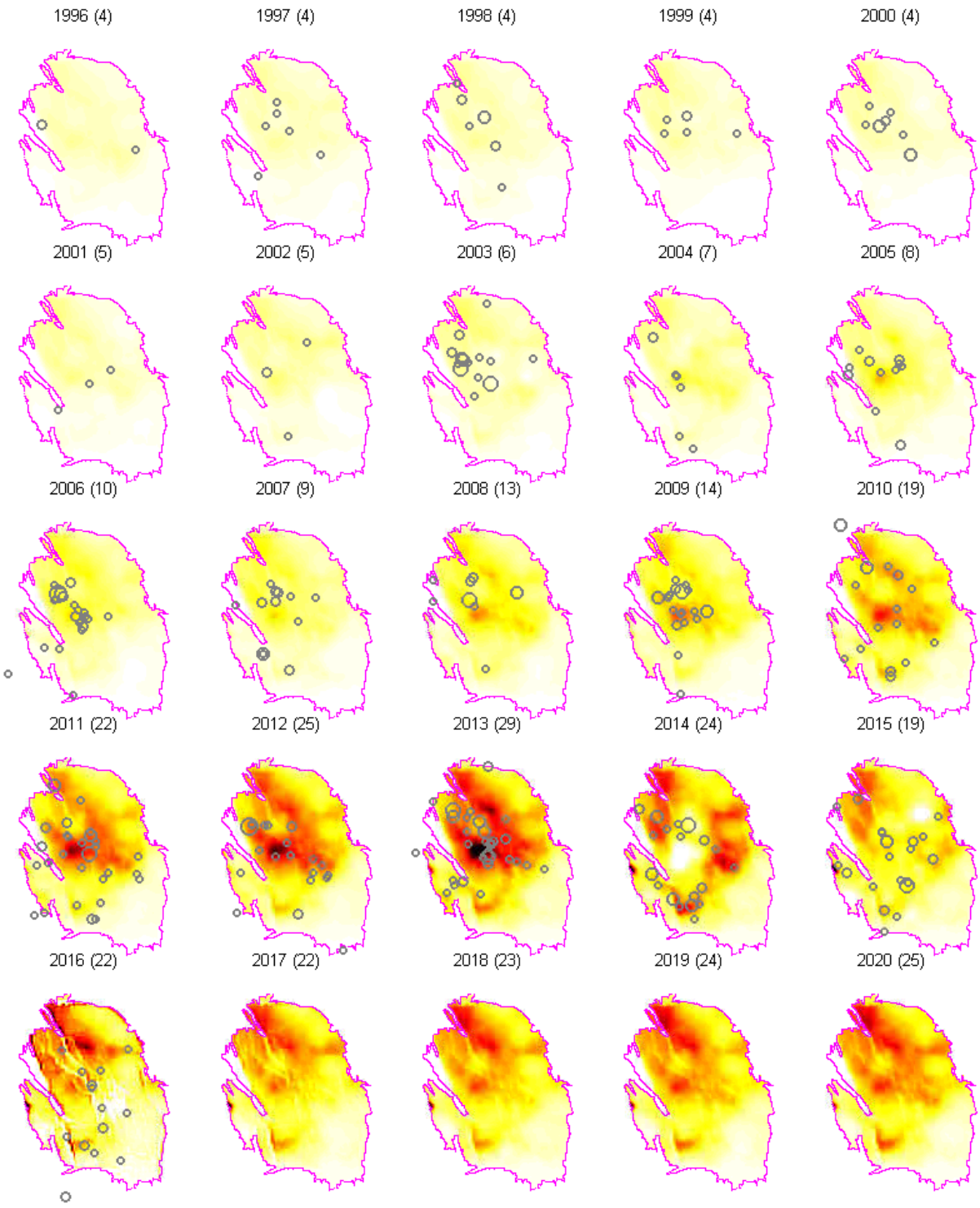

Figure 14: Maps of activity based on compaction data, fit to the field domain data, for the cubic fit, referenced to the year 1990, using a 27 bcm scenario for future projections. Actual activity is presented for a range of years. The number in parenthesis in the sub-figure title is the forecasted number of events in that year. Activity color bar ranges from 0-1e^{-7} events per m^2 per year

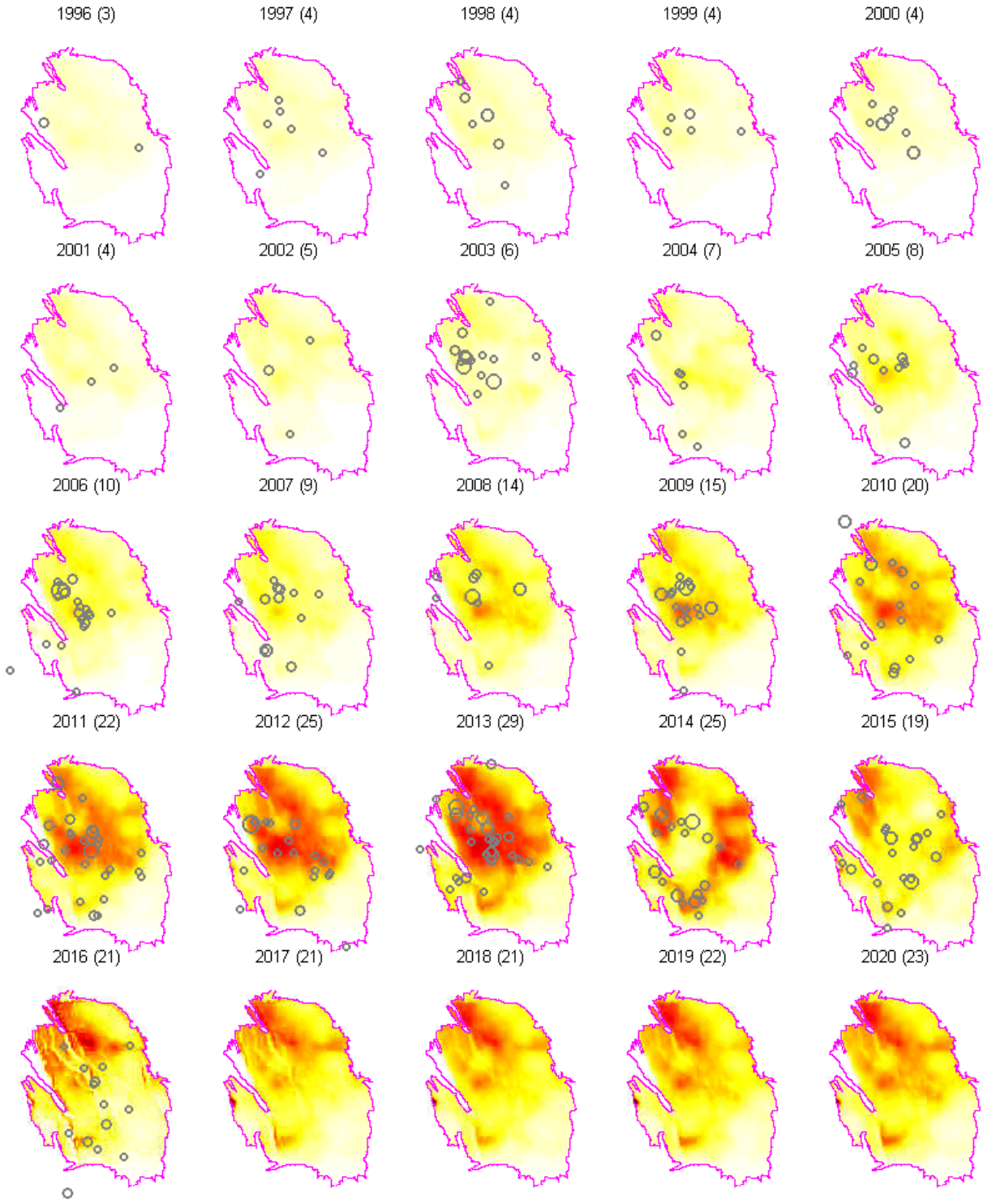

Figure 15: Maps of activity based on compaction data, fit to the field domain data, for the best generic Poisson process model, referenced to the year 1990, using a 27 bcm scenario for future projections. Actual activity is presented for a range of years. The number in parenthesis in the sub-figure title is the forecasted number of events in that year. Activity color bar ranges from 0-1e^{-7} events per m^2 per year

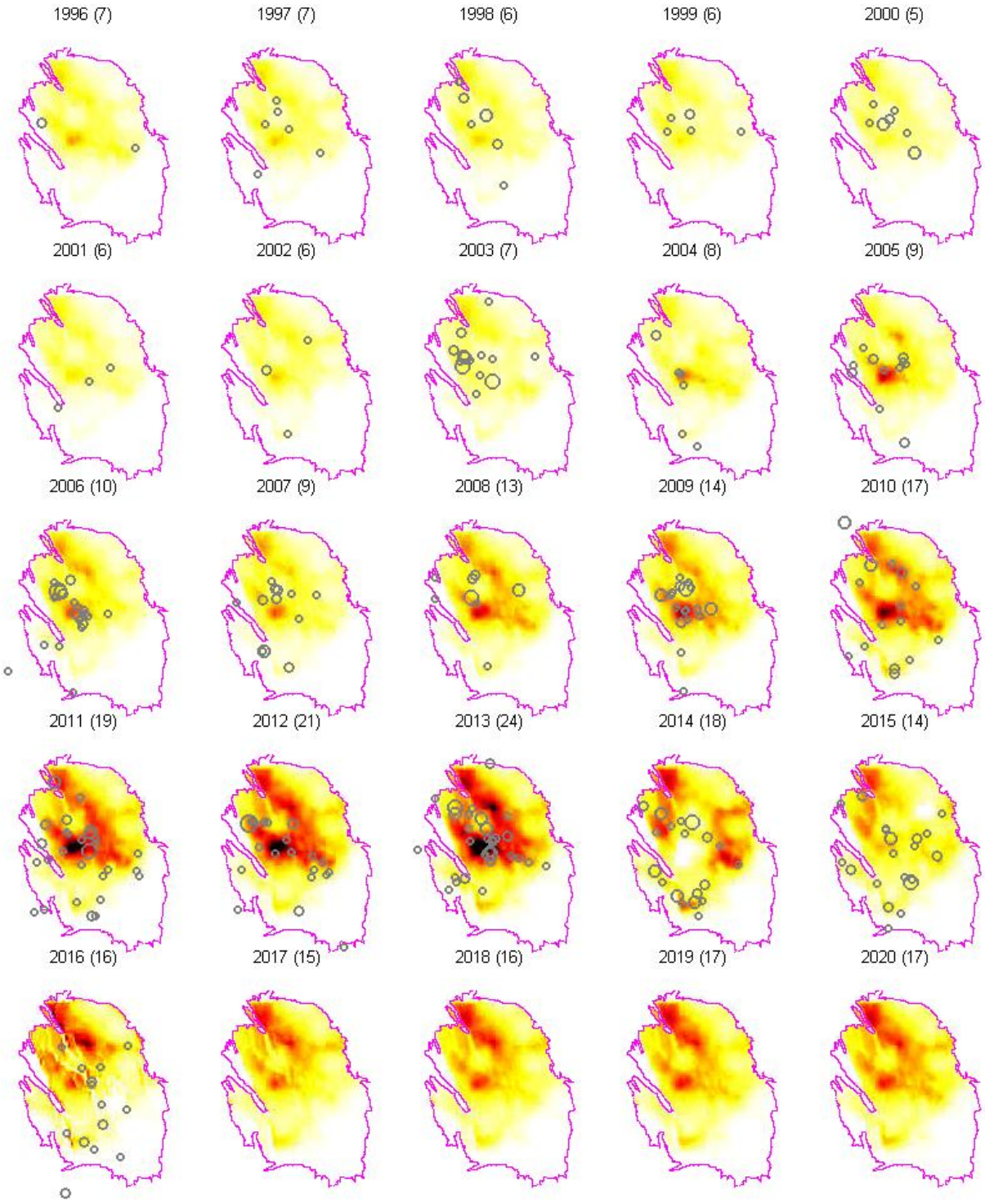

Figure 16: Maps of activity based on compaction data, fit to the field domain data, for the cubic fit, referenced to a compaction value of 0.12m, using a 27 bcm scenario for future projections. Actual activity is presented for a range of years. The number in parenthesis in the sub-figure title is the forecasted number of events in that year. Activity color bar ranges from 0-1e^{-7} events per m^2 per year

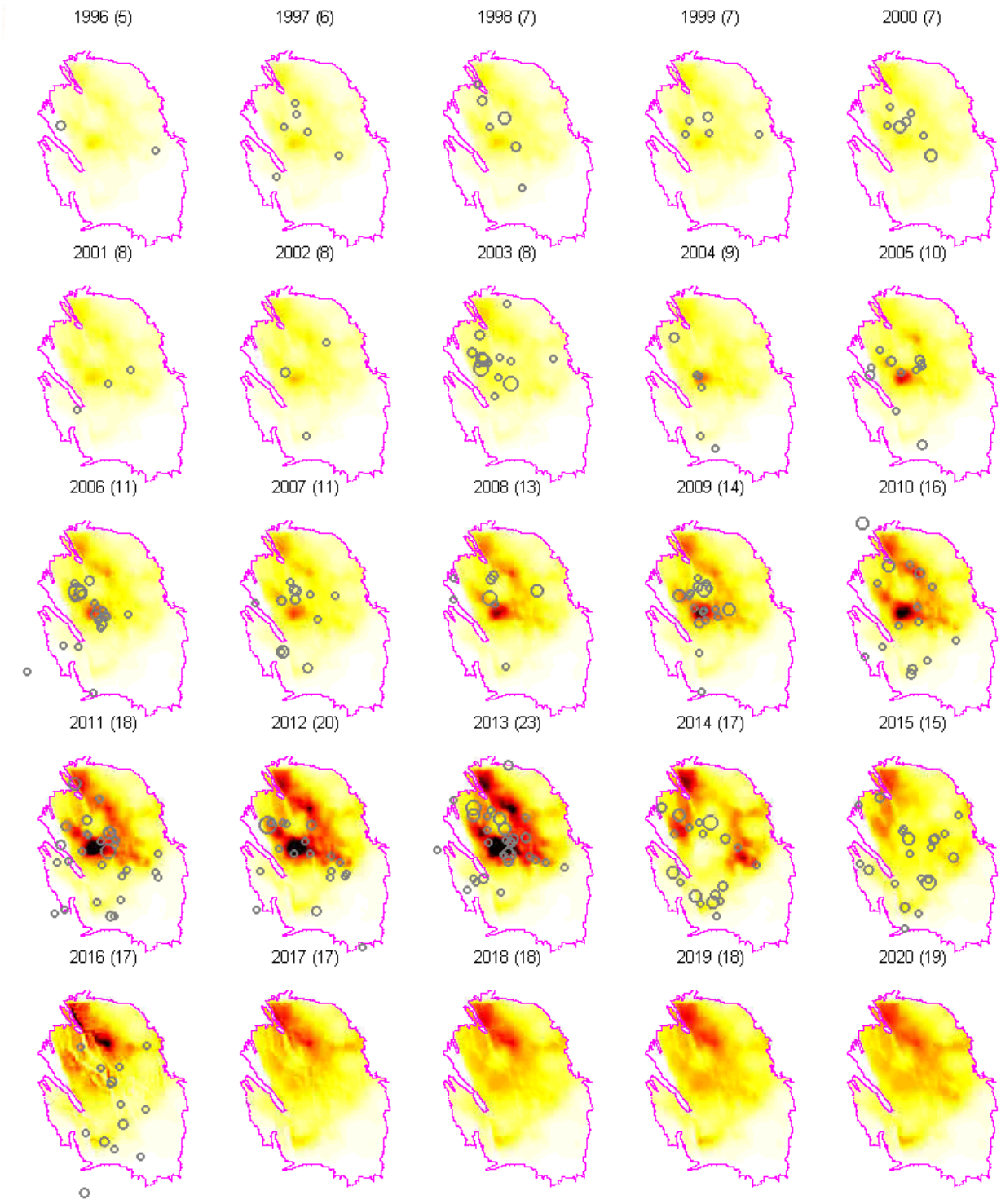

Figure 17: Maps of activity based on compaction data, fit to the field domain data, for the best generic Poisson process model, referenced to a compaction value of 0.0m, using a 27 bcm scenario for future projections. Actual activity is presented for a range of years. The number in parenthesis in the sub-figure title is the forecasted number of events in that year. Activity color bar ranges from 0-1e^{-7} events per m^2 per year

To directly assess predictive power, each model is fit to a subset of the data and the sum of the log-likelihood values for all future years is examined. As with all log-likelihood values, larger values (less negative) indicate a better fit. Figure 18 shows these values for the models highlighted above, referenced to the year 1990. A value plotted in the year 2010 is the sum of the log-likelihood for years 2010-2016. Many of the lines plot on top of one another so the same data is presented in Figure 19, but flattened so that the second worst model fit is on the x axis. This allows for the distinction between the lines to be more clearly visible.

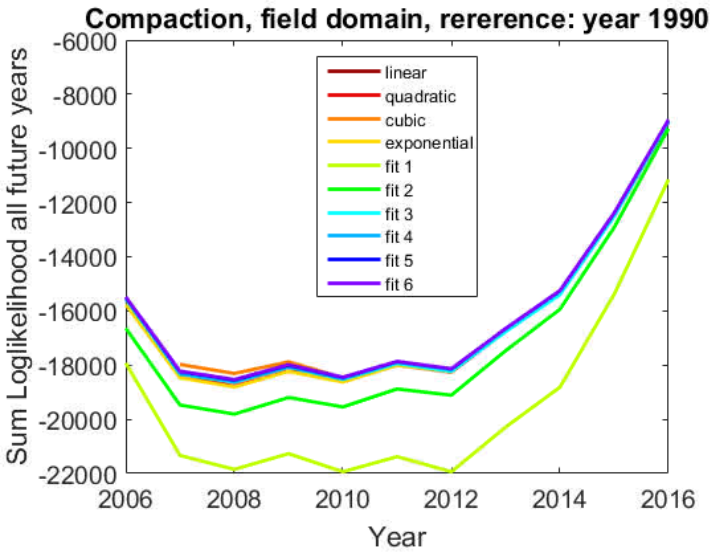

Figure 18: Sum of the log-likelihood for all future years of observation for each of the best fitting models that are referenced to 1990. Data points in year 2013 are for a model that is fit to data spanning from April 1, 1995 to January 1, 2013. Model parameters are then used to evaluate the log-likelihood for the years 2013 – 2016 and then these four numbers are summed.

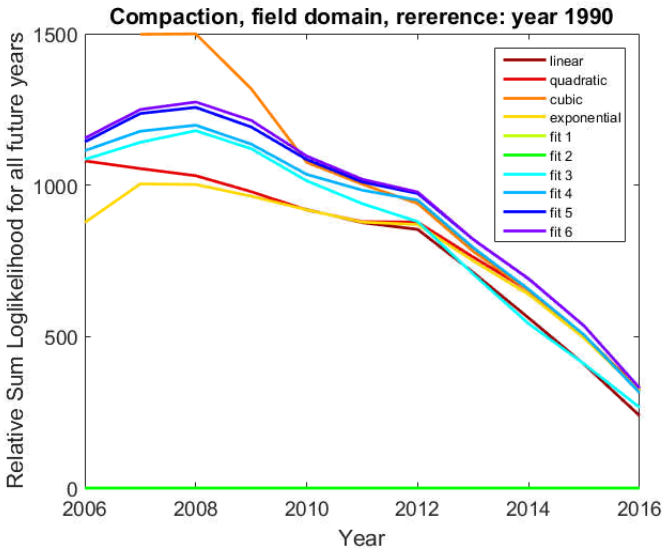

Figure 19: Same as Figure 18 but flattened to the second lowest log-likelihood line so that differences between the models are more clearly visible.

Starting with data that is fit to a time frame that ends January 1, 2009, the generic Poisson process model, fit 6, is the most predictive model. When earthquake observation data post January 1, 2014 is added to the model fitting, the specified model forms begin to catch up to the generic model forms. This means that the decrease in activity is having a larger effect on the specified model forms and increasing their predictive power more than the generic model forms. For the time being, "fit 6" is still a consistently better performing model than either the cubic or the exponential, but this may change over the next year or two if low seismic activity rates continue.

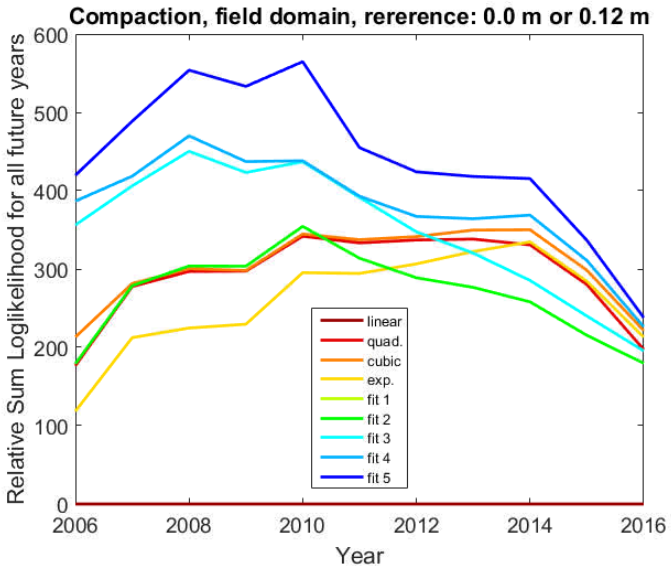

Figure 20: Same as Figure 19 but for reference to a value rather than a year.

Figure 18-Figure 19 are for the models that are referenced to a year, which are much better models than those that are referenced to values. However, for completeness the predictive power of the models referenced to values are also presented in Figure 20. The generic model is more predictive than the specific models, and while the gap is narrowing, the specific models are not yet close to overtaking the generic model.

Many model fits are performed over varying time windows when generating the data needed to directly assess the predictive power of the models. Figure 21 and Figure 22 show all of the different models and their projections into the future for models referenced to a year and to a value respectively. The variation in the model projections over time is an indication of how much the activity forecast changes with the addition of additional years of data (note that only fits up to Jan 1, 2016 are included so the most up-to-date model is not included in the figures). Some models are poorly constrained in the beginning and forecast negative activity rates (e.g. the cubic model as of a few years ago when referenced to a year). In general, the models that are referenced to a value (Figure 22) are more stable with the addition of new data, but these have substantially worse fits in general.

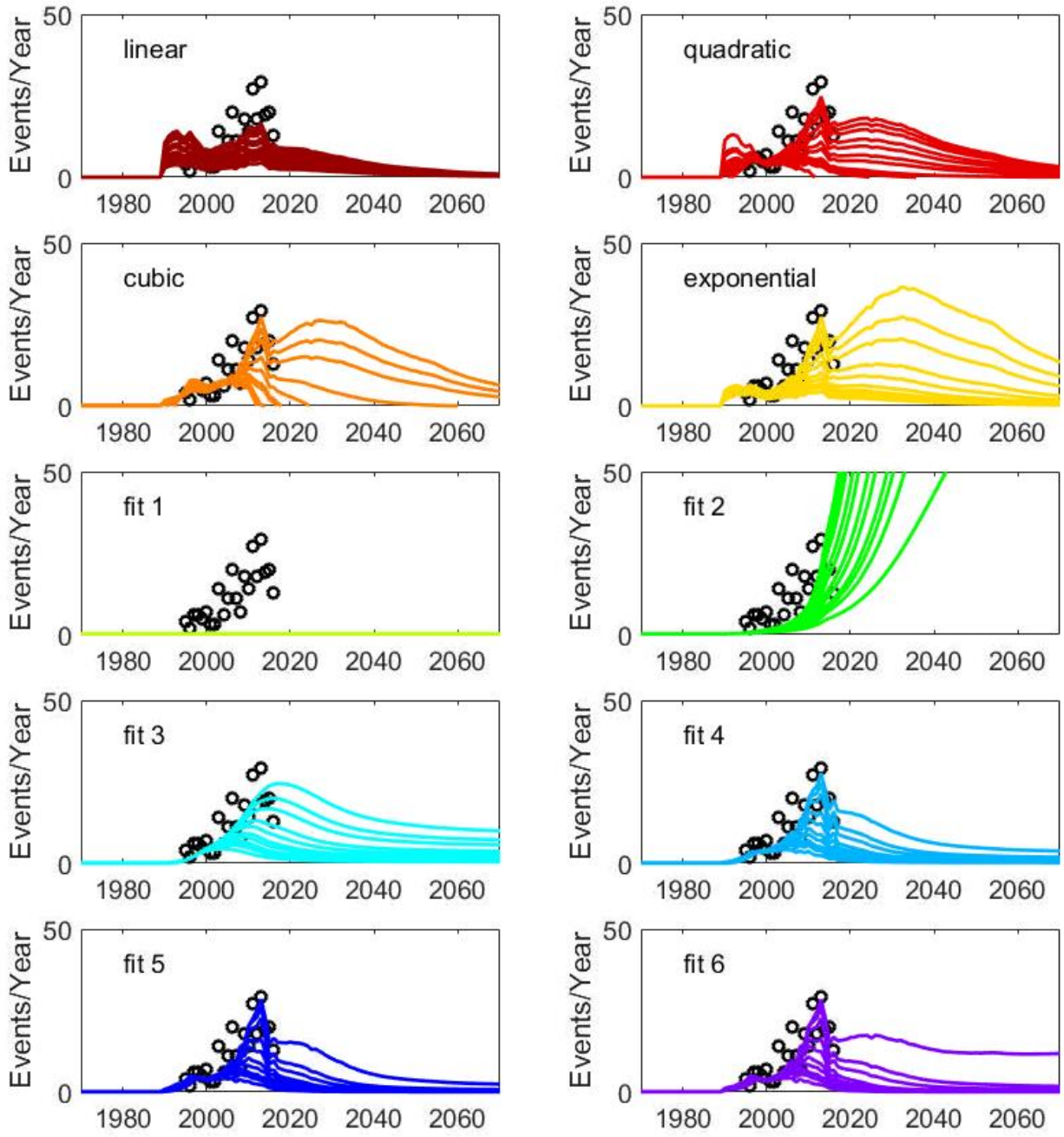

Figure 21: The collection of model fits made to the data over the timespan starting in April 1, 1995 and ending in January 1, 2006 to January 1, 2016. At early times, with little data to constrain the model, some models are poorly behaved and forecast negative activity rates post 2010.

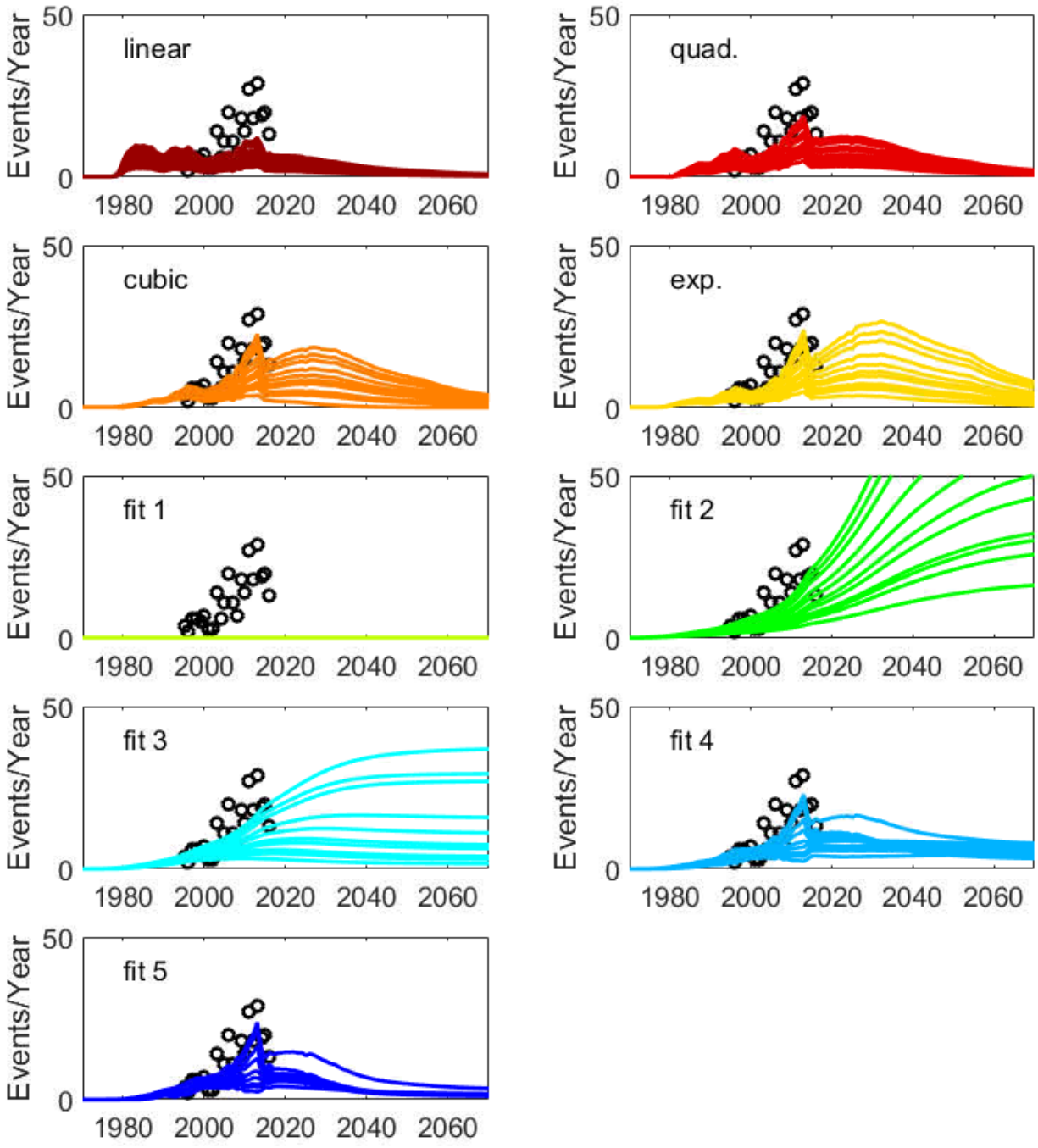

Figure 22: Same as Figure 21 but for models referenced to a value, not a year.

3.1.2 Fit to the submodel domain

For a direct comparison of compaction based and fault based models, it is necessary that the same data be used in the fitting process and the AIC evaluation. Therefore, the MLE based on the compaction data is also performed over the domain of just the submodels. The resulting AIC values and parameter fits are presented in Table 7. All AIC values in Table 7 are smaller than those in Table 5 because the size of the model domain and the number of earthquakes used to fit the model are smaller. The AIC values cannot

be compared between Table 5 and Table 7 because of the difference in domain. The parameter fits behind the best fit models of Table 7 are presented in Table 8. A comparison between the parameter values in Table 6 and Table 8 shows that there are some differences in the fit (which is expected given that they are fit to different datasets) but some of the differences are small. One of the most significant differences is that different terms are added to the generic model depending on the domain considered (f_1, f_2, f_4, f_6, f_3 used for the field domain and f_1, f_2, f_8, f_9, f_4 used for the submodel domain).

Similar to when the model was fit to the compaction and earthquake data in the domain of the entire field, the models that are referenced to years are much better fits than those that are referenced to compaction values. The best generic model, according to the AIC value, is referenced to 1988 while the best specific model is the cubic model referenced to 1990. When the log-likelihood value is considered, the best generic model is referenced to 1990 and the best specific model remains the cubic referenced to 1990. Here, for simplicity, only 1990 is examined further since this consistently shows up as a good reference year for the compaction model fits.

Table 7: Identical to Table 5 but for compaction based fits to the submodel domain. The best fits for each of the methodologies, for each type of reference, and for both AIC and log-likelihood criterions are indicated with red text. Model fits and parameter values for the reference years and values in red are presented in Table 8 and Figure 23-Figure 26.

	Log-likelihood					AIC				
Reference	Linear	Quadratic	Cubic	Exp.	Generic	Linear	Quadratic	Cubic	Exp.	Generic
1988	-4618.07	-4565.21	-4556.68	-4558.77	-4550.12	9240.14	9136.42	9121.37	9123.54	**9110.23**
1989	-4618.07	-4564.68	-4557.20	-4559.01	-4551.14	9240.14	9135.37	9122.40	9124.01	9112.28
1990	-4618.07	-4563.60	**-4556.81**	-4558.29	**-4550.00**	9240.14	9133.19	**9121.61**	9122.58	9112.00
1991	-4618.07	-4562.72	-4557.33	-4558.48	-4551.05	9240.14	9131.43	9122.67	9122.96	9114.09
1992	-4618.07	-4562.41	-4558.63	-4559.66	-4552.95	9240.14	9130.83	9125.27	9125.32	9117.90
1993	-4618.07	-4562.83	-4559.74	-4560.67	-4555.15	9240.14	9131.67	9127.47	9127.34	9122.29
1994	-4618.07	-4562.04		-4561.29	-4556.64	9240.14	9130.08		9128.58	9125.28
1995	-4618.25	-4562.45	-4561.32	-4562.26	-4558.07	9240.49	9130.90	9130.64	9130.52	9128.14
0.0 m	-4862.50	-4641.10	-4596.12	-4595.75	**-4566.79**	9729.01	9288.21	9200.23	9197.50	**9147.59**
0.01 m	-4851.04	-4647.40	-4593.76	-4595.45	-4568.62	9706.09	9300.79	9195.53	9196.89	9149.23
0.02 m	-4838.90	-4652.55	-4591.68	-4595.11	-4570.80	9681.81	9311.10	9191.35	9196.22	9151.60
0.04 m	-4815.73	-4651.82	-4588.84	-4594.57	-4571.20	9635.46	9309.64	9185.68	9195.13	9152.41
0.06 m	-4794.20	-4610.42	-4588.31	-4594.06	-4572.33	9592.40	9226.83	9184.62	9194.13	9154.66
0.08 m	-4765.24	-4619.39	-4586.98	-4592.60	-4572.64	9534.48	9244.78	9181.95	9191.20	9157.28
0.09 m	-4752.41	-4611.93	-4586.56	-4592.30	-4573.12	9508.82	9229.86	9181.13	9190.59	9158.24
0.10 m	-4737.75	-4601.02	-4586.33	-4591.95	-4576.10	9479.50	9208.05	9180.65	9189.90	9162.19
0.11 m	-4721.29	-4602.97	**-4585.89**	-4590.94	-4576.70	9446.59	9211.94	**9179.77**	9187.87	9165.41
0.12 m	-4704.35	-4599.26	-4585.96	-4590.51	-4578.62	9412.70	9204.52	9179.93	9187.02	9169.25
0.13 m	-4689.97	-4596.78	-4586.80	-4590.93	-4578.09	9383.95	9199.56	9181.60	9187.86	9168.18
0.14 m	-4675.01	-4595.37	-4588.91	-4592.45	-4580.94	9354.03	9196.74	9185.83	9190.90	9173.89
0.15 m	-4660.49	-4593.24	-4590.08	-4592.86	-4584.16	9324.99	9192.49	9188.16	9191.72	9180.33
0.16 m	-4648.35	-4593.99	-4592.13	-4594.18	-4585.81	9300.70	9193.97	9192.26	9194.36	9185.61
0.18 m	-4637.02	-4603.57	-4602.82	-4603.74	-4602.96	9278.03	9213.13	9213.63	9213.48	9217.91
0.20 m	-4635.34	-4613.89	-4613.67	-4614.07	-4617.09	9274.68	9233.78	9235.35	9234.15	9242.18
0.22 m	-4668.41	-4654.70	-4654.68	-4654.95	-4658.74	9340.82	9315.39	9317.35	9315.91	9327.48
0.24 m	-4729.88	-4725.58	-4725.28	-4725.46	-4736.89	9463.75	9457.17	9458.55	9456.93	9485.78

The model fits and forecasts over the submodel domain are shown in Figure 23 and Figure 24. The spatial map for the generic model referenced to 1990 is presented in Figure 25. A comparison of Figure 15 (field domain) and Figure 25 (submodel domain) shows much redder colors in Figure 25, and the same color scale is used. This means that there is higher activity in the submodel area when the fit is performed only in the submodel domain. This is because most of the earthquakes occur within the submodel domain, so if only that domain is considered, there must be a higher activity rate per square meter. For this reason it is not recommended to extend this fit to the entire field domain for hazard forecasts because the activity would be over-predicted. This fit should only be used for comparison to the fault slip based models.

Table 8: Best fit parameters used to generate the models presented in Table 7. All fits were performed using the compaction data and the earthquake catalog within the submodel domain.

Reference	Linear	Quadratic	Cubic	Exponential	Generic
1990	$\alpha = 4.516\ e\text{-}6$ $\delta = 5.839\ e\text{-}11$	$\beta = 8.549\ e\text{-}5$ $\alpha = -7.612\ e\text{-}7$ $\delta = 1.185\ e\text{-}10$	$\gamma = 1.048\ e\text{-}3$ $\beta = -2.435\ e\text{-}5$ $\alpha = 1.172\ e\text{-}6$ $\delta = 7.984\ e\text{-}11$	$\alpha = 6.634\ e\text{-}7$ $\beta = 1.626\ \text{e}1$ $\delta = 7.741\ e\text{-}11$	$\alpha_0 = \text{-}22.35$ $\alpha_1 = 8.709\ e1$ $\alpha_2 = -5.295\ e2$ $\alpha_8 = 2.186\ e2$ $\alpha_9 = 5.374\ e4$ $\alpha_4 = -6.323\ e5$
0.00 m					$\alpha_0 = \text{-}22.29$ $\alpha_1 = 1.910\ e1$ $\alpha_3 = -8.742\ e1$ $\alpha_8 = 8.097\ e3$ $\alpha_5 = -1.041\ e5$ $\alpha_{10} = -1.657\ e6$ $\alpha_9 = 6.527\ e5$
0.12 m	$\alpha = 3.357\ e\text{-}6$ $\delta = 2.083\ e\text{-}10$	$\beta = 4.130\ e\text{-}5$ $\alpha = -1.738\ e\text{-}7$ $\delta = 2.083\ e\text{-}10$	$\gamma = 3.100\ e\text{-}4$ $\beta = -2.330\ e\text{-}6$ $\alpha = 1.887\ e\text{-}7$ $\delta = 2.083\ e\text{-}10$	$\alpha = 3.561\ e\text{-}7$ $\beta = 12.13$ $\delta = 2.083\ e\text{-}10$	

Similar to when the model is fit over the domain of the entire field, Figure 27 indicates that the generic model was historically the most predictive model but the specific models have become relatively much more predictive over the past few years now that the annual production has been reduced and the seismic activity has decreased. It is possible that an additional year of decreased seismic activity will result in the specified models overtaking the generic model in terms of their predictive power.

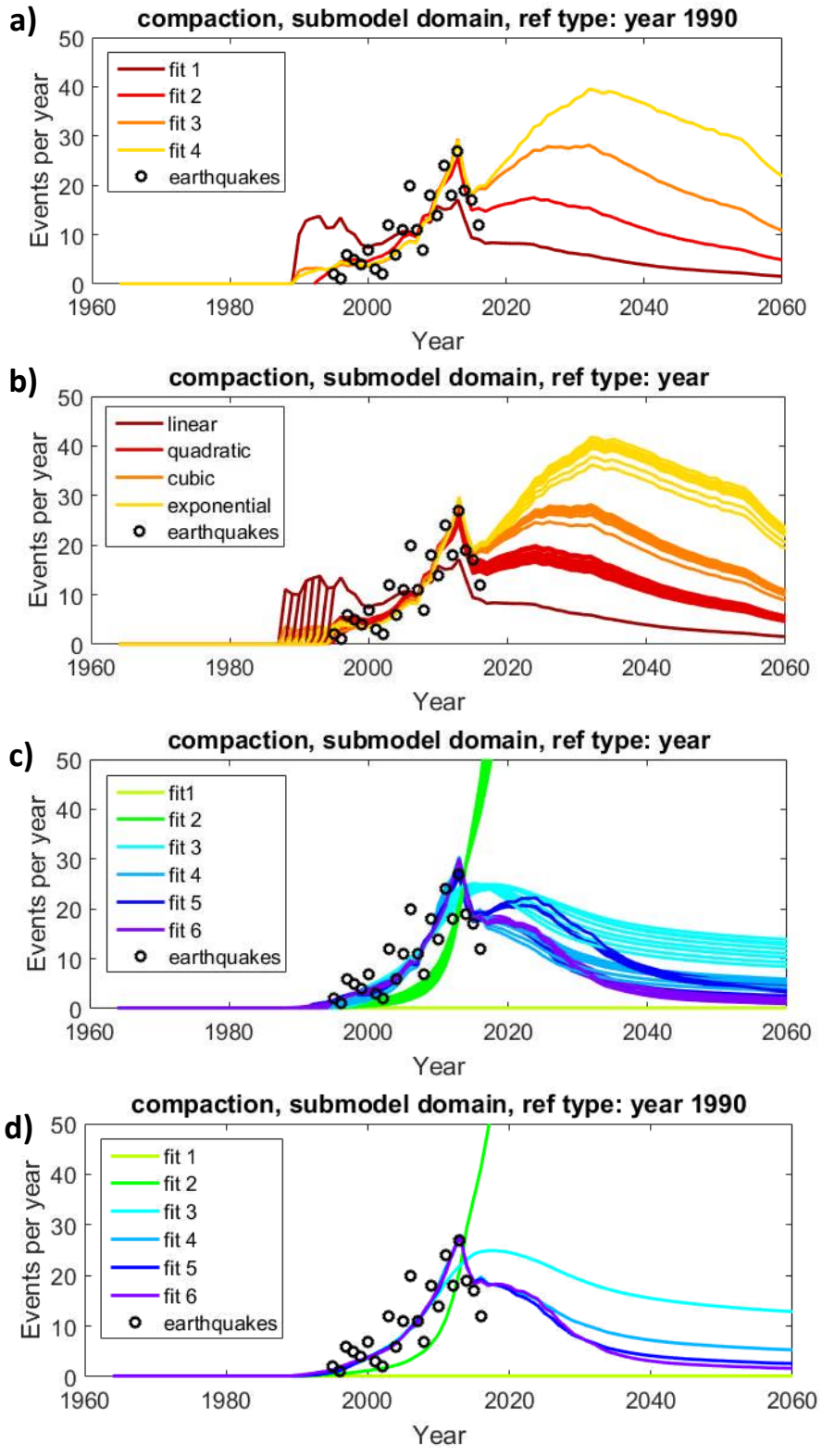

Figure 23: Similar to Figure 11. Fits to compaction data, in the submodel domain, referenced to a year. Best fits are highlighted in (b) and (d) with the cubic the best fit in (b) and fit 6 the best fit in (d). Maps of forecast activity are shown in Figure 26 (cubic) and Figure 25 (fit 6) respectively.

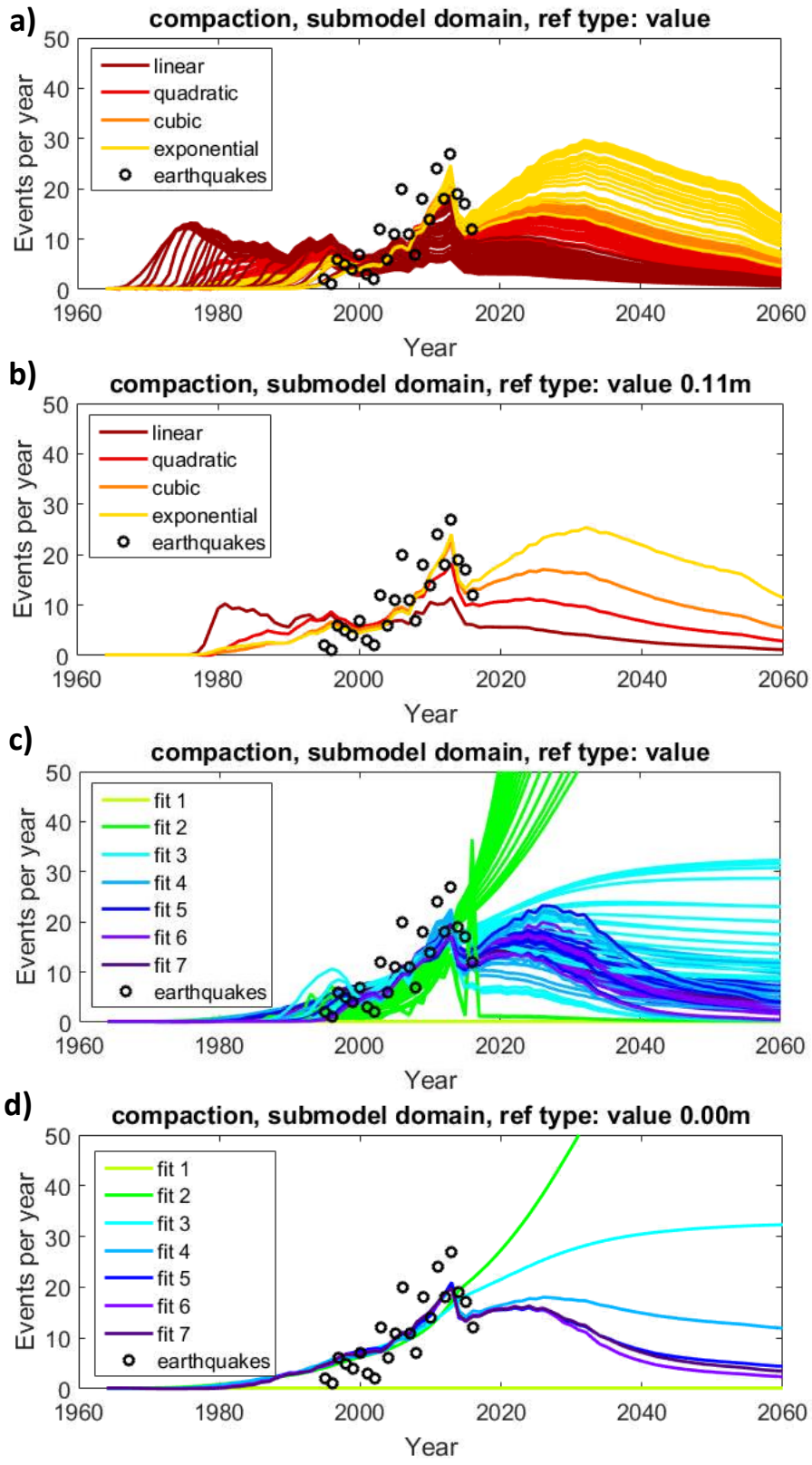

Figure 24: Similar to Figure 11. Fits to compaction data, in the submodel domain, referenced to specific values. Best fits are highlighted in (b) and (d) with cubic and fit 7 being the best respectively.

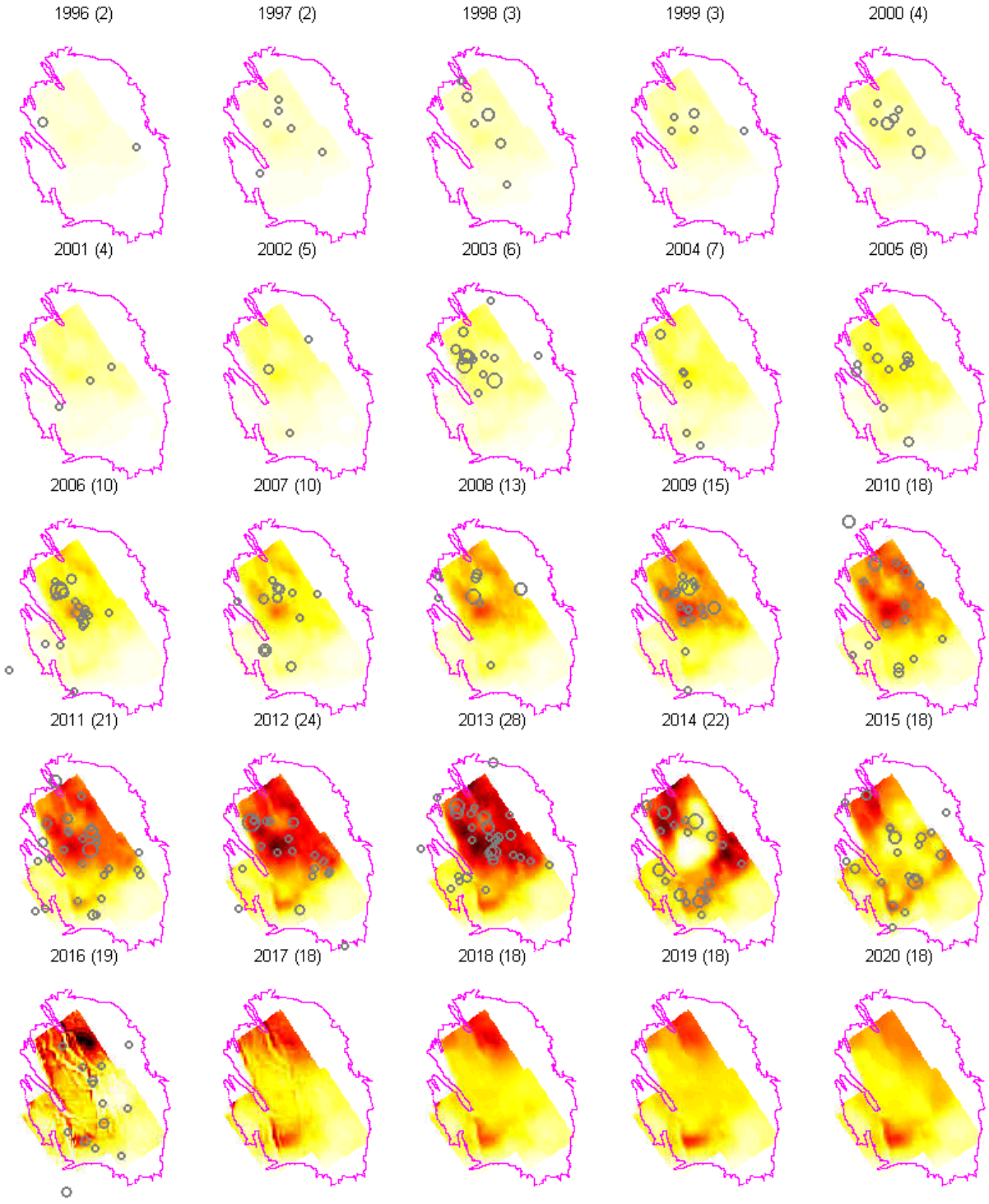

Figure 25: Maps of activity based on compaction data, fit to the submodel domain data, for the best generic Poisson process model, referenced to the year 1990, and for the 27 bcm production scenario. Actual activity is presented for a range of years. The number in parenthesis in the sub-figure title is the forecasted number of events in that year. Activity color bar ranges from 0-1e^{-7} events per m^2 per year

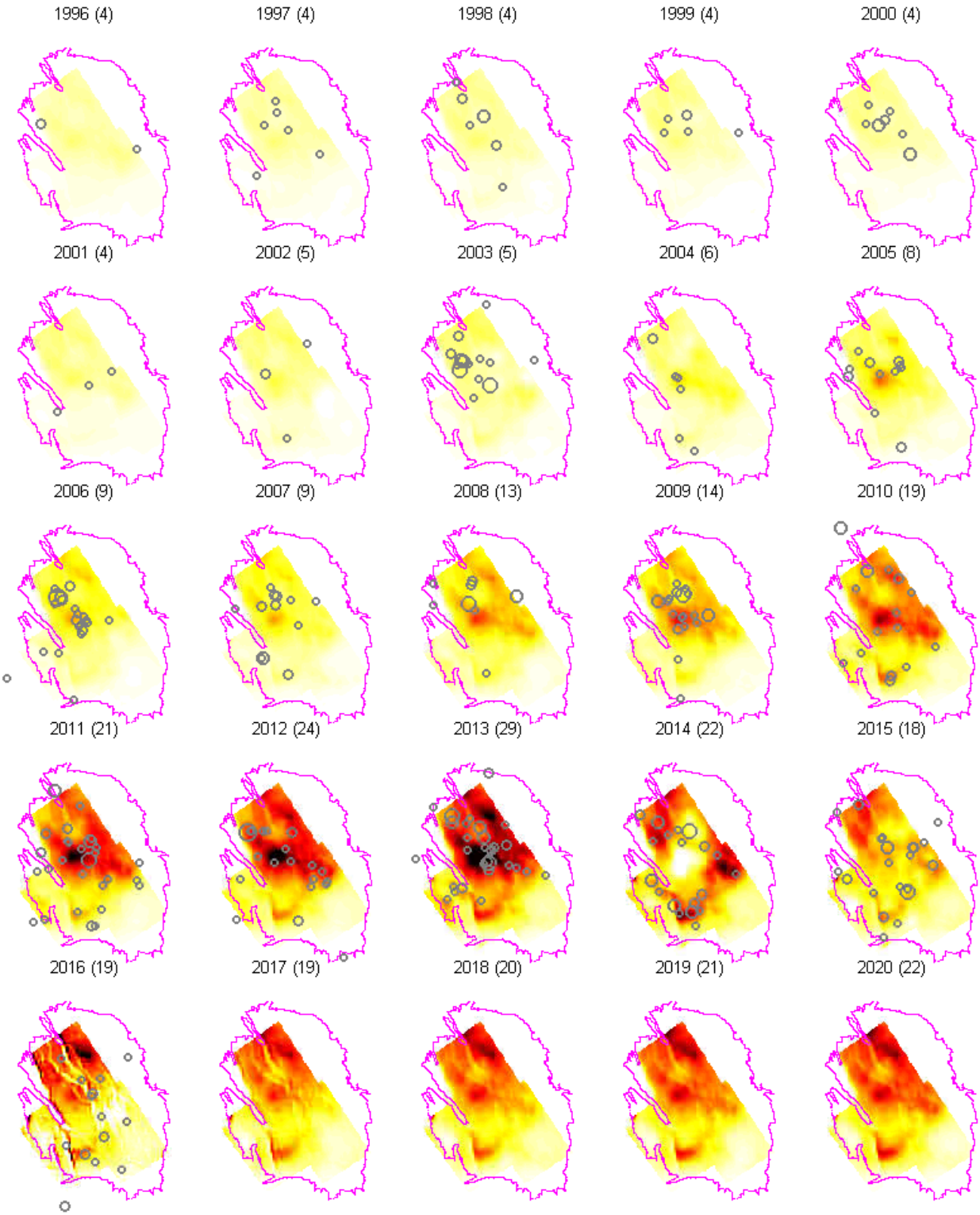

Figure 26: Maps of activity based on compaction data, fit to the submodel domain data, for the cubic specific Poisson process model, referenced to the year 1990, and for the 27 bcm production scenario. Actual activity is presented for a range of years. The number in parenthesis in the sub-figure title is the forecasted number of events in that year. Activity color bar ranges from 0-1e^{-7} events per m^2 per year

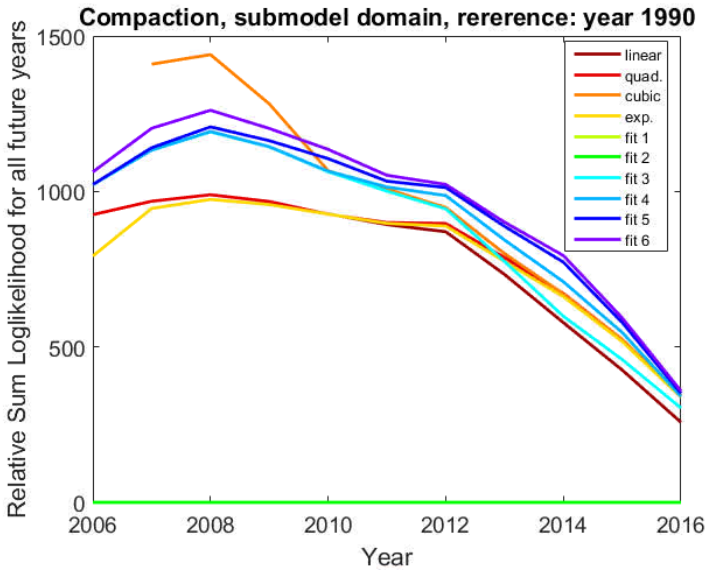

Figure 27: Same as Figure 19 but for reference to a value rather than a year.

3.2 Fault Slip Based Activity Models

As discussed in section 2.2, the fault moment occurs only at specific locations where there are faults captured in the geomechanical model. There is a fair amount of error in observed earthquake locations, so most events are assigned coordinates where there is no fault and hence no corresponding modeled moment release. With zero moment release, an activity rate at that coordinate would be zero, and this poses many obstacles to the MLE of model parameters (the estimation requires that the log be taken of the activity rate at the location of the observed earthquake and the log of zero is infinite). One way to overcome this is to use a Gaussian kernel to distribute the geomechanically modeled moment over a spatial area, and this removes many of the areas where an activity rate of zero would be forecasted.

Three sizes of kernel (3 km, 5 km and 7 km) were examined to determine if there is a better fit associated with one kernel size or another. The size is specified by the radius to the point that is equivalent to three standard deviations. The 7 km kernel results in the smoothest spatial distribution of moment (see Figure 28 for a comparison of the modeled moment as of Jan 1, 2017 for the three kernel sizes). For the small kernel size, the spatial distribution of modeled moment still resembles that of faults, but for the larger kernel sizes, the modeled moment distribution is very smoothly varying in space and the underlying character of the fault map is not preserved. For all kernel sizes, upon a visual examination there is a very good spatial correlation between the observed events and the areas of high moment release. However, in the 3 km case, there are earthquakes observed at locations with little to no moment release and this will result in those models being penalized during the maximum likelihood estimation. The 5 km and 7 km distribution models have a non-trivial amount of moment release at all points in the submodel domain and this will affect the model fitting. Results for the 3 km and 7 km distribution model will be presented in more detail. The results of the 5 km distribution model are intermediate to the presented results.

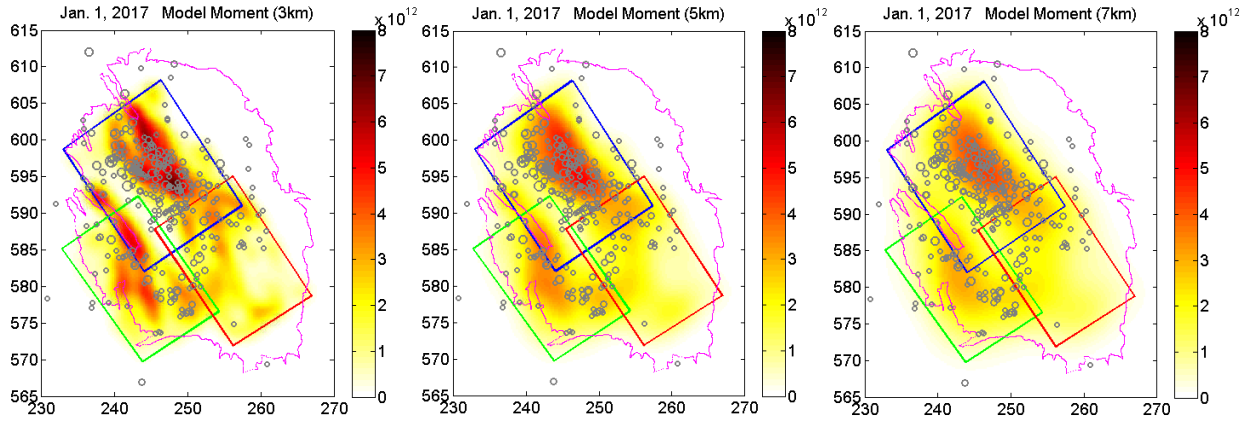

Figure 28: Comparison of cumulative moment release by fault slip in the geomechanical model as of January 1, 2017, referenced to 1990, for three different sizes of Gaussian kernels used to distribute the moment over a spatial area.

The log-likelihood and AIC values for specific and generic models fit to the moment data distributed using a 3 km kernel, are presented in Table 9. Similar to the compaction based results, models that are referenced to a year are a much better fit to the observed earthquakes than those that are referenced to a value. 1994 is the best year for both the specific and the generic models to use as a reference. The log-likelihood and AIC values prefer different specific model forms (cubic and quadratic respectively). All the model fits referenced to a year are presented in Figure 29. In comparison to the compaction based models, much lower activity rates are forecasted in the future years for the 3 km distributed moment based models. Also, especially for the specified model forms, there is very little difference between the fits and forecasts for the different specified model forms. Many parameters are included in the generic model fit (9 parameters were selected by the algorithm) and the generic model has a much higher (worse) AIC value than the specified model forms (a difference of 20 compared to a difference of 10 for the compaction models fit to the submodel domain), indicating that the generic model is not as appropriate as the specified models for this scenario.

All the model fits referenced to a slip value are presented in Figure 30. The best generic model referenced to a value is shown in Figure 30d and it is a poor representation of the observed earthquakes so it will not be discussed further. The specified model forms are a much better representation of the observations and the relatively trivial difference between the different specified model forms that was observed for the models referenced to a year persists when a reference slip value is used.

The predictive power of the models fit to a reference year are shown in Figure 31. Except for those models that are fit to the data ending January 1, 2014, the specified model forms are consistently more predictive than the generic models.

Table 9: Identical to Table 5 but for moment based fits using a 3 km kernel and only fit to the submodel domain. The best fits for each of the methodologies, for each type of reference, and for both AIC and log-likelihood criterions are indicated with red text. Model fits and parameter values for the reference years and values in red are presented in Table 10 and Figure 29-Figure 30.

	Log-likelihood					AIC				
Reference	Linear	Quadratic	Cubic	Exp.	Generic	Linear	Quadratic	Cubic	Exp.	Generic
1988	-4596.55	-4587.86	-4587.08	-4587.34	-4594.14	9197.11	9181.72	9182.16	9180.67	9206.29
1989	-4596.55	-4587.53	-4586.87	-4587.05	-4593.94	9197.11	9181.06	9181.75	9180.09	9205.88
1990	-4596.55	-4586.90	-4586.39	-4586.47	-4592.76	9197.11	9179.80	9180.77	9178.93	9203.52
1991	-4596.55	-4586.18	-4585.84	-4585.84	-4591.32	9197.11	9178.37	9179.69	9177.69	9200.64
1992	-4596.55	-4585.03	-4584.94	-4584.94	-4589.43	9197.11	9176.06	9177.88	9175.89	9196.86
1993	-4596.55	-4583.87	-4583.87	-4584.08	-4588.26	9197.11	9173.75	9175.75	9174.16	9194.51
1994	-4596.82	-4583.04	**-4582.93**	-4583.64	**-4587.65**	9197.64	**9172.08**	9173.85	9173.29	**9193.29**
1995	-4597.13	-4585.38	-4585.32	-4585.77	-4602.26	9198.26	9176.76	9178.63	9177.53	9220.53
0.0 m	-4758.96	-4686.18	-4684.48	-4699.66	**-4688.61**	9521.92	9378.36	9376.96	9405.31	**9383.23**
0.01 m	-4707.62	-4691.09	-4688.23	-4695.32	-4699.63	9419.23	9388.19	9384.45	9396.63	9413.26
0.02 m	-4690.87	-4688.62	-4686.78	-4690.56	-4724.78	9385.74	9383.25	9381.56	9387.13	9467.57
0.03 m	-4691.21	-4682.21	-4682.20	-4685.40	-4754.70	9386.42	9370.42	9372.39	9376.79	9527.41
0.04 m	-4694.81	-4681.63	-4677.90	-4704.75	-4835.45	9393.61	9369.27	9363.80	9415.50	9680.89
0.05 m	-4714.93	-4691.92	**-4677.07**	-4714.93	-4891.76	9433.85	9389.85	**9362.15**	9435.85	9793.52
0.06 m	-4779.16	-4748.54	-4721.17	-4779.16	-4988.57	9562.32	9503.08	9450.35	9564.32	9987.13
0.07 m	-4884.78	-4848.71	-4810.48	-4884.78	-5089.76	9773.56	9703.41	9628.97	9775.56	10193.52
0.08 m	-5025.56	-4992.09	-4957.46	-5025.56	-5274.74	10055.13	9990.19	9922.92	10057.13	10555.49
0.09 m	-5166.04	-5138.98	-5111.91	-5166.04	-5323.32	10336.08	10283.96	10231.82	10338.08	10658.64
0.10 m	-5297.99	-5277.16	-5277.16	-5297.99	-5455.90	10599.99	10560.31	10562.31	10601.99	10917.79
0.11 m	-5412.27	-5401.49	-5401.49	-5412.27	-5467.93	10828.55	10808.98	10810.98	10830.55	10943.85
0.12 m	-5456.13	-5450.52	-5450.52	-5456.13	-5478.78	10916.26	10907.04	10909.04	10918.26	10963.57

Table 10. Best fit parameters used to generate the models presented in Table 9. All fits were performed using the modeled moment distributed with a 3 km kernel and the earthquake catalog within the area of only the submodels.

Reference	Linear	Quadratic	Cubic	Exponential	Generic
1994	$\alpha = 1.307\ e\text{-}14$ $\delta = 2.229\ e\text{-}16$	$\beta = 2.971\ e\text{-}22$ $\alpha = 7.066\ e\text{-}15$ $\delta = 6.465\ e\text{-}15$	$\gamma = -1.381\ e\text{-}30$ $\beta = 3.688\ e\text{-}22$ $\alpha = 6.519\ e\text{-}15$ $\delta = 2.110\ e\text{-}14$	$\alpha = 8.264\ e\text{-}15$ $\beta = 1.085\ e\text{-}8$ $\delta = 3.894\ e\text{-}24$	$\alpha_0 = -22.29$ $\alpha_4 = 2.690\ e\text{-}6$ $\alpha_5 = -4.403\ e\text{-}13$ $\alpha_9 = 1.865\ e\text{-}20$ $\alpha_8 = 2.347\ e\text{-}21$ $\alpha_1 = 3.118\ e\text{-}7$ $\alpha_7 = -1.488\ e\text{-}13$ $\alpha_2 = -4.780\ e\text{-}15$ $\alpha_{10} = -2.555\ e\text{-}28$
0.00 m					$\alpha_0 = -22.29$ $\alpha_1 = 9.846\ e\text{-}8$ $\alpha_2 = -4.285\ e\text{-}16$
0.05 m	$\alpha = 6.585\ e\text{-}14$ $\delta = 2.083\ e\text{-}10$	$\beta = -1.880\ e\text{-}21$ $\alpha = 8.440\ e\text{-}14$ $\delta = 2.083\ e\text{-}10$	$\gamma = 1.315\ e\text{-}28$ $\beta = -7.351\ e\text{-}21$ $\alpha = 1.131\ e\text{-}13$ $\delta = 2.083\ e\text{-}10$	$\alpha = 6.585\ e14$ $\beta = 3.846\ e\text{-}15$ $\delta = 2.083\ e\text{-}10$	

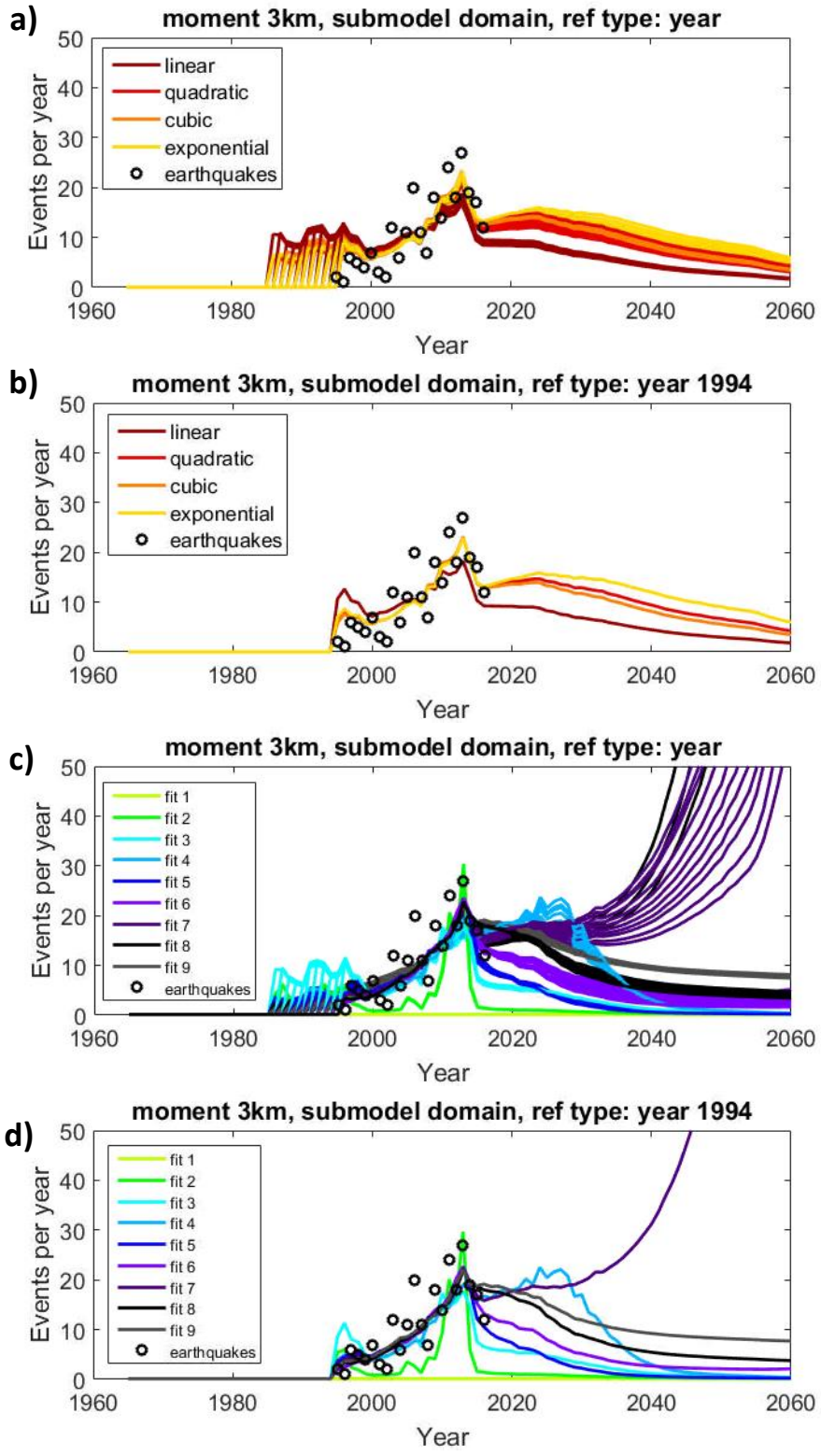

Figure 29: Similar to Figure 11. Fits to moment data with a 3 km kernel, in the submodel domain, referenced to a year. Best fits are highlighted in (b) and (d) with cubic and quadratic fits being the best in (b), depending on the metric used, and fit 9 being the best in (d).

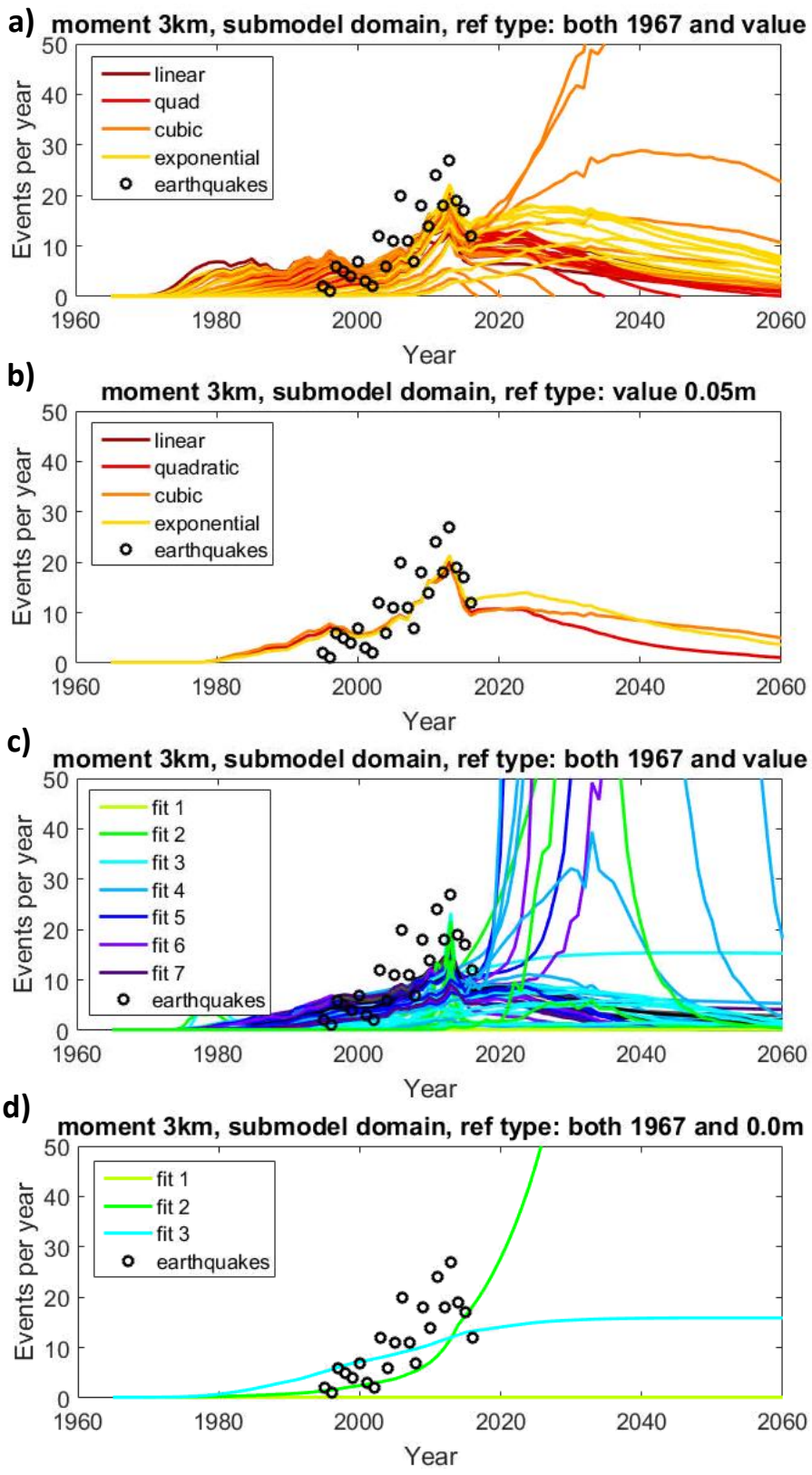

Figure 30: Similar to Figure 11. Fits to moment data with a 3 km kernel, in the submodel domain, referenced to a slip value. Best fits are highlighted in (b) and (d) with cubic and fit 3 being the best respectively.

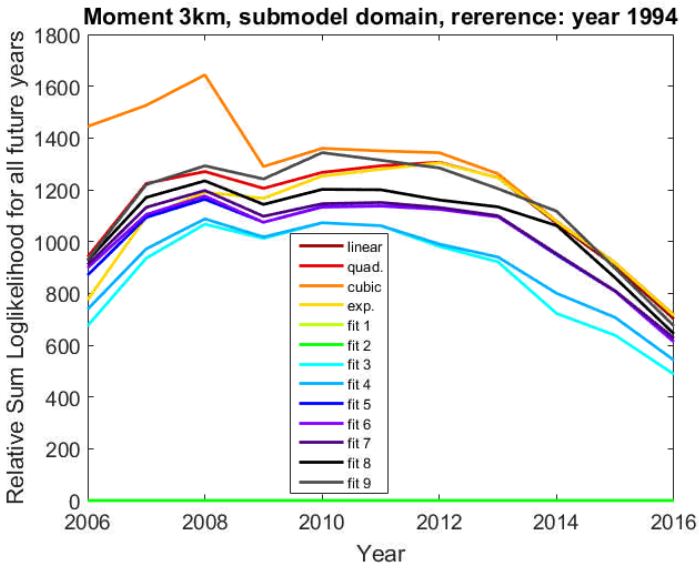

Figure 31: Same as Figure 19 but for reference to a value rather than a year.

The log-likelihood and AIC values for specific and generic models fit to the moment data distributed using a 7 km kernel are presented in Table 11. Similar to all other results presented, models that are referenced to a year are a much better fit to the observed earthquake activity than those that are referenced to a value. The best reference year for the specific models is 1993 while the best reference year for the generic models is 1988. Similar to the 3 km kernel results, the specific models are much better than the generic model (an AIC difference of ~20). The log-likelihood value suggests that the cubic is the best fit to the observations, but the AIC value indicates that the quadratic would be more predictive. All of the fits are shown in Figure 32. As with the 3 km distribution results, the cubic and quadratic fits are very similar to one another.

All the model fits referenced to a year are presented in Figure 33. Similar to the 3 km distribution model data, the best generic model referenced to a value (shown in Figure 33d) yields a poor representation of the observed earthquakes so it will not be discussed further. The specified model forms referenced to a year are a much better representation of the observations and there is only a small difference between the quadratic and the cubic forms, which are both good fits to the observations. Hence the models referenced to a year rather than a value are greatly preferred. An example of the activity maps for the quadratic model, referenced to 1993 is shown in Figure 34.

As with other scenarios, the predictive power of the models referenced to a year is examined in Figure 35. Historically the generic model was generally the most predictive but recently the specified cubic and quadratic forms became the most predictive. The variation in the model fits is shown in Figure 36.

Because the models fit to the 3 km distribution model moment data and the 7 km distribution model moment data were made over the same domain area and the same set of earthquakes, the log-likelihood and AIC values can be directly compared. The best 3 km distribution model has an AIC value of 9172 while the best 7 km distribution model has an AIC value of 9054. This difference is very significant and indicates

that the smoother activity maps of the 7 km distribution model are much better for modeling the observations.

Table 11: Identical to Table 5 but for distributed moment based fits using a 7 km kernel and only fit to the submodel domain. The best fits for each of the methodologies, for each type of reference, and for both AIC and log-likelihood criterions are indicated with red text. Model fits and parameter values for the reference years and values in red are presented in Table 12 and Figure 32-Figure 33.

	Log-likelihood					AIC				
Ref.	Linear	Quadratic	Cubic	Exp.	Generic	Linear	Quadratic	Cubic	Exp.	Generic
1987	-4578.46	-4526.30	-4525.89	-4534.08	-4530.95	9160.92	9058.60	9059.78	9074.17	9073.90
1988	-4578.46	-4525.98	-4525.49	-4534.09	**-4529.75**	9160.92	9057.96	9058.99	9074.19	**9073.50**
1989	-4578.46	-4526.34	-4525.90	-4534.33	-4545.95	9160.92	9058.67	9059.80	9074.66	9099.89
1990	-4578.46	-4526.28	-4525.93	-4534.11	-4537.50	9160.92	9058.57	9059.87	9074.22	9085.00
1991	-4578.46	-4525.97	-4525.63	-4533.84	-4538.12	9160.92	9057.93	9059.26	9073.69	9086.23
1992	-4578.46	-4524.76	-4524.21	-4533.43	-4538.41	9160.92	9055.52	9056.43	9072.87	9086.82
1993	-4578.46	-4524.22	**-4523.49**	-4533.25	-4539.38	9160.92	**9054.45**	9054.99	9072.51	9088.77
1994	-4578.72	-4525.06	-4524.15	-4533.98	-4541.85	9161.44	9056.11	9056.29	9073.97	9093.70
1995	-4579.09	-4533.05	-4532.29	-4539.50	-4534.68	9162.18	9072.10	9072.59	9085.00	9083.36
0.0 m	-4758.96	-4686.18	-4684.48	-4699.66	-4654.75	9521.92	9378.36	9376.96	9405.31	9321.51
0.01 m	-4674.08	-4554.83	**-4553.47**	-4585.21	**-4574.83**	9352.17	9115.66	**9114.95**	9176.41	**9155.65**
0.02 m	-4635.27	-4564.12	-4559.95	-4585.05	-4592.02	9274.54	9134.24	9127.91	9176.11	9190.04
0.03 m	-4605.54	-4573.86	-4563.48	-4583.94	-4613.32	9215.09	9153.72	9134.96	9173.88	9232.63
0.04 m	-4586.53	-4580.18	-4568.60	-4582.03	-4644.34	9177.05	9166.35	9145.21	9170.05	9294.68
0.05 m	-4575.98	-4575.58	-4571.41	-4575.98	-4699.69	9155.96	9157.16	9150.82	9157.96	9405.37
0.06 m	-4582.36	-4570.47	-4570.33	-4582.36	-4709.11	9168.72	9146.94	9148.67	9170.72	9428.22
0.07 m	-4617.32	-4588.98	-4579.92	-4617.32	-4800.68	9238.65	9183.97	9167.85	9240.65	9613.37
0.08 m	-4681.02	-4642.34	-4642.34	-4681.02	-5023.00	9366.04	9290.69	9292.69	9368.04	10053.99
0.09 m	-4790.28	-4745.06	-4745.06	-4790.28	-5040.44	9584.56	9496.13	9498.13	9586.56	10088.87
0.10 m	-4948.25	-4901.30	-4901.30	-4948.25	-5220.49	9900.50	9808.61	9810.61	9902.50	10448.98
0.11 m	-5163.82	-5127.39	-5127.39	-5163.82	-5431.02	10331.63	10260.78	10262.78	10333.63	10868.04
0.12 m	-5314.79	-5314.79	-5314.79	-5314.79	-5451.73	10633.57	10635.57	10637.57	10635.57	10909.46

Table 12: Best fit parameters used to generate the models presented in Table 11. All fits were performed using the modeled moment distributed with a 7 km kernel and the earthquake catalog within the area of only the submodels.

Reference	Linear	Quadratic	Cubic	Exponential	Generic
1988					α_0 =-22.76 $\alpha_1 = 1.145\ e\text{-}7$ $\alpha_3 = -8.584\ e\text{-}24$ $\alpha_4 = 4.070\ e\text{-}6$ $\alpha_5 = -1.193\ e\text{-}12$ $\alpha_7 = -5.047\ e\text{-}14$ $\alpha_9 = 1.752\ e\text{-}20$
1993	$\alpha = 1.398\ e\text{-}14$ $\delta = 2.306\ e\text{-}16$	$\beta = 8.746\ e\text{-}22$ $\alpha = -1.180\ e\text{-}15$ $\delta = 3.625\ e\text{-}15$	$\gamma = -6.210\ e\text{-}30$ $\beta = 1.078\ e\text{-}21$ $\alpha = -2.031\ e\text{-}15$ $\delta = 7.962\ e\text{-}16$	$\alpha = 4.773\ e\text{-}15$ $\beta = 2.964\ e\text{-}8$ $\delta = 1.979\ e\text{-}15$	
0.01 m	$\alpha = 1.236\ e\text{-}14$ $\delta = 2.225\ e\text{-}16$	$\beta = 7.614\ e\text{-}22$ $\alpha = -4.397\ e\text{-}15$ $\delta = 2.083\ e\text{-}10$	$\gamma = -5.063\ e\text{-}30$ $\beta = 9.797\ e\text{-}22$ $\alpha = -5.421\ e\text{-}15$ $\delta = 2.083\ e\text{-}10$	$\alpha = 2.853\ e\text{-}15$ $\beta = 3.058\ e\text{-}8$ $\delta = 9.075\ e\text{-}14$	$\alpha_0 = -22.29$ $\alpha_1 = 2.069\ e\text{-}7$ $\alpha_2 = -1.838\ e\text{-}15$

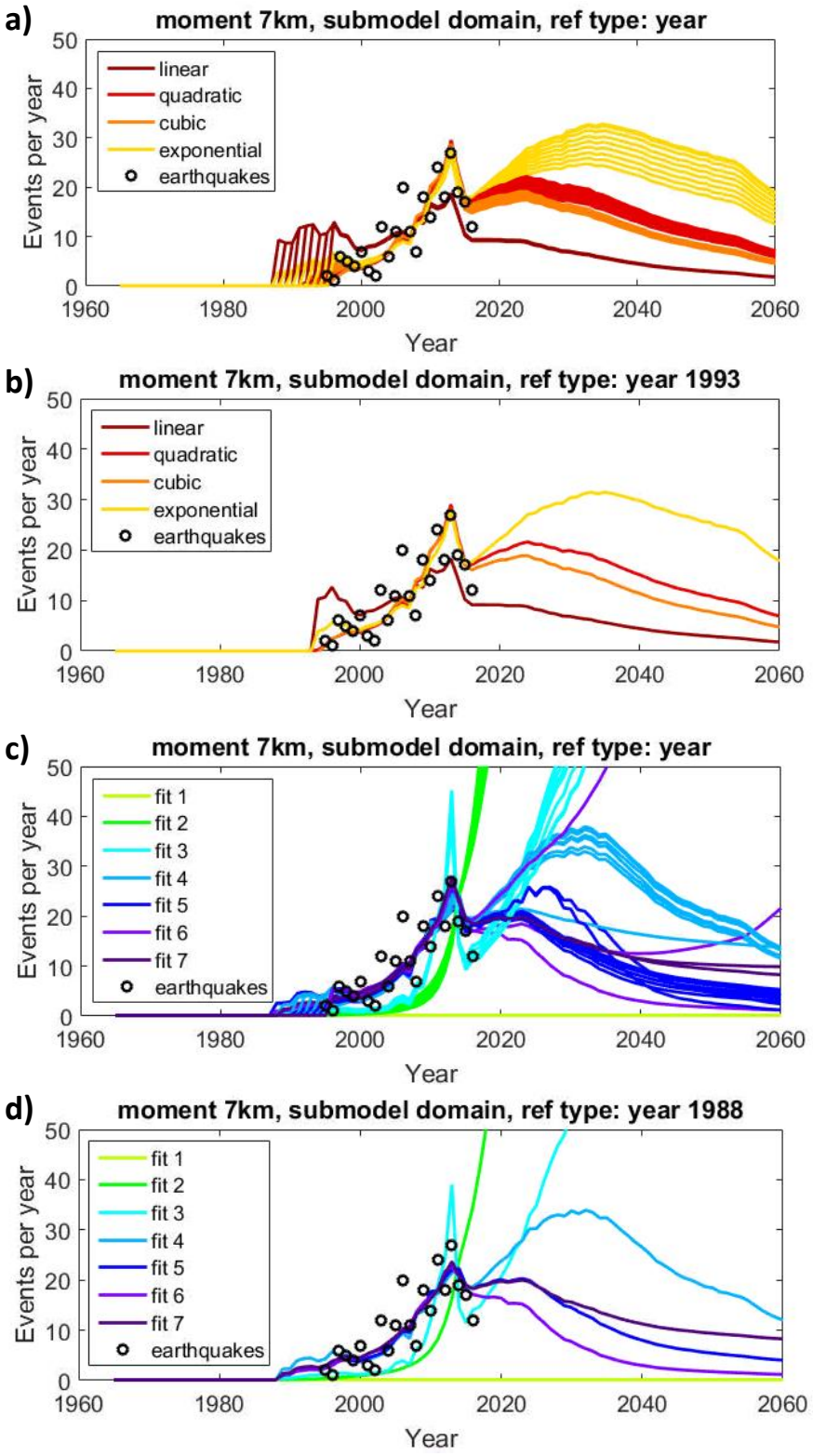

Figure 32: Similar to Figure 11. Fits to moment data distributed with a 7 km kernel, in the submodel domain, referenced to a year. Best fits are highlighted in (b) and (d) with cubic and quadratic fits being the best in (b), depending on the metric used, and fit 7 being the best in (d).

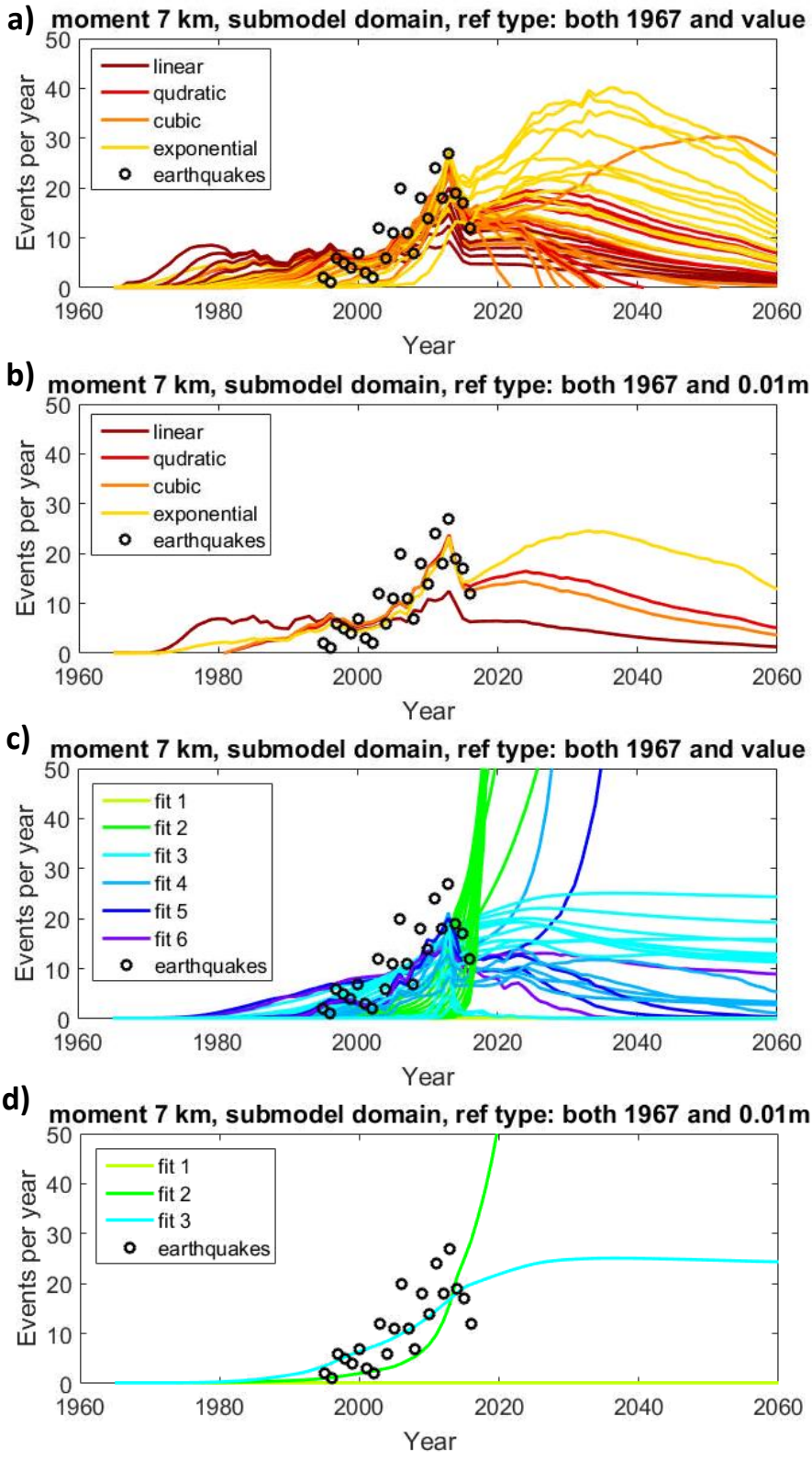

Figure 33: Similar to Figure 11. Fits to moment data distributed with a 7 km kernel, in the submodel domain, referenced to the year 1967 and then a value. Best fits are highlighted in (b) and (d) with cubic and quadratic fits being the best in (b), depending on the metric used, and fit 3 being the best in (d).

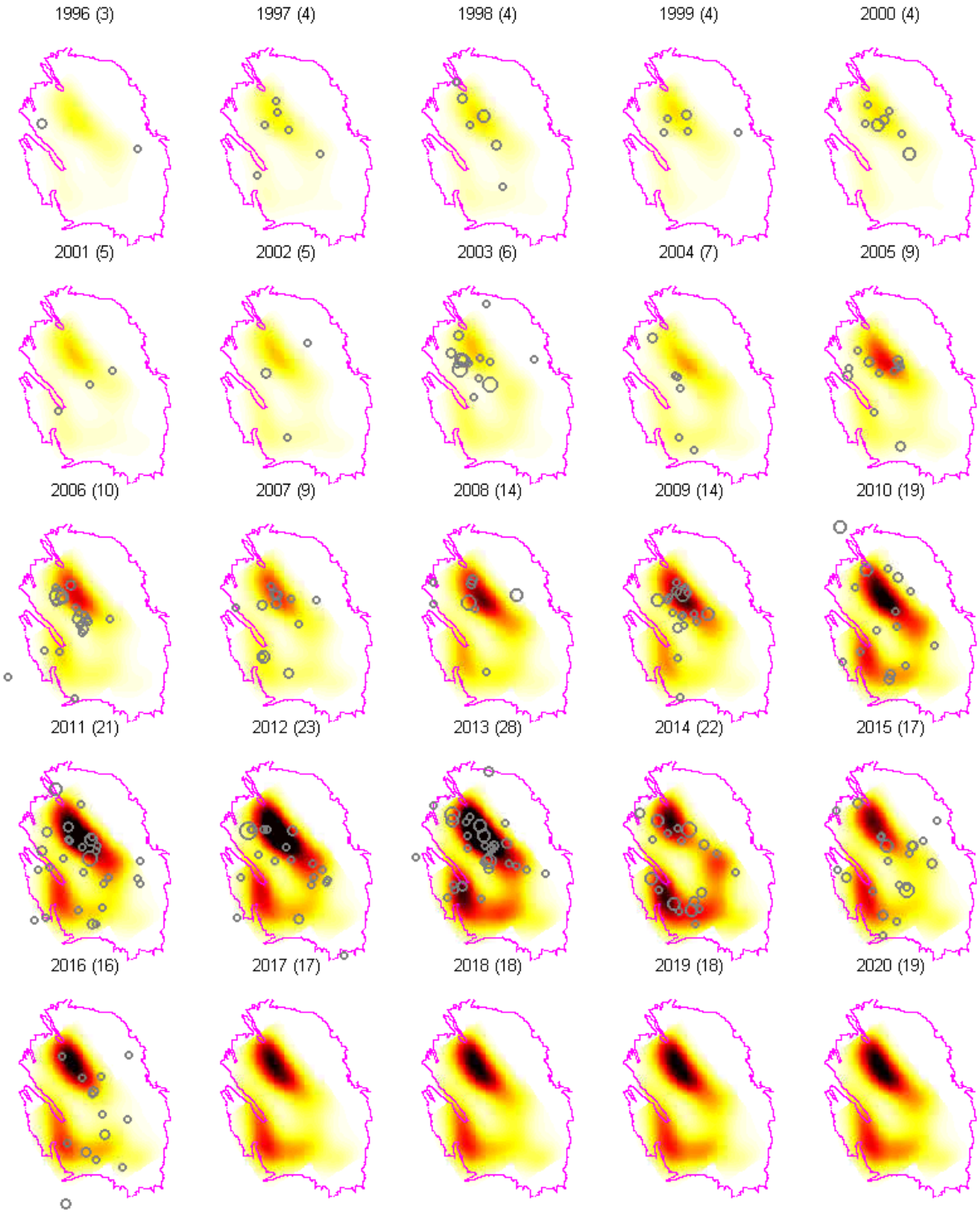

Figure 34: Maps of activity based on moment data distributed using a 7 km Gaussian kernel, fit to the submodel domain data, for the quadratic specific Poisson process model, referenced to the year 1993, and for the 27 bcm production scenario. Actual activity is presented for a range of years. The number in parenthesis in the sub-figure title is the forecasted number of events in that year. Activity color bar is for 0-1e^{-7} events per m^2 per year

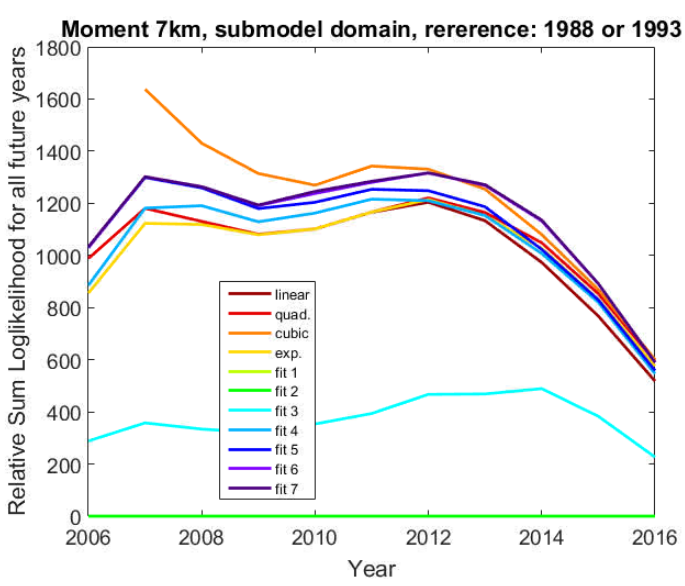

Figure 35: Same as Figure 19 but for a 7 km distribution of moment referenced to a year.

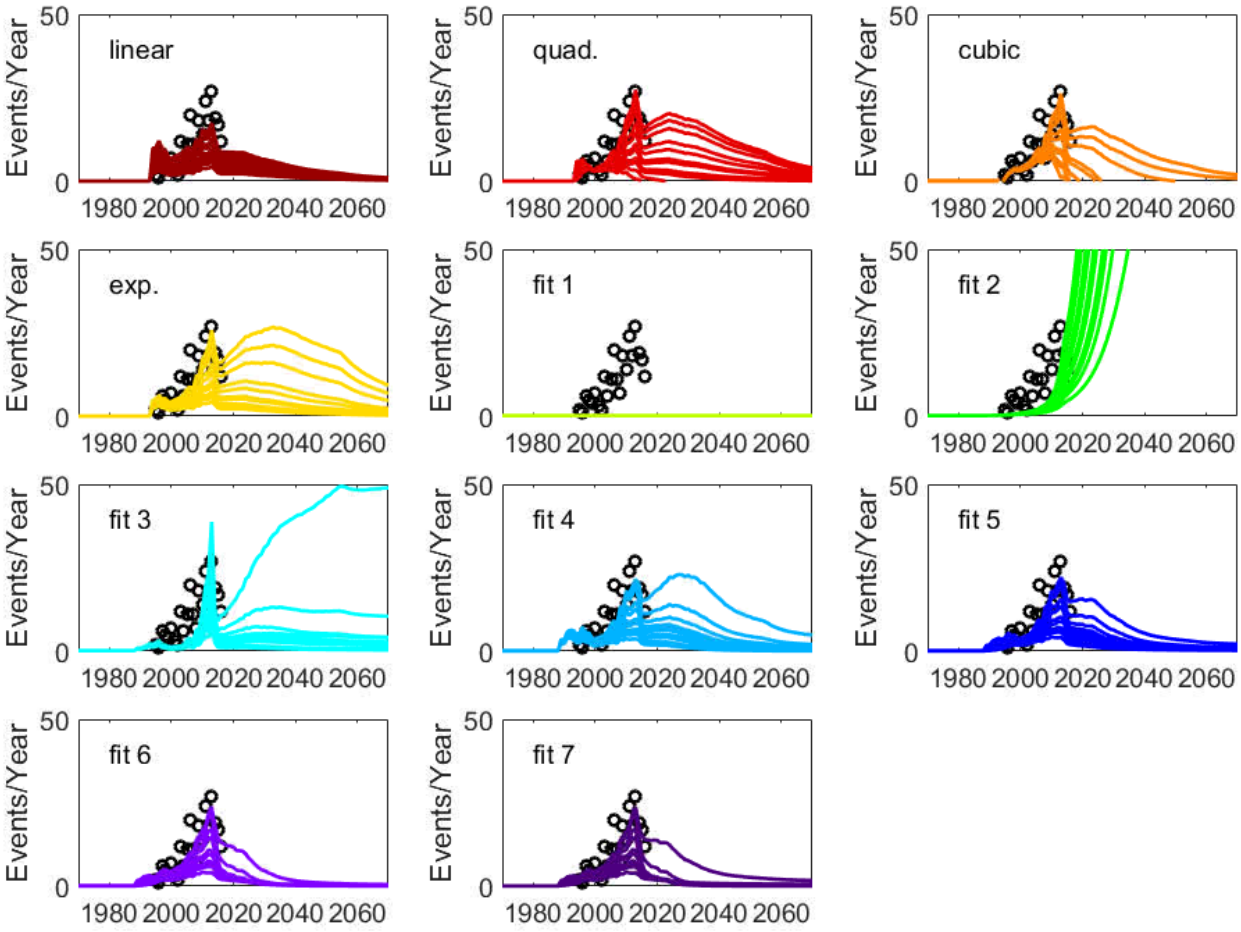

Figure 36: Same as Figure 21 but for moment data distributed using a 7 km Gaussian kernel and referenced to a year.

4.0 Discussion

Reference years were preferable to reference values for both compaction and fault moment based models. The specified exponential model used by Bourne and Oates (2015a,b) is a conservative assumption that can be made because it frequently results in the highest forecasted activity rates. The cubic or quadratic specified models are frequently preferred over the exponential except for the case of compaction fit to the entire field domain. In this scenario the exponential has the best AIC value but the cubic has the best log-likelihood value. If fault moment is considered, the more diffuse moment based models (using a 7 km kernel) give significantly better fits to the earthquake observations than the more localized fault moment models (3 km kernel).

In this section a subset of models are examined more closely to determine the effect of the model fits on hazard maps and implications for activity rate based production caps. A comparison of the field wide compaction based models is discussed first, followed by a comparison of the fault and compaction based models in the submodel domain.

4.2 Field Wide Compaction Based Models

In section 3.1.1 the activity maps for five field wide compaction based models are presented. The five models result in similar spatial distributions of activity but there is a fair range in the number of events that would be forecasted to occur over the next 5 years for the 27 bcm production scenario. Figure 37 shows the PGA (at a 10% chance of exceedance in 50 years) for the five scenarios. These maps were generated using the maximum magnitude distribution determined by a panel of experts during the Maximum magnitude workshop (Coppersmith et al., 2016) and a 50-50 weighting on the upper and middle branches of the version 2 GMPE (Bommer et al., 2015b). Because the version 2 GMPE is applied with a Monte Carlo framework, we accounted for uncertainty using the standard deviation values from version 1 (Bommer et al., 2015a). The spatial patterns of the hazard maps (PGA with a 10% probability of exceedance in 50 years) are very similar to one another despite the differences in the degree of activity localization between the models. The maximum PGA ranges from 0.149-0.168 g for the five models considered. This is a very small range given the variation in the input models and the number of events that are forecasted. The models used as input for (a), (b) and (c) are far better fits to the data than those shown in (d) and (e). When only the top three performing models are considered, the range in maximum PGA reduces to 0.153-0.168 g. This narrow range reflects a reasonable amount of uncertainty in the hazard calculation.

With the recent decrease in activity the specified model forms are becoming more predictive than the generic model forms. While the generic model form is currently the most predictive model (Figure 37a) an additional year or two of low seismic activity rates could potentially make this model less predictive than the cubic and exponential forms (Figure 37b and c). For some of the moment based models a transition to the specified forms being more predictive has already occurred. For this reason, the exponential and the cubic forms are the preferred model forms. The AIC value of the exponential form is lower making it a better representation of the seismicity given the number of parameters used to fit the model, but the cubic model fits the historical data better than the exponential. Both of these models

should be used going forward as a measure of the uncertainty range in the forecasted seismicity rates and hazard maps.

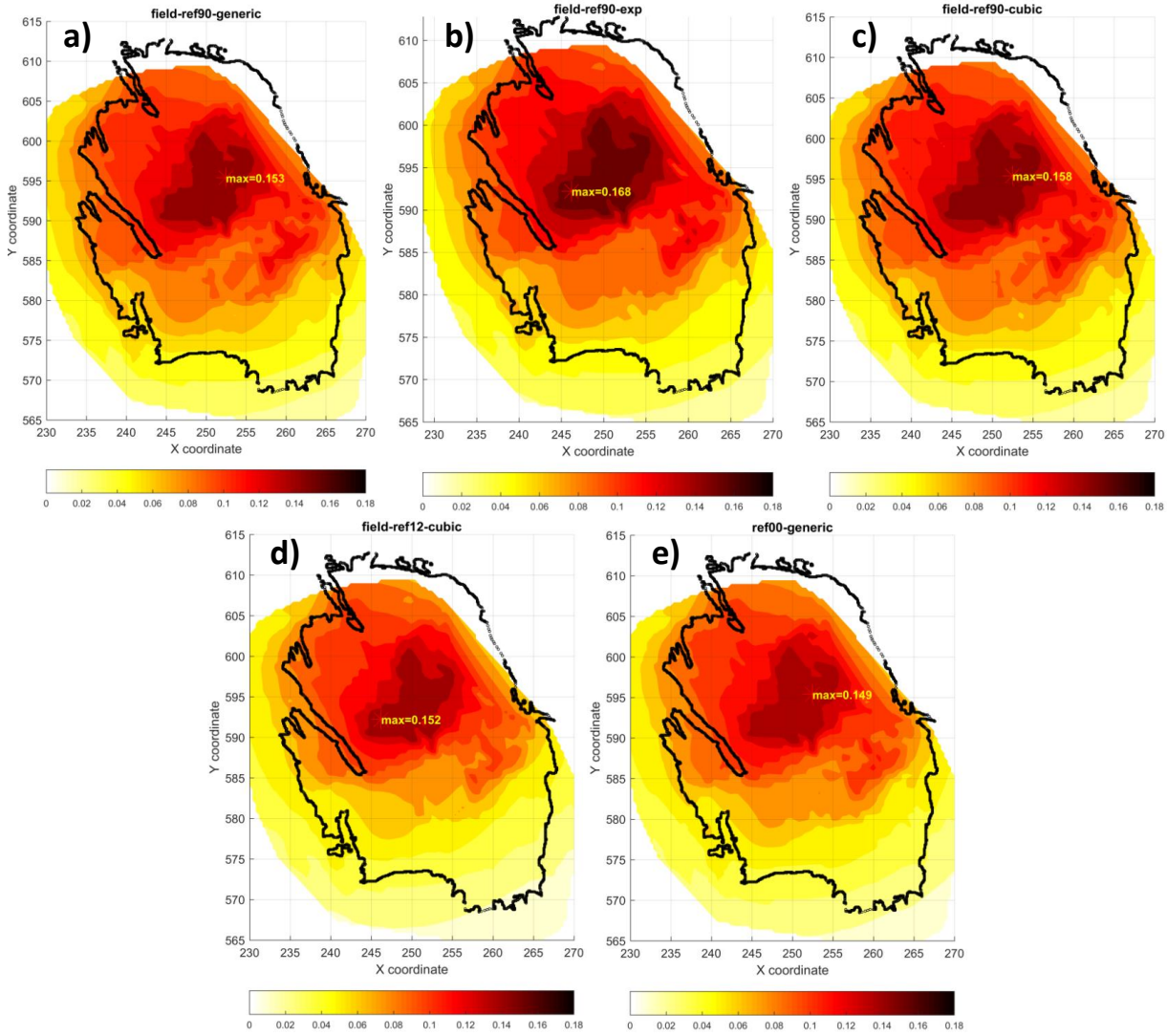

Figure 37: PGA (10% probability of exceedance in 50 years) hazard maps for the five best activity models based on the field wide compaction data. (a) generic model referenced to 1990; (b) exponential specific model referenced to 1990; (c) cubic specific model referenced to 1990; (d) cubic specific model referenced to 0.12 m; (e) generic model referenced to 0.0 m. Despite the differences in activity forecast maps, the hazard maps are very similar. The models used as input for (a), (b) and (c) yield far better fits to the data than those shown in (d) and (e).

4.1 Comparison of Compaction and Fault Based Models

4.1.1 Best Fault and Compaction based Models for Comparison

A comparison of the compaction and fault based moment models can only be made in the submodel domain since the faulted geomechanical model does not exist across the domain of the entire field.

The best AIC value for a fault moment based model was 9054.45 for the 7 km Gaussian kernel, quadratic model referenced to 1993. This was followed closely behind by the 7 km Gaussian kernel cubic model, referenced to 1993, with an AIC value of 9054.99 (values in Table 11). In comparison, the best compaction based model is the generic model, referenced to 1988, with an AIC value of 9110.23. Many results were presented in section 3.1.2 for the compaction based model referenced to 1990 (rather than 1988). That model had an AIC value of 9112.0 which is only slightly worse than the 1988 reference year compaction based model. An AIC value of ~9110 is substantially higher than an AIC value of 9054 indicating that the 7 km Gaussian kernel moment based activity maps may be better activity models than those that are compaction based. In comparison, the best 3 km Gaussian kernel fault based model AIC value is 9172.08, which is for the quadratic model referenced to 1993. This is worse than the AIC value for the best compaction based model.

The poor AIC value for the 3 km distributed moment based model is surprising given the high spatial correlation between the observed events and the fault slip data shown in Figure 28a. The poor fit is believed to be due to the fact that seismic activity is observed in locations where the 3 km distribution has little to no fault moment release. Use of a larger kernel size disperses the activity more so this does not occur but the high degree of spatial correlation between fault slip and observed seismicity is preserved (Figure 28c).

Five models are chosen for comparison using just the submodel domain. An activity map is needed over a larger domain, but this submodel comparison is sufficient to determine the magnitude of the model effect on the activity levels and the PGA hazard map. The five models selected are:

1. Fault moment distributed with a 3 km Gaussian kernel, referenced to 1994, quadratic specified model – this is the lowest AIC valued model but not the lowest log-likelihood (-4583.04 for the quadratic vs. -4582.93 for the cubic). However, the log-likelihood values are very close and the cubic and quadratic models are very similar in their activity forecasts with the cubic forecasting slightly less activity. Of the five models considered this is the poorest fit.
2. Fault moment distributed with a 7 km Gaussian kernel, referenced to 1993, quadratic specified model – this is the lowest AIC valued model but not the lowest log-likelihood (-4524.22 for the quadratic vs. -4523.49 for the cubic). However, the log-likelihood values are close and the quadratic model predicts higher activity than the cubic model. Of the five models considered this is the best fit
3. Compaction, referenced to 1990, generic model – this is not the lowest AIC value (compare 9110.23 for 1988 to 9112.0 for 1990). However, 1990 is the year with the best log-likelihoods for both the specific and generic models, a good reference year for the field wide models and the reference year used by Shell in the last HRA submission. This model forecasts comparatively low levels of seismicity (Figure 11d) that are not consistent with many of the other model predictions so this model is an outlier within the group
4. Compaction, referenced to 1990, exponential model – this is not the lowest AIC or log-likelihood choice, but it is the most similar to the NAM HRA submission.
5. Compaction, referenced to 1990, cubic model – this model has the best AIC and log-likelihood values for the specified model forms fit to compaction and referenced to a year. The generic

model (model 3) has a lower AIC but an outlier future forecast. Hence this cubic model is the most best supported compaction based model fit.

Model 1 does not fit the data as well as the others and model 3 has an anomalous forecast so they are included to provide a bound on the level of seismicity expected. Model 2 yields the best fit and models 4 and 5 also yield good fits. The differences in forecasts from these three models provide some idea about the variability that is reasonable.

4.1.2 Comparison of Activity in the Near Term

The total activity for the 5 models in the submodel domain is shown in Figure 38. The five models make very different forecasts about the future level of activity. The generic compaction model (model 3 - blue line) is different from all the other models shown here and the large decrease in activity is not seen in many of the other model fits presented in section 3. Therefore, even though this model has the lowest AIC value of the compaction models, and it is the best representation of the historical seismicity, it is the least conservative model and should not be the only scenario carried forward.

The response of the regulator to the most recent Winningsplan submission was to base a production level recommendation on the number of forecasted events and not the seismic hazard level (Kamp, 2016). This is a challenging metric on which to base a production cap because activity forecasts are based on a Poisson process and the observed number of seismic events in a given year will be highly variable around an expected rate. Even if the expected rate is lower than the 2015 level, from a statistical point of view it is possible that a larger number of events may be observed in at least one of the next five years. At the time of writing, the regulator recommendation was that the number of yearly events in the next five years should not exceed the activity level observed in 2015. Figure 38 shows significant differences between the 5 models over this five year interval.

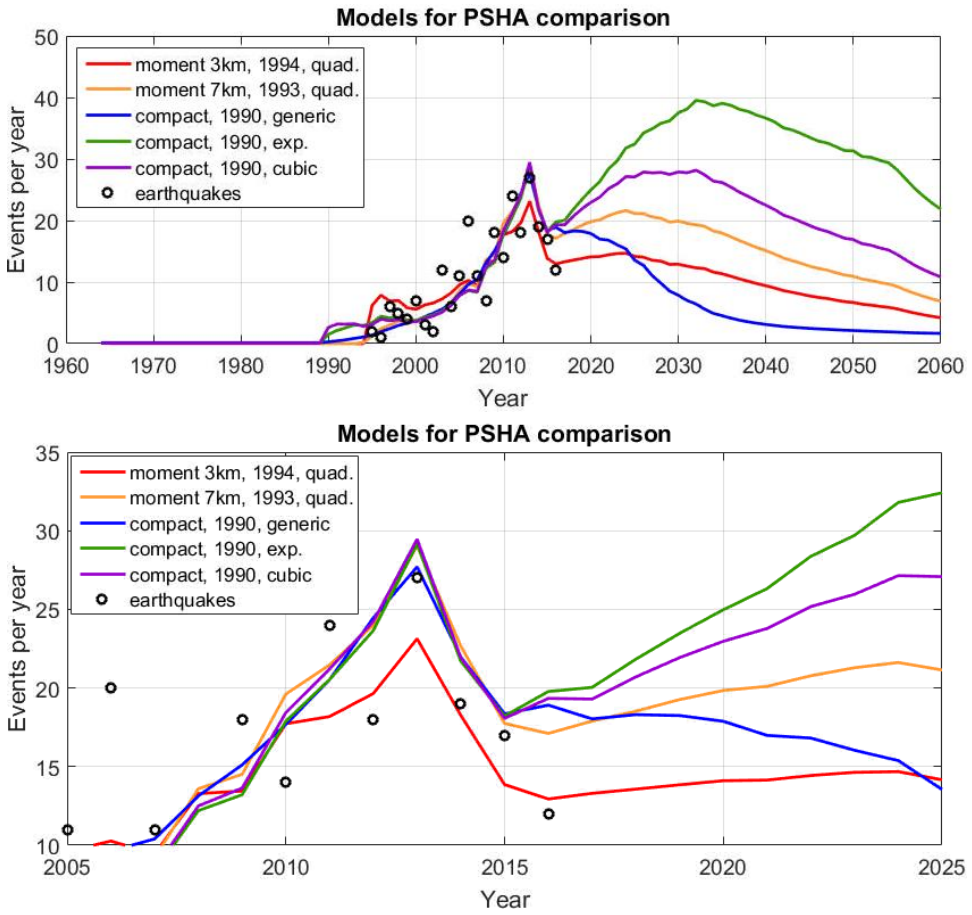

Figure 38: Total activity in the submodel domain for the five models closely examined. Same models are shown in both figures but lower figure is a close up of the current time frame. All forecasts are based on a 27 bcm production scenario.

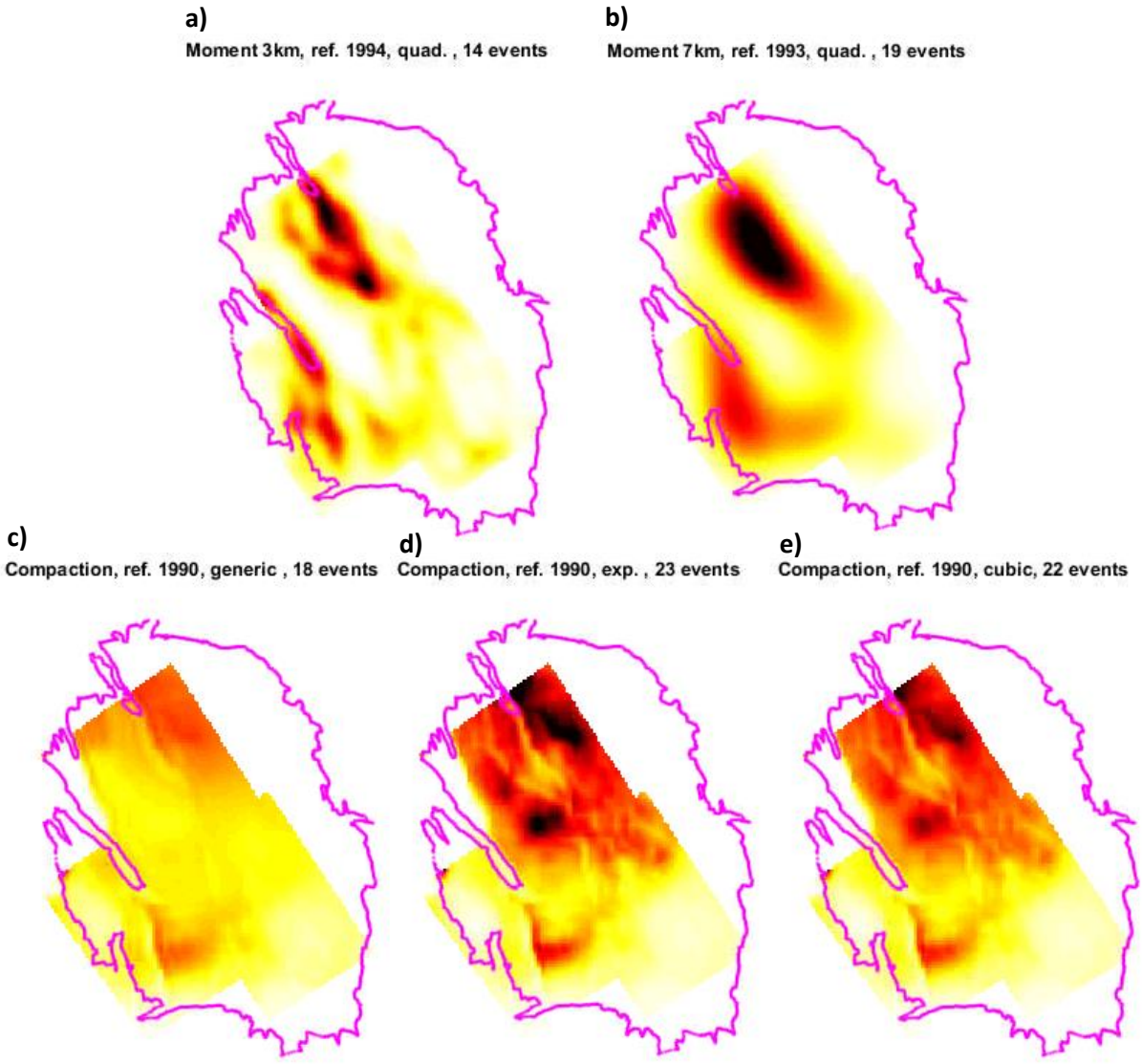

Figure 39: Average activity over the next 5 years for the four models under consideration (a) model 1 - 3 km distribution of fault moment, referenced to 1994, quadratic specified model; (b) model 2 - 7 km distribution of fault moment, referenced to 1993, quadratic specified model; (c) model 3 - Compaction, referenced to 1990, generic model; (d) model 4 - Compaction, referenced to 1990, exponential model; (e) model 5 - Compaction, referenced to 1990, cubic model.

In addition to the differences in the total activity rate the five models also result in different spatial distributions of seismic activity. The PGA hazard calculation is based on the activity map over the next five years (activity from January 1, 2017 to December 31, 2021) so average maps over this time frame are shown in Figure 39. The activity ranges from an average of 14-23 events per year but the best model has 19 events per year and the second best has 22 events per year.

4.1.3 Comparison of PGA Hazard Maps

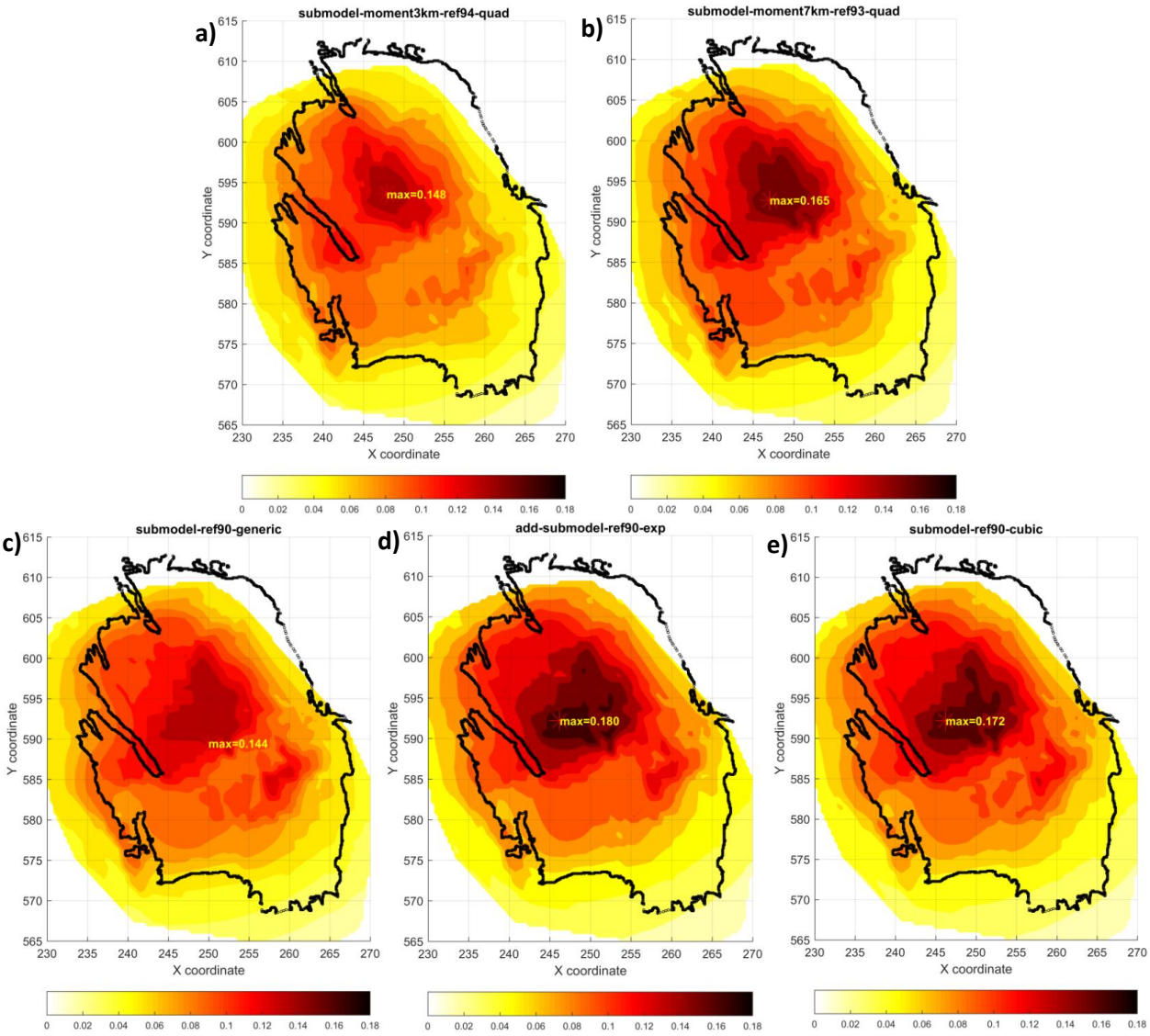

Figure 40: PGA hazard maps for the four activity models shown in Figure 39 plotted at the 10% in 50 years exceedance level. (a) model 1 - 3 km fault moment, referenced to 1994, quadratic specified model; (b) model 2 - 7 km distribution of fault moment, referenced to 1993, quadratic specified model; (c) model 3 - Compaction, referenced to 1990, generic model; (d) model 4 - Compaction, referenced to 1990, exponential model; (e) model 5 - Compaction, referenced to 1990, cubic model.

One potential impact of the seismological model is the effect on resulting hazard maps. Figure 40 shows the PGA (at a 10% chance of exceedance in 50 years) for the five models. These maps were generated using the maximum magnitude distribution determined by a panel of experts during the Maximum magnitude workshop (Coppersmith et al., 2016) and a 50-50 weighting on the upper and middle branches of the version 2 GMPE (Bommer et al., 2015). While the forecast activity maps that fed into these hazard

maps were quite different, the spatial distribution of the hazard is very similar for all of the models considered.

The five models result in different peak PGA values. The model underlying Figure 40a is the worst representation of the historical seismicity and the maximum PGA is 0.148 g. The model underlying Figure 40c forecasts a substantial decrease in future seismicity that may not be likely to occur, and as a result the maximum PGA is 0.144 g. These two scenarios provide lower estimates of the PGA. The three remaining models Figure 40b, d and e, show similar maximum PGA hazard values 0.165-0.180 g. The similarity in these PGAs is striking given that they come from two different input data sets (compaction and fault moment).

The spatial and peak PGA value similarities to the compaction based models make it clear that a fault based model can be incorporated without significantly changing the hazard map. This work supports the models previously submitted by NAM by demonstrating that compaction based models provide an assessment of the PGA hazard level that is consistent with fault based model results.

5.0 Summary and Conclusions

Geomechanical models can be used to constrain the range of likely deformation scenarios in the subsurface due to a given production schedule. A geomechanical measure can then be used to generate a seismological model, which is the link between deformation and seismic activity. Subsurface deformation can be driven by reservoir compaction, slip on discrete faults, or a combination of both. The seismological model is a statistical model that represents the average activity rate as a function of the geomechanical input. In the absence of a deep physical understanding of how the number of earthquakes is related to the subsurface deformation, the statistical model can take many forms. Assuming a form for the statistical model will have implications for the seismicity levels that are forecasted in future years.

This report explores many potential forms for the statistical model and methods of calibration to the onset of seismicity. However, this is not a complete analysis and additional forms not investigated here could later prove to offer better representations of the seismicity. Similar to the methodology followed by Bourne and Oates (2015a,b) a few forms for the seismological model were specified *a priori* and these four models are referred to as the specified models. To complement the specified forms, a generic form for a Poisson process was applied that could include a variety of parameters. An iterative approach was used to progressively add one term at a time to the solution to obtain a final seismological model. The end result of this iterative procedure is referred to as the generic model.

In addition to examining many functional forms for the model, both compaction and fault based slip are considered as inputs into the seismological model. Compaction is a field wide variable (every point in space has a compaction associated with it) but that is not the case for fault slip because there is not a fault at every point in space. Therefore, fault slip (fault moment release) was converted to a field variable by distributing the modeled moment release over a spatial area. The amount of dispersion/localization used for this conversion also became a parameter that was examined to determine what produced the best seismological model. The final dimension that was explored was the reference (threshold) value for the

input data. A large amount of production occurred before the initiation of seismicity indicating that a threshold was reached. This threshold could be imposed in the models as either a year or a deformation value (a critical level of compaction or amount of modeled fault slip) so only deformation that occurred after this threshold was reached was considered in generating the statistical model. The threshold used is referred to as the reference since all input geomechanical quantities are in reference to this year or value.

Regardless of the approach taken, models with a reference year were consistently found to provide better fits to the historical seismicity than models with a reference value. Conceptually it makes sense that a large amount of compaction has an effect but a small amount is negligible (a threshold value) but it is hard to come up with a reason that everything changed in one year, especially given the amount of variability in compaction across the field in a given year. However, regardless of the physical intuition, a reference year is consistently the better option. One possibility is that this is the manifestation of an important dependency that is not captured in the current set of variables, but at this point that is strictly speculation.

For fault slip based seismological models different kernel sizes were used to distribute the modeled fault slip over a spatial area. The more localized representations (3 km kernel) preserved the character of the fault network but gave poor fits to the historical seismicity. When the moment was more dispersed (using a 7 km kernel) there were fewer earthquakes observed in areas with a near zero activity rate so the fit was better. The 3 km and 7 km Gaussian kernel scenarios result in very different activity maps and forecasted event numbers. The differences could have large implications for a production cap determined by the number of events but have a much smaller effect on resulting PGA hazard maps. The spatial distribution of hazard is nearly identical and the forecast max PGA value only differs by 10%. For the purposes of this study we have not investigated the effects on spectral accelerations at different structural periods or other values for probability of exceedance.

Fault moment based models can only be made in the domain where the faulted geomechanical models exist. This is referred to as the submodel domain and covers the area where most of the observed earthquakes occurred. To compare compaction and fault based models the analysis must be limited to the submodel domain. Five models were selected to understand the effect on the PGA hazard maps and the variability in activity rates forecasted over the next five years. A seismological model based on the 7 km distribution of fault moment model is statistically the best fit to the past seismicity. The next best models are compaction based and the worst fitting model is the 3 km distribution of fault moment based model. The five models discussed above respectively predict large differences in the forecasted seismicity rate.

The best fitting fault slip based seismological model forecasts lower activity rates over the next 30 years than the seismological model that is used by NAM. Despite these differences, the resulting PGA hazard maps are not substantially different. Compaction and fault based models result in very different spatial distributions of earthquake activity, but this has a relatively small effect on resulting PGA hazard maps due to the fact that the Ground Motion Prediction Equations (GMPEs) act to disperse the hazard over a larger domain.

The results here indicate that a fault based model is a valuable addition to the PSHA process because it can provide a very good representation of the seismicity. However, it will not substantially alter the PGA hazard maps, and hence the results support the compaction based hazard maps previously submitted to the regulator by NAM.

The faulted geomechanical model does not exist in the entire domain of the field, so currently only compaction can be used to develop a field wide activity model. A variety of forms were considered and the model currently used by NAM was found to be one of the better models. However, there are two other seismological models that represent the historical data better, or nearly as well, that make different forecasts about the seismicity rate in the near term.

Many models can represent the observed seismicity equally well, but these models can yield very different activity forecasts over the next 10 years so it might be worthwhile to consider a wide range of models and not be locked into one form at the expense of potentially more predictive models. Multiple models should be carried forward and weighted appropriately in a logic tree so that the unconstrained assumption of one form for the seismological model does not singularly determine the result.

References

Bommer, J. L., Stafford, P. J., Edwards, B., Dost, B., and Ntinalexis, M. *Development of GMPEs for response spectral accelerations and for strong-motion durations (Version 1).* NAM, 2015a.

Bommer, J. J., Dost, B., Edwards, B., Kruiver, P. P., Meijers, P., Ntinalexis, M., Polidoro, B., Rodriguez-Marek, A., and Stafford, P. J. *Development of Version 2 GMPEs for response spectral accelerations and significant durations from induced earthquakes in the Groningen Field.* NAM, 2015b.

Bommer, J. J., Dost, B., Edwards, B., Stafford, P. J., van Elk, J., Doornhof, D., and Ntinalexis, M. "Developing an application-specific ground-motion model for induced seismicity." *Bulletin of the Seismological Society of America*, 2016: 106: 1840-1857.

Bourne, S., and Oates, S. *An activity rate model of induced seismicity within the Groningen Field (Part 1).* NAM, 2015a.

Bourne, S., and Oates, S. *An activity rate model of induced seismicity within the Groningen Field (Part 2).* NAM, 2015b.

Coppersmith, K., Ake, J., Bungum, H., Dahm, T., McGarr, A., Main, I., Wong, I., and Youngs, R. *Workshop on maximum magnitude estimates for Probabilistic Seismic Hazard and Risk modeling in Groningen Gas Field.* NAM, 2016.

Kamp, H. G. J. "Letter to the House of Representatives on natural gas extraction in Groningen." Ministry of Economic Affairs, the Netherlands, 2016.

Lele, S. P., Hsu, S.-Y., Garzon, J. L., DeDontney, N., Searles, K. H., Gist, G. A., and Dale, B. A. "Geomechanical modeling to evaluate production-induced seismicity at Groningen Gas Field." *Abu Dhabi International Petroleum Exhibition and Conference.* Abu Dhabi, UAE: Society of Petroleum Engineers, 2016.

Sanz, P. F., Lele, S. P., Searles, K. H., Hsu, S.-Y., Garzon, J. L., Burdette, J. A., Kline, W. E., Dale, B. A., and Hector, P. D. "Geomechanical analysis to evaluate production-induced fault reactivation at Groningen Gas Field." *SPE Annual Technical Conference and Exhibition.* Houston, TX: Society of Petroleum Engineers, 2015.

van Thienen-Visser, K., Sijacic, D., van Wees, J-D., Kraaijpoel, D., and Roholl, J., "Groningen field 2013 to present gas production and induced seismicity." TNO report R10425, 2016.